UNIVERSITÀ DEGLI STUDI DI PADOVA

DIPARTIMENTO DI SCIENZE CHIMICHE

LAUREA MAGISTRALE IN SCIENZA DEI MATERIALI

TESI DI LAUREA MAGISTRALE

Synthesis and Characterization of Iron based Model Electrocatalysts for Hydrogen Evolution Reaction

Relatore: Dr. Mattia Cattelan

Controrelatore: Prof. Andrea Sartorel

Laureando: Samuele Lasagna

ANNO ACCADEMICO 2022/2023

Abstract

Molecular hydrogen is an attractive energy vector with a high gravimetric energy density and it is considered a “green” alternative to traditional fossil fuels, main causes of the climate change. However, nowadays hydrogen is mostly produced in a not “green” way, i.e., via the methane steam reforming ($CH_4 + H_2O \leftrightarrow CO + 3H_2$) of natural gas and subsequent water-gas shift reaction ($CO + H_2O \leftrightarrow H_2 + CO_2$), which produces carbon dioxide. In the quest of H_2 production with zero carbon emissions, electrochemical water splitting ($2H_2O$ + energy → $2H_2 + O_2$) has become one of the most promising routes, since it employs water and electrical energy from renewable sources, such as wind turbines or photovoltaic.

Electrochemical water splitting can be conducted in acidic or alkaline media. The former is usually performed using a proton exchange membrane (PEMs) with high energy efficiency and fast hydrogen production rate. However, the acidic medium limits the electrocatalysts choice for the two semi-reactions, i.e., the Hydrogen Evolution Reaction (HER) and Oxygen Evolution Reaction (OER), to critical raw materials and precious metal and oxides (Pt, RuO_2, IrO_2), resulting in a not sustainable and expensive production of H_2. On the other hand, water electrolysis in alkaline medium, broadens the range of the available electrocatalysts to earth-abundant materials, including Ni and Fe. The latter is the fourth most abundant element in Earth’s crust and considered neither harmful nor critical material.

My Master Thesis aim was to gain a fundamental understanding of morphological, structural, and electrochemical properties of ultrathin Iron oxide films prepared as model system on a single crystal Gold (111). To perform such careful investigations, I used both surface science to synthesize and characterize materials, and electrochemical tools to study their activity. The surface science methods I employed are the following: X-ray Photoelectron Spectroscopy (XPS), Low Energy Electron Diffraction (LEED) and Physical/Chemical Vapor Deposition (PVD/CVD) under Ultra-High Vacuum (UHV) conditions. The electrochemical methods I used are Cyclic Voltammetry (CV) and Linear Sweep Voltammetry (LSV). Most importantly, I also worked with state-of-the-art

combination of these tools, i.e., with an *in-situ* electrochemical setup connected to XPS and the Electro-Chemical Scanning Tunneling Microscopy (EC-STM), which allows to directly visualize changes at the atomic scale in the materials during the catalytic activity. To improve further the performances of the materials, the effect of the addition of a second metal, Manganese, on the substrate FeO_x/Au(111) was also investigated.

Sommario

L'idrogeno molecolare è un attraente vettore energetico con alta densità di energia gravimetrica ed è considerato come alternativa "verde" ai tradizionali combustibili fossili, causa principale del cambiamento climatico. Tuttavia, attualmente l'idrogeno è prodotto prevalentemente in modo non sostenibile, ovvero tramite il processo di steam reforming di gas naturale ($CH_4 + H_2O \leftrightarrow CO + 3H_2$) e successiva reazione di spostamento del gas d'acqua ($CO + H_2O \leftrightarrow H_2 + CO_2$), che produce diossido di carbonio. Nella corsa alla produzione di idrogeno senza emissioni di carbonio, l'elettrolisi dell'acqua ($2H_2O$ + energy $\rightarrow 2H_2 + O_2$) è diventato uno dei processi più promettenti dal momento che sono impiegate acqua ed energia elettrica da fonti sostenibili e rinnovabili come l'eolico o il fotovoltaico.

L'elettrolisi dell'acqua può essere condotta in ambiente acido o alcalino. Nel primo caso è realizzata con membrane a scambio protonico (PEM) con alta efficienza energetica ed elevata velocità di produzione di idrogeno. Tuttavia, l'ambiente acido limita gli elettro-catalizzatori per le due semi-reazioni, ossia la Reazione di Evoluzione di Idrogeno (HER) e la Reazione di Evoluzione di Ossigeno (OER), a materie prime critiche, metalli preziosi e loro ossidi (Pt, RuO_2, IrO_2), risultando in una produzione di H_2 costosa e non sostenibile. D'altra parte, l'elettrolisi dell'acqua in ambiente alcalino allarga la gamma di elettro-catalizzatori utilizzabili a materiali abbondanti, tra cui Ni e Fe. Quest'ultimo è il quarto elemento più abbondante sulla crosta terrestre, non è né nocivo né considerato un materiale critico.

L'obiettivo della mia Tesi Magistrale è stato di acquisire una comprensione di base delle proprietà morfologiche, strutturali ed elettrochimiche di strati ultrasottili di ossido di ferro preparati come sistemi modello su un cristallo singolo di Oro (111). Per questo accurato studio ho usufruito sia della scienza delle superfici per sintetizzare e caratterizzare i materiali, sia di strumentazione elettrochimica per investigare la loro attività. Le tecniche di scienza delle superfici che ho utilizzato sono state: spettroscopia fotoelettronica a raggi X (XPS), diffrazione di elettroni a bassa energia (LEED) e deposizione fisica/chimica da vapore (PVD/CVD) in condizioni di ultra-alto vuoto (UHV).

I metodi elettrochimici che ho impiegato sono la voltammetria ciclica (CV) e la voltammetria a scansione lineare (LSV). In particolare, ho lavorato anche con combinazioni allo stato dell'arte di questi strumenti, ossia, un setup di elettrochimica *in-situ* collegato a XPS e la microscopia elettrochimica ad effetto tunnel (EC-STM), che permette di visualizzare in maniera diretta i cambiamenti fino alla scala atomica nei materiali durante l'attività catalitica. Per migliorare ulteriormente le performance dei materiali, è stato anche indagato l'effetto dell'aggiunta di un secondo metallo, Manganese, sul substrato FeO_x/Au(111).

Sommario

List of abbreviations

AEMWE	Anion Exchange Membrane Water Electrolyser
AWE	Alkaline Water Electrolyser
BCC	Body-Centered Cubic
BE	Binding Energy
CAE	Constant Analyzer Energy
CE	Counter Electrode
CV	Cyclic Voltammetry
DA	Dual Atom
DAC	Dual Atom Catalyst
EBPVD	Electron Beam - Physical Vapour Deposition
EC-STM	Electro Chemical - Scanning Tunnelling Microscopy
FCC	Face-Centered Cubic
HBE	Hydrogen Binding Energy
HCP	Hexagonal Close-Packed
HER	Hydrogen Evolution Reaction
HOR	Hydrogen Oxidation Reaction
IMFP	Inelastic Mean Free Path
KE	Kinetic Energy
LDH	Layered Double Hydroxide
LEED	Low Energy Electron Diffraction
LSV	Linear Sweep Voltammetry
LVP	Lower Vertex Potential
ML	MonoLayer
MLE	MonoLayer Equivalent
MOCVD	Metal Organic - Chemical Vapour Deposition
NP	NanoParticle
OCP	Open Circuit Potential
OER	Oxygen Evolution Reaction

PEM	Proton Exchange Membrane
RDS	Rate Determining Step
RE	Reference Electrode
RHE	Reversible Hydrogen Electrode
SHE	Standard Hydrogen Electrode
SSC	Silver – Silver Cloride
STM	Scanning Tunnelling Microscopy
UHV	Ultra-High Vacuum
UPD	Under Potential Deposition
UVP	Upper Vertex Potential
XPS	X-ray Photoelectron Spectroscopy
WE	Working Electrode

1 Introduction

1.1 Climate change and greenhouse gases emissions

The global average temperature is today 1.1°C higher with respect to the 1951-1980 mean, as shown in figure 1-1 (a)[1], with devastating effects on the Earth equilibria as can be seen by the more and more frequent environmental disasters, aridification, droughts, glaciers' melting, extinction/migration of species due to alteration of the ecosystems.[2] This temperature increase is directly correlated with the increase of the greenhouse gases concentration in the atmosphere, in particular CO_2, shown in figure 1-1 (b)[3], that has never been so high in the last 800000 years and of most of all is much higher than a level compatible with its concentration's periodic oscillation. Not only the CO_2 concentration is increasing, but also the annual emissions[4]. By staying on this trend, we will risk to make our Planet inhabitable, or to attend huge climate migrations toward the few habitable regions left on Earth and so unimaginable overpopulation and all the related problems.

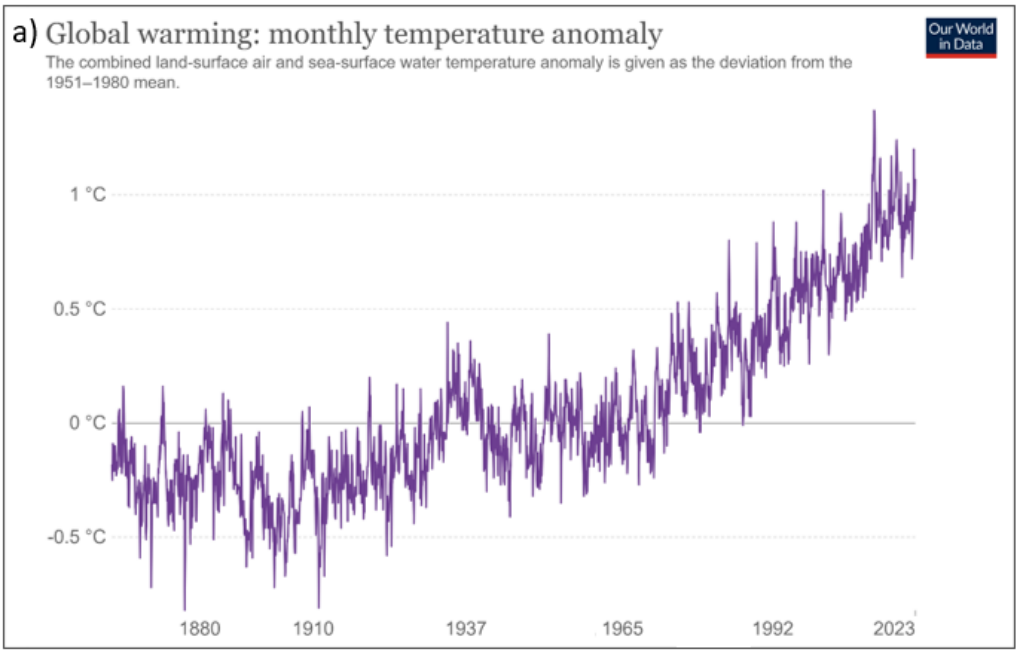

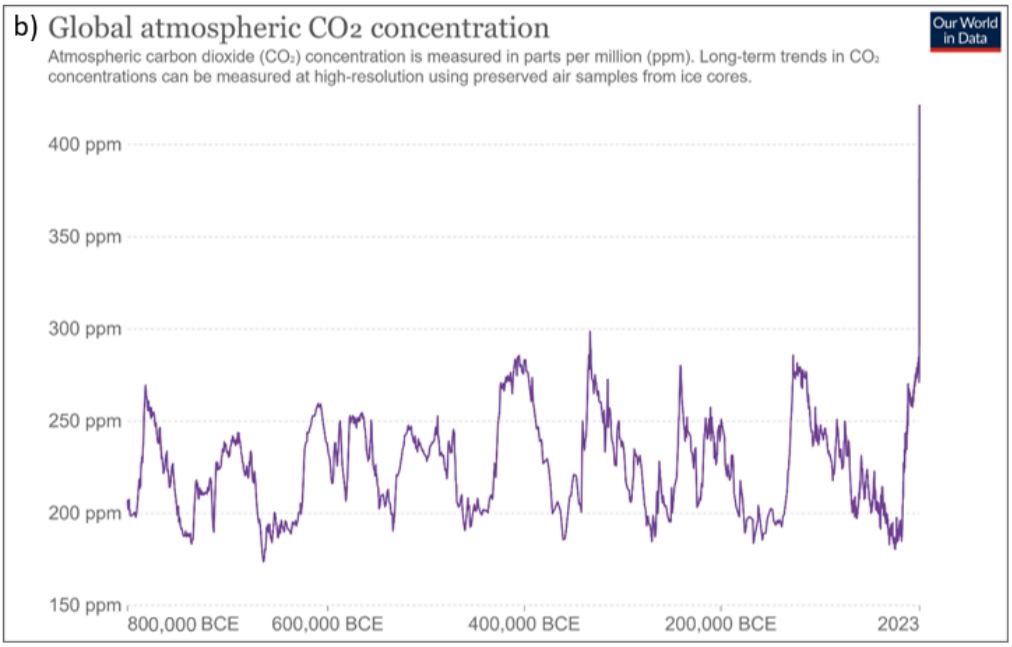

Figure 1-1: (a) combined land-surface air and sea-surface water monthly temperature anomaly, given as the deviation from the 1951–1980 mean. Adapted from Ref. 1. (b) global atmospheric carbon dioxide concentration measured in parts per million (ppm). Adapted from Ref. 3.

CO_2 average global concentration is nowadays ≈420 ppm[5] and has never been so high: the last time CO_2 levels exceeded 400 ppm was around four million years ago, during the Pliocene era, when global temperatures were 2-4°C warmer and sea levels were 10-25 m higher than today[6].

The main cause of CO_2 and other greenhouse gases emissions is found in the energy sector[7], as clearly visible in figure 1-2, due to our dependence on fossil fuels as energy sources, either in their direct use (as for transports or heating) or indirect (to produce electricity). It is evident we must move to renewable energy sources, i.e. sources that are replenished on a time human scale (e.g. sunlight, wind and water movement, geothermal heat), and to fuels with a life-cycle which CO_2 net emissions are zero such as green hydrogen, bio-ethanol, ammonia and solar driven CO_2 Reduction Reaction (CO_2RR) products (methane, methanol, formic acid, etc.).

In this thesis, it was investigated the performance of an Iron-based catalyst in hydrogen generation from water.

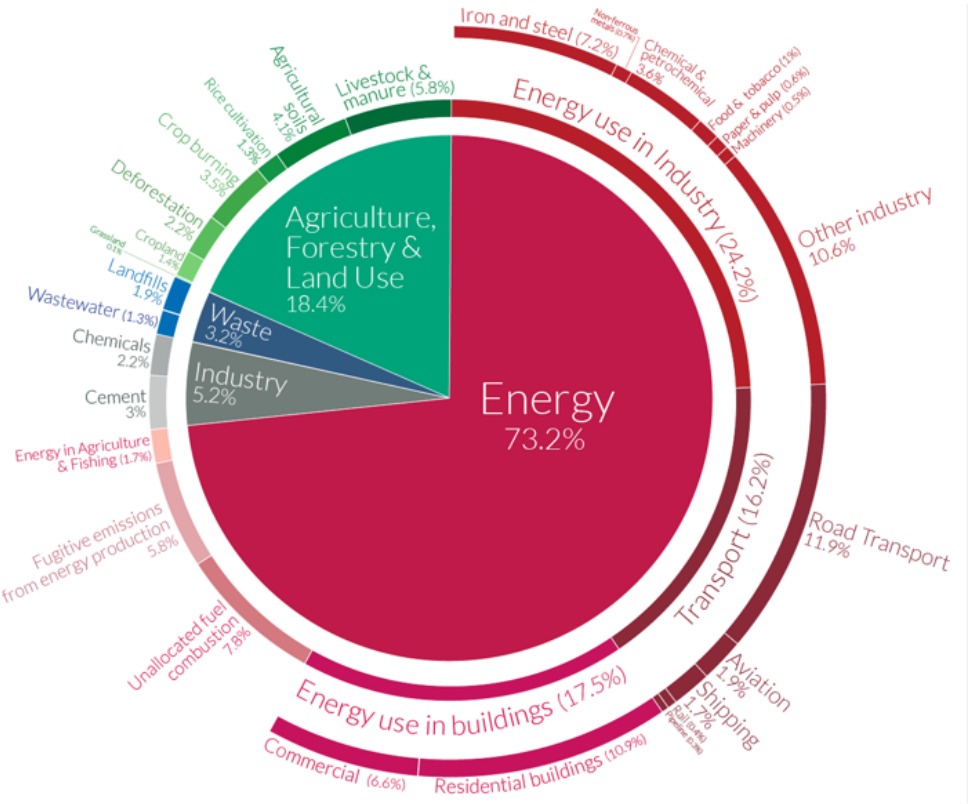

Figure 1-2: greenhouse gases emissions by sector in year 2016 (total emissions were 49.4 billion tonnes CO_2 equivalent). Reproduced from Ref. 7

1.2 Molecular Hydrogen

In the last decades, molecular Hydrogen H_2 gained higher and higher interest as energy carrier, because of its high energy content by weight (nearly three times the one of gasoline), being non-toxic and, most of all, having the potential to be completely sustainable, since its combustion produces only water as exhaust, in addition to a considerable amount of energy as heat:

$$2H_2 + O_2 \rightarrow 2H_2O$$

Furthermore, by driving the process electrochemically, by means of fuel cells devices, the Gibbs free energy of the reaction (-228.6 kJ/mol[8]) can be converted into electrical work, in this way one can eliminate the thermodynamic constraints unavoidable if the work was generated from the heat produced by the reaction.

But hydrogen is only as clean as the technologies used to produce and use it. Replacing fossil fuels with hydrogen to provide energy services could bring major environmental

benefits, with the condition that hydrogen is used in non-polluting fuel cells and that the carbon dioxide and harmful gases emitted in the hydrogen-production process are reduced or eliminated.

The production of hydrogen can be emission-free if the energy used in the production process is derived from renewables. Nowadays, about 96% of hydrogen global production comes from fossil fuels, especially *via* the methane steam reforming ($CH_4 + H_2O \leftrightarrow CO + 3H_2$) which is followed by the water-gas shift reaction ($CO + H_2O \leftrightarrow H_2 + CO_2$), with production of net carbon dioxide emissions.[9,10]

To be completely sustainable, hydrogen production should exploit "green" energy and exclude fossil fuels from the process. Water electrolysis is one of the major candidates as a sustainable process (if powered by renewable energy sources).

1.2.1 Alkaline Water Electrolysis

Water electrolysis is the chemical reaction in which water is converted to H_2 and O_2 through application of electrical energy. At the cathode the HER occurs, while at the anode Oxygen is produced by OER. The half-reactions and mechanisms are different according to the acidity or basicity of the electrolyte. In acid conditions the half-reactions are:

$$\text{Cathode: } 2H^+ + 2e^- \rightarrow H_2$$
$$\text{Anode: } 2H_2O \rightarrow O_2 + 4H^+ + 4e^-$$
$$\text{Total reaction: } 2H_2O \rightarrow 2H_2 + O_2$$

In acidic conditions, the HER starts with the proton adsorption to the catalyst's active site, also known as the Volmer step:

$$\text{Volmer step: } H^+ + e^- \rightarrow H_{ad}$$

The Volmer step is followed by the formation of the H_2 molecule on the surface, that can be both electrochemical, involving a hydrogen ion from the solution (Heyrovsky step) or just chemical, in which two adsorbed hydrogen atoms reacts to form a hydrogen molecule (Tafel step):

$$\text{Heyrovsky step: } H^+ + e^- + H_{ad} \rightarrow H_2$$

$$\text{Tafel step: } 2H_{ad} \rightarrow H_2$$

In acid, the Tafel slope is used to assess the Rate Determining Step (RDS) of acid HER on a certain material. According to the Sabatier principle, the most active catalyst, so the one with the highest exchange density current j_0, should show a not too weak nor too strong adsorption of the proton, thus, an intermediate Hydrogen Binding Energy (HBE); this can be clearly seen in the so-called volcano plot, shown in figure 1-3[11], in which the exchange density current is plotted against the activity descriptor ΔG_H, the hydrogen adsorption Gibbs free energy. Pt, the best catalyst for acid HER, exhibits an almost zero ΔG_H.

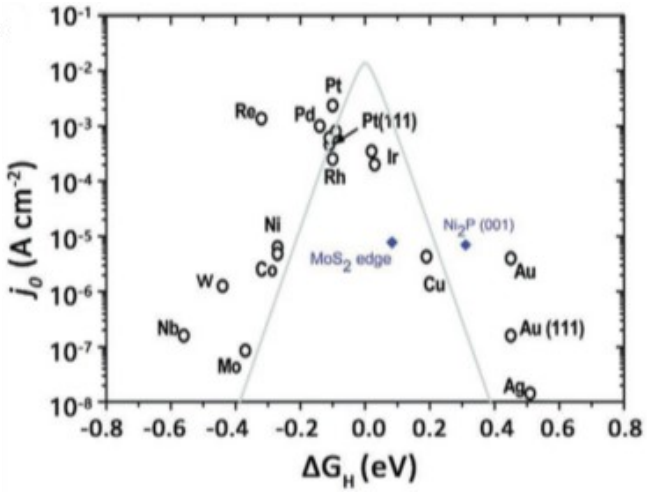

Figure 1-3: Volcano plot of exchange current density against the activity descriptor of ΔG_H in acidic electrolytes. Adapted from Ref. 11

While the acidic medium limits the electrocatalysts choice for the two semi-reactions, i.e HER and OER, to critical raw materials and precious metal and oxides (Pt, RuO_2, IrO_2), resulting in a not sustainable and expensive production of H_2, water electrolysis in alkaline medium, broadens the range of the available electrocatalysts to earth-abundant materials, including Ni and Fe.

In alkaline conditions[12–14], the half-reactions at the electrodes are slightly different:

$$\text{Cathode: } 2H_2O + 2e^- \rightarrow H_2 + 2\text{OH}^-$$
$$\text{Anode: } 4OH^- \rightarrow O_2 + 2H_2O + 4e^-$$
$$\text{Total reaction: } 2H_2O \rightarrow 2H_2 + O_2$$

While Tafel steps keeps the same as in acid medium, Heyrovsky and Volmer steps are described with water rather than protons as reactants:

$$\text{Volmer step: } H_2O + e^- \rightarrow H_{ad} + \text{OH}^-$$

$$\text{Heyrovsky step: } H_2O + H_{ad} + e^- \rightarrow H_2 + OH^-$$

Therefore, in the Volmer and in the Heyrovsky steps in alkaline medium, the adsorption of the hydrogen and the formation of the hydrogen molecule, respectively, are necessarily preceded by the dissociation of water. This unavoidable step may introduce an additional energy barrier and, thus, influence the kinetics of the overall reaction.

Unfortunately, the reaction kinetics of HER is sluggish in alkaline electrolytes, which is at least two orders of magnitude lower than that in acid[12,15]. This may be due to the slower transport of OH^- compared to H^+ in solution or to the stronger O-H bond in water molecules (HO-H) than in hydrated protons (H_2O-H^+) or to the hydrogen adsorption ability on a certain surface[16], in addition to the water dissociation energy barrier previously mentioned.

Therefore, the performance of a catalyst in alkaline HER is affected by water adsorption energy on active sites, water dissociation energy barrier, HBE and adsorption strength of aqueous OH^- (which, if too strong, may poison the surface by occupying active sites). In the above elementary reaction steps, adsorbed hydrogen appears to be the only reaction intermediate on the electrode surface, similar to the case in the acidic electrolyte. Consequently adsorption and removal of adsorbed H atoms become competitive processes. Sheng et al.[17] showed that also in alkaline medium, there is correlation between the HER exchange current densities and HBE values, as shown in figure 1-4, suggesting that the HER activity could be tailored by tuning the surface chemical

properties such that an optimal HBE value can be obtained. Iron HBE is – 0.59 eV while Gold one is 0.14 eV.

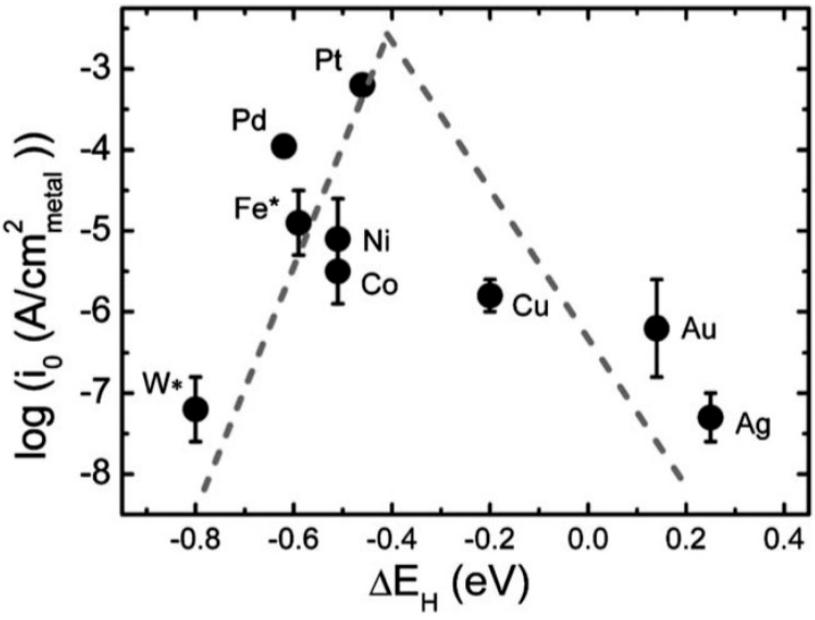

Figure 1-4: Exchange current densities, log(i_0), on monometallic surfaces plotted as a function of the calculated HBE. The i_0s for non-Pt metals were obtained by extrapolation of the Tafel plots between 1 and 5 mA cm_{disk}^{-2} to the reversible potential of the HER and then normalization by the electrochemical surface areas of these metal surfaces. Reproduced from Ref. 17.

Alkaline electrolysis is performed in alkaline water electrolysers (AWEs), a scheme is shown in figure 1-5[18]. The cell consists of two electrodes separated by a gas-tight diaphragm. This assembly is immersed in a liquid electrolyte that is usually a highly

concentrated aqueous solution of KOH, of the order of 25–30 wt.%, to maximize its ionic conductivity. Typical operating temperatures range from 65 °C to 100 °C[19].

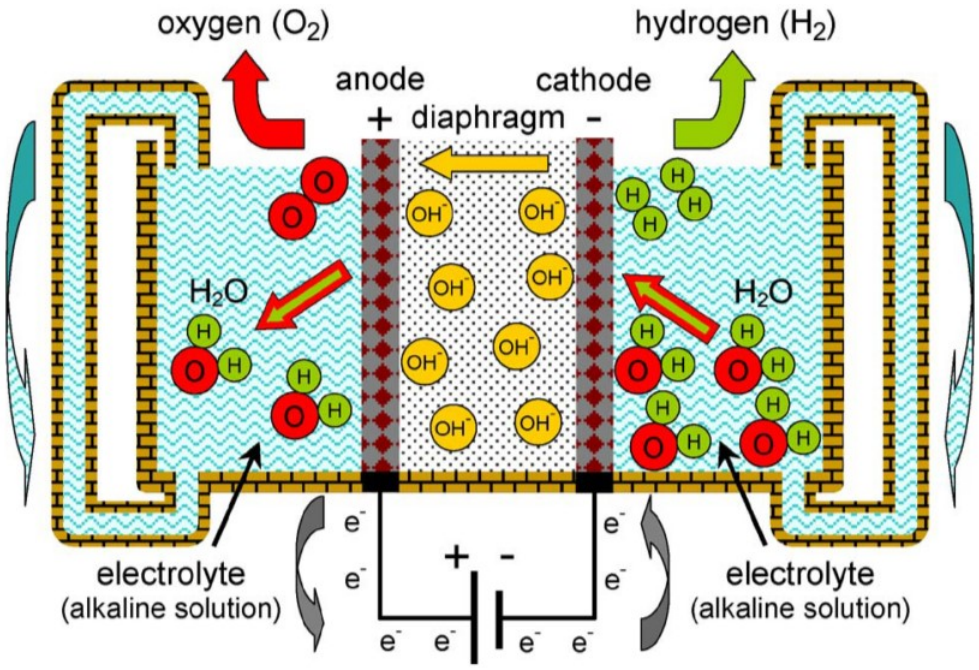

Figure 1-5: schematic representation of an electrolyser. Reproduced from Ref. 18

The evolution of the gaseous products from the electrodes is critical because a significant overvoltage concentration can be originated that reduces the electrolysis efficiency. In order to facilitate gas bubbling, the electrodes should be carefully designed to maximize the interfacial contact area with the liquid electrolyte. To this end, it is important that the electrodes have a porous texture and show many perforations. The great advantage of water electrolysis, compared with other methods for producing hydrogen, is the high purity levels of hydrogen and Oxygen that are reached without any auxiliary purification equipment: 99.9 and 99.7 vol.%, respectively[20–22]. On the other hand, the water fed to the electrolyzer has to be significantly pure, with an electric conductivity below 5 µS/cm[23] in order to protect the electrodes and operate safely, avoiding undesired electrochemical reactions.

To increase the efficiency of the device, e.g. reducing the amount of energy used per kg H_2 produced, some improvements have been done and still are under investigation: the minimization of the space between the electrodes in order to reduce the ohmic losses

and allow working with higher current densities, the transition from conventional AWEs with oxide based finite diaphragms to zero-gap electrolysers, namely, Anion Exchange Membrane Water Electrolysers (AEMWEs), shown in figure 1-6[24], that allows high current densities up to 1.7 A cm^{-2} at 1.8 V[25], the development of high-temperature alkaline water electrolyzers that promotes the kinetics of the electrochemical reactions on the electrodes surface, and, last but not least, the development of advanced electrocatalytic materials to reduce the electrode overvoltages.

The object of investigation of this thesis is Iron, a very common electrocatalyst for water electrolysis.

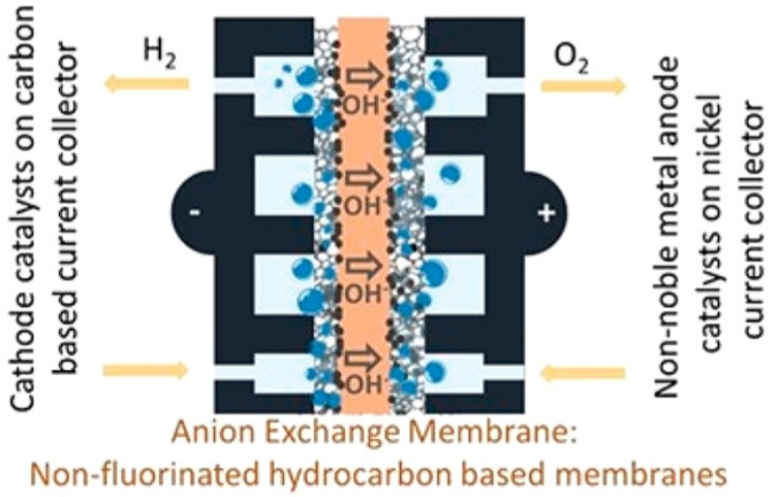

Figure 1-6: zero-gap AEMWE utilizing an OH^- conducting membrane. Adapted from Ref. 24

Iron has been extensively studied as electrocatalyst for HER and OER, both as oxide/hydroxide and as dopant in Layered Double Hydroxides (LDHs). Fe is one of the most effective chemical additives to Ni catalysts, especially for promoting the OER. In fact, Fe^{3+} ions can increase electron conductivity and the reaction kinetics since these species have an optimal bond energetics for the adsorption of OER intermediates. However, Iron's worth noting that many studies have reported contradictory conclusions[26]. For this reason, fundamental studies employing in-situ and in-operando techniques, such as the one presented in this thesis, are of paramount importance to clarify I ron's catalytic role.

1.3 Iron Oxides

The Iron oxides are all based on a close packed O^{2-} anion lattice, with the smaller Fe cations occupying octahedrally and tetrahedrally coordinated interstices in between, figure 1-7[27].

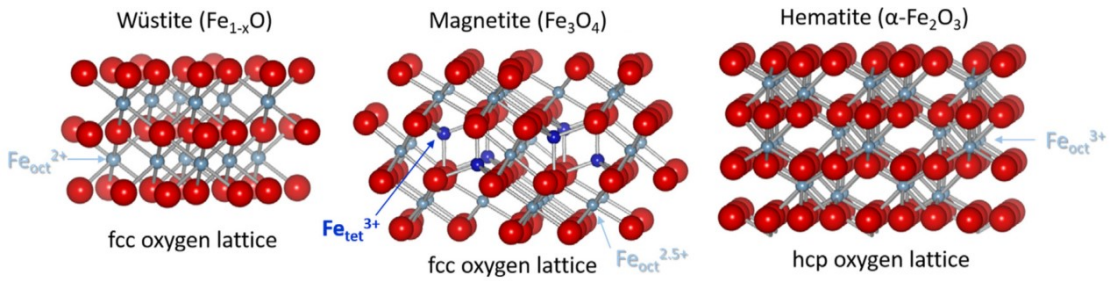

Figure 1-7: Iron oxides crystalline structures. Maghemite (not shown) is isostructural with magnetite, but with Fe vacancies on the octahedral sublattice. Reproduced from Ref. 27.

Under the most reducing conditions, wüstite ($Fe_{1-x}O$) is formed. It crystallizes in the rocksalt structure, contains Fe^{2+} in octahedral sites, and is often non-stoichiometric with a cation deficiency. Under oxidizing conditions, hematite (α-Fe_2O_3) is formed. α-Fe_2O_3 crystallizes in the corundum structure and contains Fe^{3+} in octahedral sites. In between, there is magnetite (Fe_3O_4), an (inverse) spinel with Fe^{3+} in tetrahedral sites and a 50:50 mixture of Fe^{2+} and Fe^{3+} in octahedral sites. Finally, when Fe_3O_4 is oxidized directly, Fe^{2+} is converted to Fe^{3+} within the spinel structure, and compensating Iron vacancies appear in the octahedral sublattice. The defective spinel structure is remarkably robust and can accommodate the full range of stoichiometry between Fe_3O_4 and Fe_2O_3. In the extreme case, all Fe is oxidized to Fe^{3+}, and maghemite (γ-Fe_2O_3) is formed. γ-Fe_2O_3 is metastable against transformation to α-Fe_2O_3 but exists partly because the conversion from the spinel to the corundum structure requires the O^{2-} lattice to be converted from face-centered cubic (FCC) to hexagonal close-packed (HCP). In contrast, switching between γ-Fe_2O_3, Fe_3O_4 and $Fe_{1-x}O$ is remarkably fluid because this only requires a rearrangement of the cations within a FCC Oxygen lattice.

The Fe-O_2 phase diagram, shown in figure 1-8[28], reveals that γ-Fe_2O_3, Fe_3O_4 and $Fe_{1-x}O$ can all be the stable bulk phase at O_2 pressures and temperatures accessible in a UHV

surface science experiment. However, in the nanoscale things may be very different, also the substrate may play an important role in stabilizing some phases rather than others.

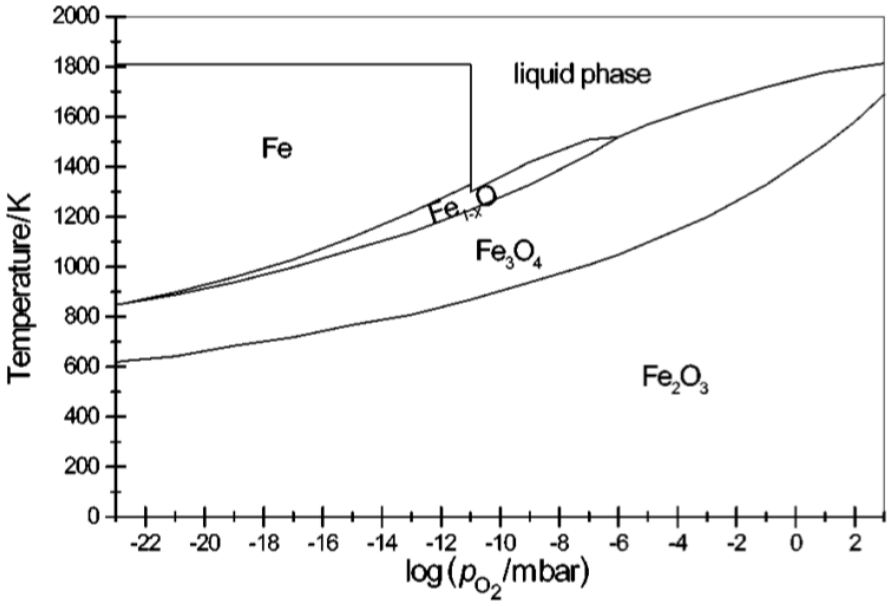

Figure 1-8: Temperature-pressure phase diagram for the Iron-Oxygen system. Reproduced from Ref. 28

It is important to know also that Iron is present in nature also with its hydroxides, divided into thermodynamically unstable (ferrihydrite $Fe_2O_3 \cdot 2FeOOH \cdot 2.5H_2O$, feroxyhyte $\delta - FeOOH$, and lepidocrocite $\gamma - FeOOH$) and the stable goethite $\alpha - FeOOH$[29]. Goethite is isostructural with diaspore, AlO(OH), and groutite, MnO(OH), and can be described in terms of a slightly distorted hexagonal close-packed O-atom arrangement with Fe atoms occupying one-half of the octahedral interstices, and with all atoms located on mirror planes. There are two distinct O sites, O1 and O2, each bonded to three Fe atoms, with O2 additionally bonded to an H atom[30].

1.4 Iron Oxides model systems on Au (111)

Model systems, as single crystals, are crucial for fundamental heterogeneous catalysis studies, giving a conceptual insight into questions that are very difficult to acquire otherwise. As well-known surfaces, they allow a significant low level of complexity, that can be increased step by step up to the real catalytic material, as shown in figure 1-9[31]. Starting from the well-known surface of the metal single crystal, Au(111) in this thesis, high ordered thin oxide films can be grown epitaxially (and pseudomorphically if the

mismatch between the metal substrate and the oxide allows it) and be used as substrate in turn, for the growth of nanoparticles (NPs), both pure or as alloys, and subsequent defects engineering.

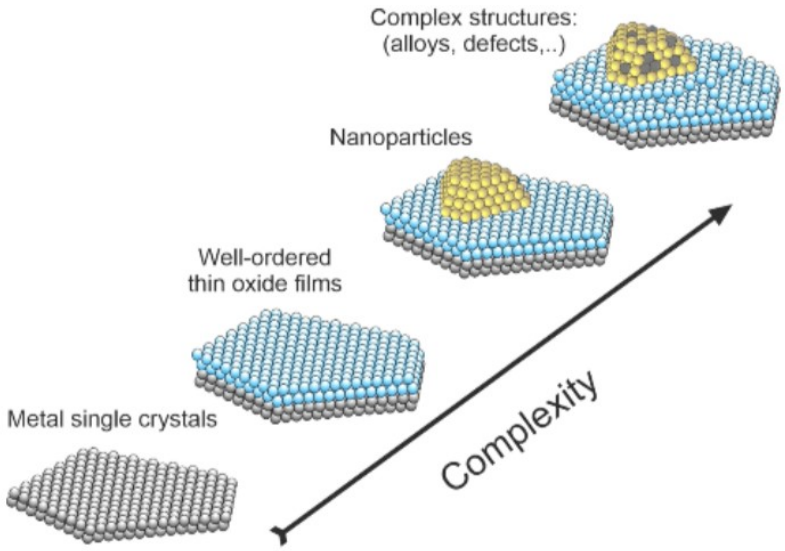

Figure 1-9: schematic representation of complexity levels in modelling heterogeneous catalysts. Reproduced from Ref. 31.

Moreover, metal single crystals, given their conductivity, allow to investigate insulating materials like oxides, provided a low thickness of the film: the traditional surface science techniques based on charged information carriers, such as electrons and ions, may be employed without having to deal with electrical charging problems occurring for bulk materials.

Via the control of the thickness of the films, one is able to secure that the electronic properties of the films approach those of the bulk materials. The controllable preparation of such supports is an important prerequisite to continue to work towards the next step of complexity by depositing metal NPs onto these supports. In addition, with the preparation of supported particle systems it is possible to address questions concerning the properties of the metal-support interface, and its importance in catalytic reactions, as well as the chance to investigate those phenomena down to the atomic level.

1.4.1.1 *In-operando characterization*

Nowadays, surface science has reached a step further: characterizing the model catalysts far from their working conditions is not enough anymore. *In-situ* techniques allow to characterize the material as prepared in UHV without exposing it to air and, thus, to carbon impurities as well as to 0.21 atm O_2 pressure. In this thesis, the electrochemical characterization was carried out by means of an electrochemical cell *in-line*, directly connected to the UHV preparation chamber, see paragraph *2.6.2*. Furthermore, to rationally drive the development of the catalysts, it is necessary to gain knowledge of the active site structures, the reaction pathways, and the degradation mechanisms. To this aim, *in-operando* characterization of the electrode–electrolyte–gas interface of electrocatalytic processes under electrochemical working conditions has paramount importance. Electro Chemical – Scanning Tunneling Microscopy, described in paragraph *2.8*, allows to directly visualize changes in the materials during the catalytic activity, or more in general upon arbitrary polarization, with a resolution that can range from tens of nanometres down to the atomic scale. This is naturally much more complex than simple Scanning Tunneling Microscopy (STM), the interface is not anymore solid-vacuum but the more complicated one solid-liquid, reaction occurs during measurements and the electrochemical and tunnelling potential are bound to each other and have to be managed in a proper way. In the last decade, great effort has been done and is being done in *operando* characterization to elucidate reaction mechanisms and/or surface dynamics of Cu based catalysts for CO_2RR[32–36] and Co, Ni, Fe-based catalysts for alkaline OER and HER[37–42].

1.4.2 Au (111)

In this thesis, a Gold Single Crystal Au (111) was chosen as substrate of the model catalyst.

Gold is an FCC metal that exhibits a reconstruction of the close-packed (111) surface. Unreconstructed Au(111) planes consist of hexagonal lattices, as Au has a FCC crystal structure. For the reconstructed Au(111) surface, a complex structure consisting of paired rows is observed, as shown in the STM images in figure 1-10[43]. The bright lines are boundaries between unfaulted FCC and faulted hcp stacking[44]. This faulting arises

because the surface atomic bonds undergo a uniaxial contraction by 4% along the $\langle 1\bar{1}0 \rangle$ direction and the surface therefore contains more atoms than a bulk (111) plane. For every 22 atoms along the $\langle 1\bar{1}0 \rangle$ direction in the bulk there are 23 surface atoms, resulting in a $\left(22 \times \sqrt{3}\right)$ unit cell. Long-range forces on this surface further complicate matters in which the lowest energy configuration involves a periodic change in the direction of the reconstruction, and this results in a zig-zag appearance that is called the herringbone reconstruction.[45]

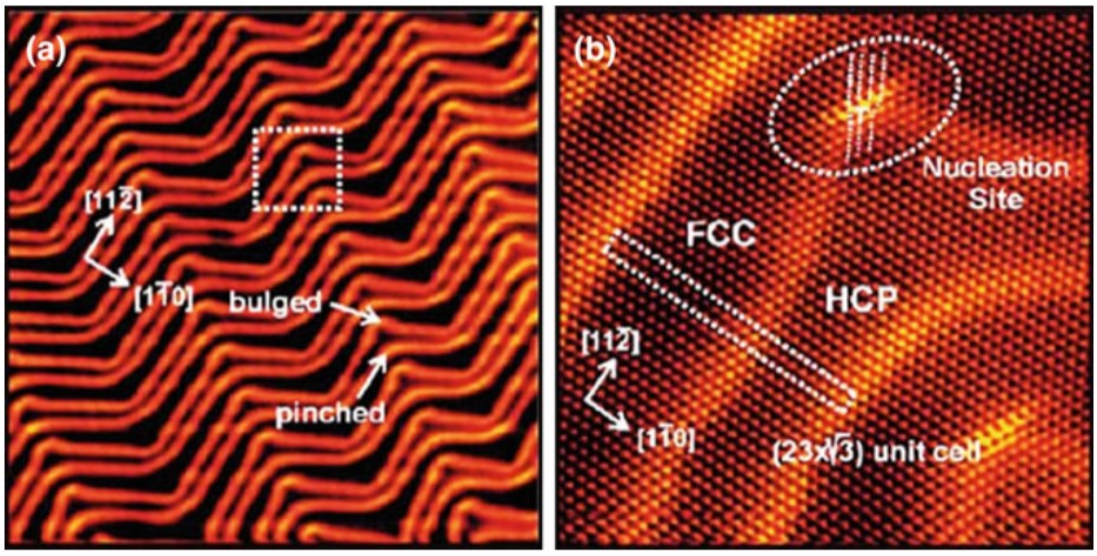

Figure 1-10: STM images showing a) large scale herringbone reconstruction of the Au(111) surface (Image size: 80.2 × 79.5 nm^2) and b) atomically resolved (22 × √3) unit cells on Au(111) (Image size: 14.1 × 13.5 nm^2; U_T = – 0.04 V; I_T = 1.55 nA). Reproduced from Ref. 43.

1.4.3 FeO_x/Au(111)

As the fourth most abundant element on the Earth's crust and being neither harmful nor critical material, Iron is one of the major candidate catalysts to drive the ecological transition. Iron and Gold combination have been subject of extensive studies in UHV, mainly on model surfaces, and in applied chemistry mostly in NPs.

The growth of Fe and its oxides on Au (111) has been and is being extensively studied[45–55] because of the applications in heterogeneous catalysis[56–58], electronics and spintronics[59–61] and gas sensing[58,62].

For applied chemistry Au/Fe NPs may be synthesized in many ways and for different purposes. Liu et al.[59], in order to integrate the optical functionality of Gold (given its surface plasmon resonance) and the magnetic properties of Iron, synthesized AuFe alloy NPs with different compositions via a one-pot polyol process, using Gold acetate and Iron (III) acetylacetonate as precursors, obtaining high control on the atomic ratio and close particles' size distribution. Furthermore, Fe/Au NPs were also synthesized in different core-shell structures to tailor magnetic and optical properties by using reverse micelles as micro-reactors, both Iron-Gold core-shell[63,64] and onion-like Au/Fe/Au structures[65,66] were synthesized and characterized.

Another way to synthesize Iron/Iron oxide NPs or thin films on Gold is by means of Electron Beam - Physical Vapour Deposition (EBPVD) in UHV, allowing great control on the purity of the system.

Under UHV conditions, nucleation the PVD of metallic Iron starts at the corners of the herringbone reconstruction[47,48], known to be hotspots of surface energy, as shown in figure 1-11[53].

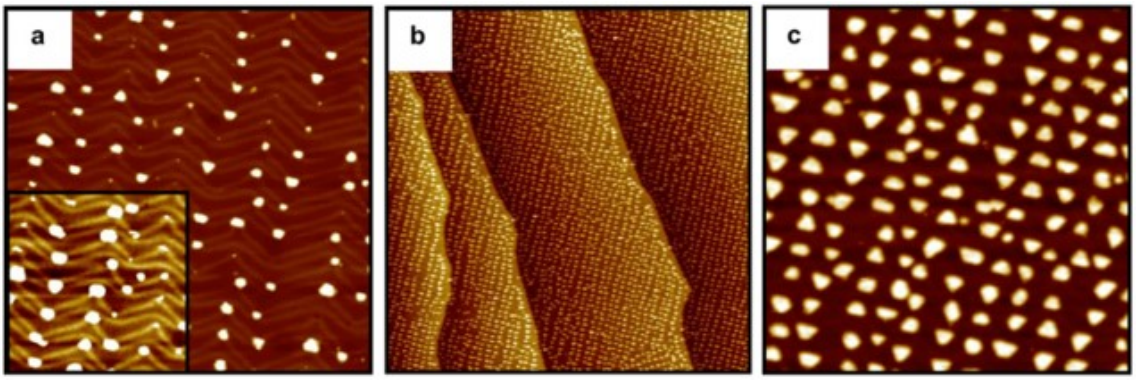

Figure 1-11: Room temperature STM images of 0.25 ML Fe on Au(111): (a) 0.08 ML Fe, 100 x 100 nm^2 (I_T = 1.2 nA, U_T = 0.8 V); (b) 0.25 ML Fe, 500 x 500 nm^2 (I_T = 0.9 nA, U_T = 1.0 V); (c) 0.25 ML Fe, 100 x 100 nm^2 (I_T = 0.9 nA, U_T = 1.0 V). Adapted from Ref. 54.

Until a critical thickness of ≈1.7 ML, the growth of a metastable FCC (111) phase occurs pseudomorphically with formation of triangular-shaped NPs; above ≈1.7 ML, Allmers et al.[46] observed a phase transition from FCC (111) to the native RT body-centered cubic

(BCC) structure of Fe, showing (110) planes, with formation of rectangular-shaped crystallites resembling the twofold symmetry of BCC (110).

On the other hand, Iron oxides, FeO, Fe_3O_4 and α-Fe_2O_3 do not show phase transitions above a certain coverage. FeO is a Fe-O bilayer, which grows epitaxially on the Au(111) support and exposes the FeO(111) surface. Under oxidative conditions, the lattice of FeO_x remains with a hexagonal (111)-like periodicity; however, the height varies from monolayer FeO(111) to multilayer Fe_3O_4(111) and Fe_2O_3(0001) structures, STM images are shown in figure 1-12[55].

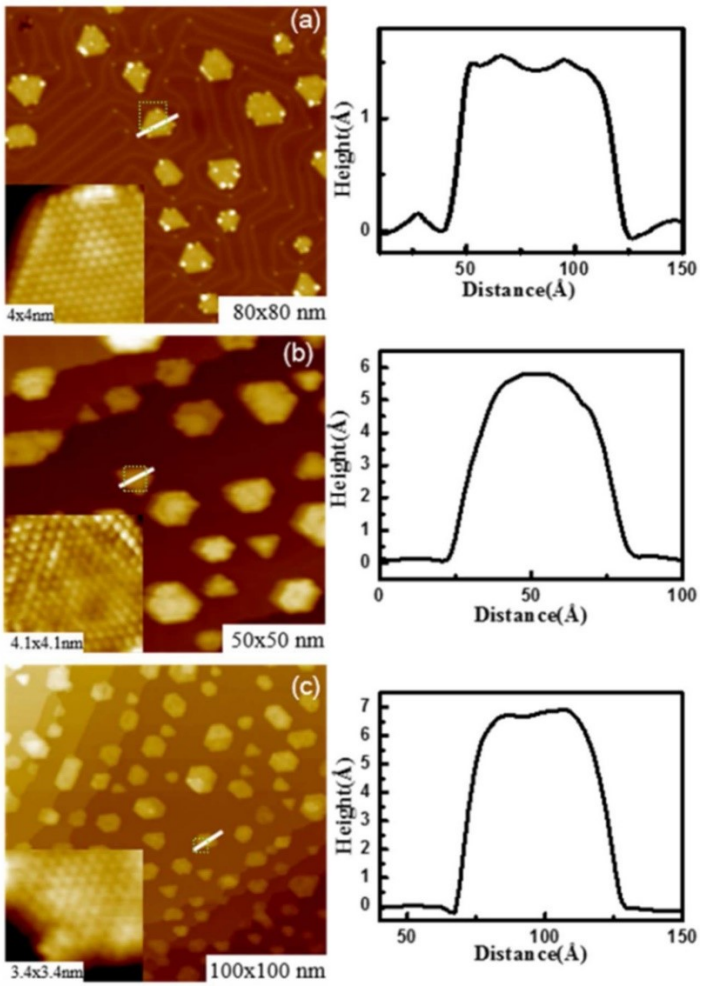

Figure 1-12: STM images of (a) FeO, (b) Fe_3O_4 and (c) Fe_2O_3 nanostructures on Au(111). The corresponding apparent heights of these nanostructures, as marked by white lines in STM images, are plotted on the right side of the STM image. Inset of each STM image shows the atomic resolution of nanostructures. Scanning parameters for each inset image are a) U_T = 0.05 V, I_T = 2.0 nA; b) U_T = 0.5 V, I_T = 3.0 nA; c) U_T = 0.1 V, I_T = 1.9 nA. Reproduced from Ref. 55.

FeO/Au(111) exhibits a Moiré pattern since the lattice constants of FeO and Au(111) are slightly different. The FeO/Au(111) lattice constant FeO/Au(111) was initially measured, by Khan and Matranga[50] to be 3.3 Å and the Moiré periodicity (3.4±0.4) nm; ten years later, Yang et al.[51] and Jiang et al.[52] measured 3.16 and 3.15 Å lattice constants and 3.17 and 3.3 nm Moiré periodicities; moreover, Jiang showed a model in which a 10x10 FeO cell is in a commensurate relation with a 11x11 Au(111) cell (assumed to be compressed by 0.7%), with a Moiré periodicity of 3.15 Å, in good agreement with experimental data. Yang, on the other hand, proposed an atomic model with lattice constant 3.16 Å, coincidence structure periodicity 3.20 nm and a rotation of 9.8° between the Moiré pattern and Au(111).

The FeO/Au(111) lattice constant is stretched with respect to the one of the bulk FeO, 3.07 Å, due to interface interactions. The height of the FeO NPs, which consist of a layer of Fe atoms and one of O atoms, is ≈1.7 Å[50,55]. FeO is not the most stable Iron oxide, as visible in the Fe-O_2 phase diagram in figure 1-8, the hematite (Fe_2O_3) and magnetite (Fe_3O_4) phases are more stable at temperatures below 800 K and pressures of approximately 10^{-10}-10^{-7} mbar. However, the formation of more stable Iron oxide phases, such as Fe_2O_3 and Fe_3O_4 requires multiples layers of Iron and Oxygen to achieve one full unit cell. Therefore, the Iron monoxide described above is stabilized by the Au(111) surface underneath. Moreover, the FeO/Au(111) is a polar surface, with O atoms facing the vacuum and Fe atoms in contact with the Gold surface.

Deng and Matranga[53] showed that α-Fe_2O_3 NPs adopt a more three-dimensional structure, with heights between 5 and 6 Å and a hexagonal unit cell with a lattice constant of ≈3 Å, in agreement with an O-terminated α-Fe_2O_3(0001) surface. At low coverage, α-Fe_2O_3 forms small particles, adopting either a triangular or hexagonal shape, increasing coverage irregular hexagonal shape are found with a few having more elongated shapes, some particles start to coalesce and at 1 ML coverage islands are large with irregular shape, moreover, they cover only ≈80 % of the Au(111) surface consistent with a three-dimensional island growth mode.

In this thesis we defined one monolayer equivalent (MLE) equal to an hypothetic full coverage of Au(111) with Fe_3O_4 which are technically two couples of atomic bilayer of Fe and O. The MLE has been calibrated by STM imaging on a subMLE sample with no Fe_3O_4 multilayers island were formed.

Deng and Matranga, in a successive study[54], characterized Fe_3O_4 NPs on Au(111), produced by partially reducing through annealing in UHV the α-Fe_2O_3 particles. They observed irregular hexagonal shape NPs with sharp edges, showing a hexagonal lattice with ≈3 Å periodicity (O terminated Fe_3O_4(111) surface) and observed also two different ordered hexagonal superstructures, named structure 1 and structure 2, with different periodicity, ≈50 and ≈42 Å, and different height, ≈6 and ≈7 Å, respectively; NPs and the two different superstructures are shown in figure 1-13. In this thesis, higher and larger NPs were obtained, see paragraph *3.3.4*, due to the different growth conditions.

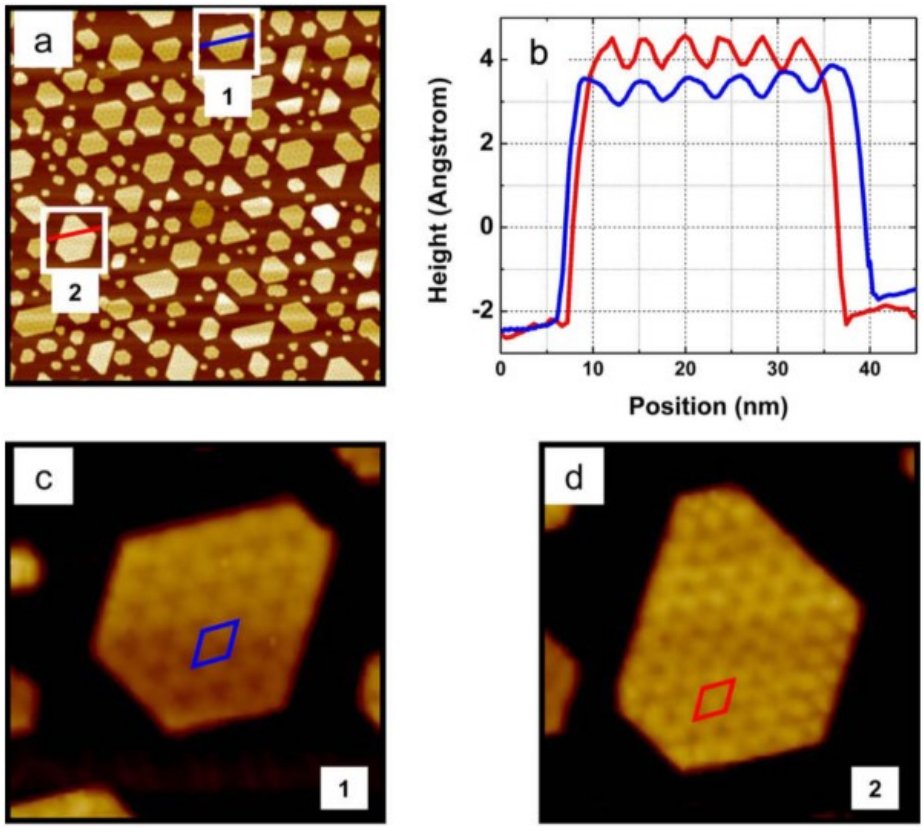

Figure 1-13: Room temperature STM images of Fe_3O_4 on Au(111). (a) 300 x 300 nm^2 (I_T = 50 pA, U_T = 1.0 V), (b) linescans of structures 1 and 2 shown in panel a, (c) enlarged image of structure 1 (50 x 50 nm^2, I_T = 50 pA, U_T = 1.0 V), (d) enlarged image of structure 2 (50 x 50 nm^2, I_T = 50 pA, U_T = 1.0 V). Adapted from Ref. 54

2 Materials synthesis and Characterization methods

2.1 Gold Single Crystal Au(111)

The Gold Single Crystal Au(111) used was purchased by MaTecK and is shown in figure 2-1. It is hat shaped to fit in the sample holder; being polished on the top side (where materials are deposited), it has roughness lower than 30 nm. The orientation accuracy is lower than 0.1°. The Gold purity is 99.999%. Before each experiment, the Au(111) was cleaned through Ar^+ sputtering (1.5 kV, 15 µA of ion current) and annealed for 30 minutes at ≈800 K *via* a Pyrolitic Boron Nitride heater (3.0 A, 5.5 V), with slow ramp for heating and cooling (35 K/min and 18 K/min, respectively).

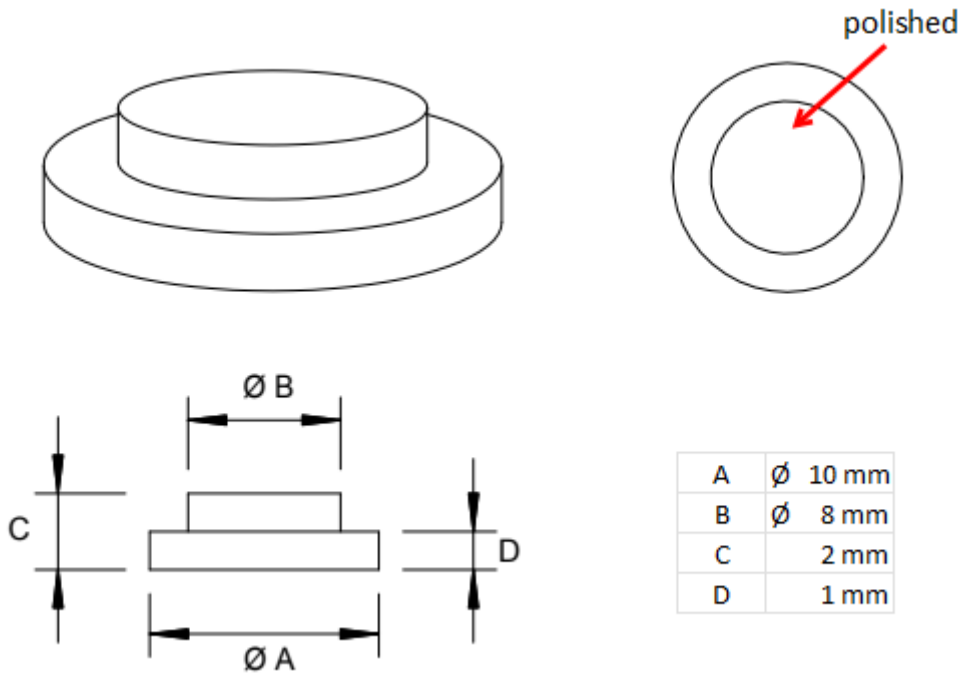

Figure 2-1: shape and dimensions of Au (111) used.

2.2 Iron Oxide

Iron was deposited on the Au(111) by means of physical vapour deposition (PVD) through an electron-beam evaporator (EFM3, Focus GmbH), shown in figure 2-2 on the left[67], with integrated flux monitor (voltage 1000 V, filament current ≈3.9 A, emission current 15.0 mA, flux 0.08 NA). The deposition was homogeneous, since the Iron

molecular beam cone section at the experimental distance nozzle-substrate (22cm) is larger than the Gold substrate itself, figure 2-2 on the right[68].

After Fe deposition, annealing in oxidative atmosphere, dosing molecular Oxygen via a leak valve ($p_{O_2} = 5 \cdot 10^{-7}$ Torr), at T≈800 K was conducted.

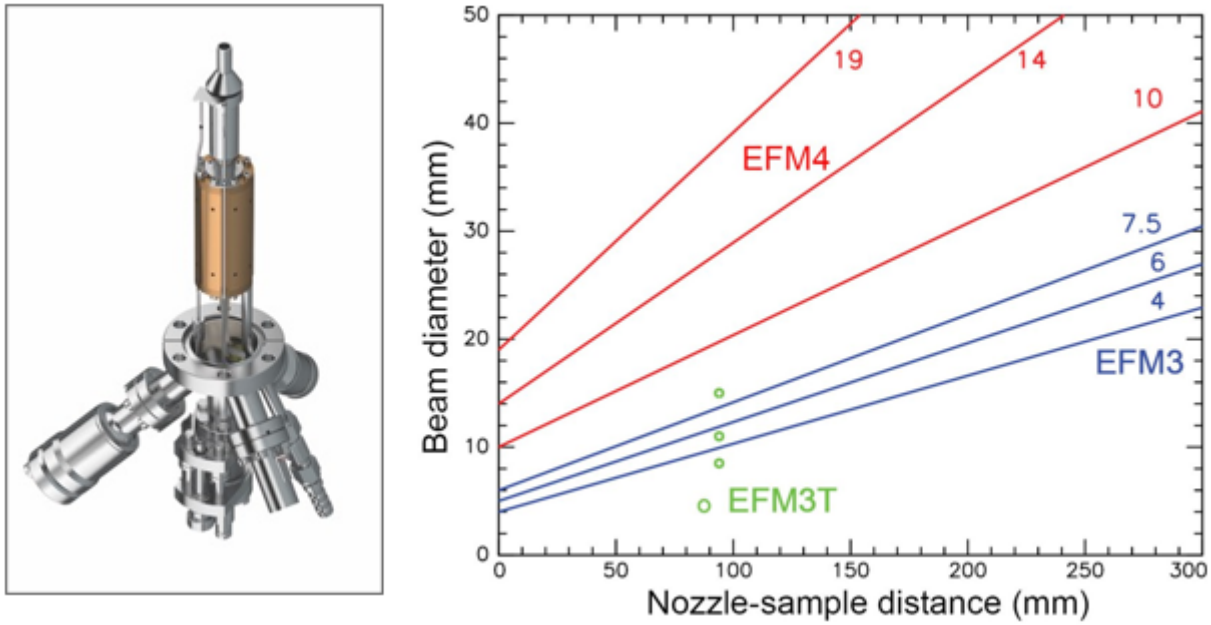

Figure 2-2: Left: evaporator used; Right: plot showing the dependance of the Iron beam diameter on the nozzle-sample distance. Adapted from Refs. 67-68.

2.3 Mn deposition

On a Fe_3O_4/Au(111) MLE substrate, Mn was deposited via Metal Organic – Chemical Vapour Deposition (MOCVD) adapted to UHV conditions. The precursor chose was $Mn_2(CO)_{10}$, shown in figure 2-3[69], which give the possibility to deposit Mn dimers, namely Dual Atoms (DAs). It was heated up to 90-100 °C (its decomposition occurs at temperatures higher than 110 °C[70,71] to increase its vapour pressure (which at room temperature is ≈ 6.82 Torr[70] and dosed *via* a leak valve at a pressure of $4 \cdot 10^{-6}$ Torr, with the substrate kept at room temperature.

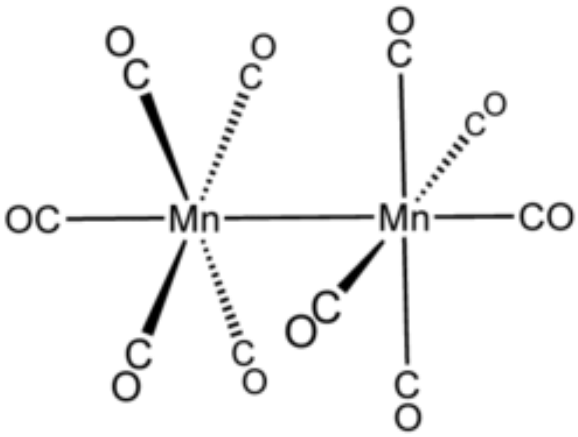

Figure 2-3: Molecular structure of $Mn_2(CO)_{10}$. Reproduced from Ref. 69

2.4 X-ray Photoelectron Spectroscopy

XPS is a technique that allows to identify the elements that compose a surface and most importantly their chemical states. It takes advantage of the photoelectric effect described by Einstein in 1905[72], according to which the atoms of a sample irradiated with enough high energy photons can ionize and emit a number of photoelectrons directly proportional to the intensity of the incident light. If the photoelectron is emitted from the surface of the sample, and it does not undergo inelastic scattering, its kinetic energy (KE) is given by the difference between the energy of the incoming photons (hv), the energy which bound the electron to the atom, i.e. binding energy (BE), and the sample's work function in vacuum Φ_S:

$$KE = hv - BE - \Phi s$$

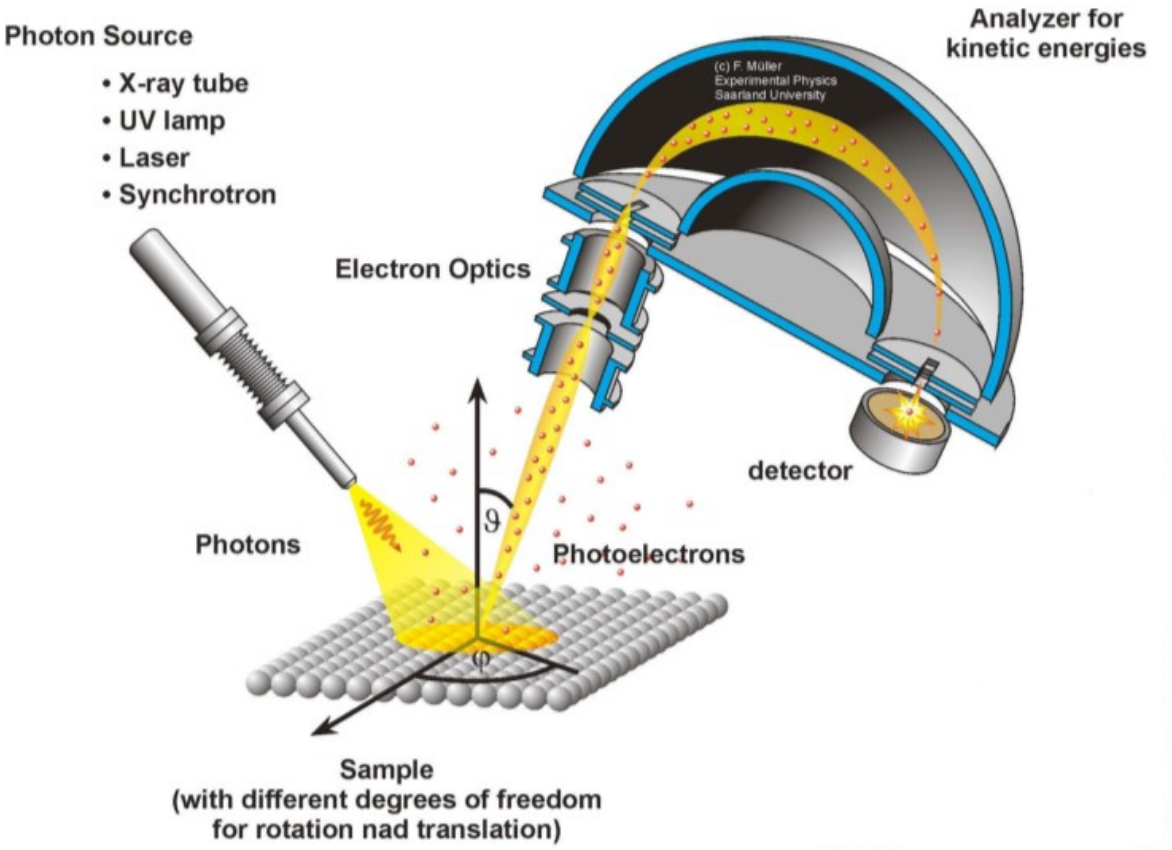

Figure 2-4: scheme of the typical XPS setup. Reproduced from Ref. 73

As shown in figure 2-4[73], an analyser for kinetic energies is in charge of the collection of the photoelectrons. The analyser itself possesses a work function Φ_A, which shifts the measured value of kinetic energy KE' from its real value KE, provided that the Fermi Levels of the sample and the analyser are at the same energy, being in electrical contact:

$$KE' = KE - (\Phi_A - \Phi_S) = h\nu - BE - \Phi_S - (\Phi_A - \Phi_S) = h\nu - BE - \Phi_A$$

That considered, the BE of the photoemitted electron results:

$$BE = h\nu - KE' - \Phi_A$$

This is a fundamental equation for XPS analysis: given that the photon energy is known, the photoelectron energy is measured, and that the work function of the analyser is empirically found by setting the energy scale to zero at the Fermi edge of reference samples, it is possible to determine the electron BE. By comparing the peaks at specific BEs that arise from a spectrum with those in literature[74], it is possible to qualitatively

and quantitative identify which elements are present in a sample. Oxidation states can be determined as well: for example, an oxidized element has a lower electron density than its neutral or reduced counterparts, so the remaining electrons experience a lower screening of the nuclear positive charges and, thus, have a higher BE. The opposite goes for an element in a reduced state, in which electrons show lower BEs due to a more effective screening given by the higher electron density. Because of this characteristic, by deconvoluting a photoemission peak in its components it is possible to deduce the various chemical states of a given species.

Depending on the atomic orbital considered, the photoemission peak shapes can vary greatly. Electrons from s orbitals present only one line, while electrons form p, d and f orbitals all exhibit a splitting due to spin-orbit coupling. The coupling between orbital and spin momentum is described by the quantum number $j = |l \pm s|$, where l defines the orbital and s the spin. The splitting typically grows with the atomic number and the degeneracy is equal to $2j + 1$. Due to this, given for example a p orbital ($l = 1$), the two observed peaks are named $p_{1/2}$ and $p_{3/2}$ and have a constant area ratio 1:2, whereas for a d orbital ($l = 2$) the peaks are named $d_{3/2}$ and $d_{5/2}$ and have a constant area ratio 4:6. The line shape of a singular well defined photoemission peak is theoretically a Lorentzian function, with a natural line width ΔE_0 which depends on the lifetime of the core hole state left by the photoemission process, according to the energy-time uncertainty principle[75]. However, due to temperature-dependent atomic vibrations, complex final states, chemical environment and instrumental broadening of the peaks, photoemission lines are better described by a Voigt function, i.e. a convolution of a Gaussian and a Lorentzian curve. In our case, the biggest factor of uncertain is the not-monochromatic X-Ray source which induces a broadening of the XPS lines of 0.9-1 eV.

A very important feature of XPS spectra of first row (2p) transition metals, as Fe and Mn, is the presence of shake-up satellites[76]. When a core electron is photoejected, the coulombic potential experienced by the outer shell electrons is suddenly altered. This sudden perturbation may induce a “shake-up” transition, involving the excitation of a valence electron to a higher, previously unoccupied orbital[77]. The shake-up process is thought of as taking place simultaneously with core electron photoejection. If shake-up

occurs, the KE of the ejected core electron will be less than that of an electron ejected from a corresponding core orbital in another atom where shake-up has not occurred. Consequently, “shake-up” satellites always appear on the higher BE side of the main peaks.

In the analysis of the XPS spectrum of Fe and Mn, also multiplet splitting must be taken into account. Multiplet splitting arises when an atom contains unpaired electrons. In these instances when a core electron vacancy is formed by photoionization there can be coupling between the unpaired electron in the core with the unpaired outer shell electron. This can create a number of final states, which will manifest in the photo-electron spectrum. Thus, low-spin Fe(II) and Mn(VII) will not show multiplet splitting, since they do not have unpaired *d* electrons, whereas Mn(II), Mn(III), Mn(IV), Mn(VI) and high spin Fe(II) and Fe(III) will. Given the experimental resolution reachable with common XPS instrumentation, the multiplet splitting does not cause the presence of additional peaks, but only results in the broadening of the peak.

To interpret XPS data of complex lines, such as the Fe 2p, one can adopted the procedure based on Gupta–Sen multiplets[78,79] developed by Biesinger[80,81].

Besides the electrons emitted because of the photoelectric effect by core level and valence bands, Auger peaks can also be found in an XPS spectrum. In fact, after an atom has been ionized, its relaxation process can occur by either X-ray fluorescence or by Auger electron emission. The former is typical of heavier elements, with atomic number above 35, whereas lighter elements tend to relax via the Auger mechanism. In this case, electrons are emitted with a constant KE that is independent from the incoming photon energy: given for example the relaxation of a L1 electron to the K hole with emission of a L2 Auger electron, its kinetic energy is in fact $KE = (BE_{L1} - BE_K) - BE_{L2}$. Because of this property, Auger lines are found at different (apparent) BEs with different X-ray sources (since the energy of the incoming photon hv changes), but at the same KE values.

XPS is a technique with significant surface sensitivity. In fact, even though X-rays penetrate ≈1μm of material and so excite photoelectrons until that depth, only the ones

ejected from the outermost 10 nm can emerge from the sample with a non-zero KE and reach the analyser. The probability of an electron to keep its KE unchanged (i.e. to not undergo inelastic events) decays exponentially with the travelled distance, *d*, being the Inelastic Mean Free Path (IMFP, λ) the decay characteristic length:

$$P = \exp\left(-\frac{d}{\lambda}\right)$$

By tilting the sample of an angle θ, the surface sensitivity is enhanced since the electrons photo-emitted at a depth *d* will have to travel a distance $\frac{d}{\cos(\theta)}$; thus, those that reach the analyser belong to a thinner region of surface than if the sample was not tilted.

In our system, a not monochromatic Al-kα X-ray source (1486.7 eV) was employed, a potential was set to 13.0 KV and the power at 150 W. Measurements were taken in Constant Analyzer Energy (CAE) mode; in particular, survey scans, between 0 and 900 eV BEs with a pass energy of 50 eV, were employed to identify the various elements on the sample, and other high-resolution scans with a pass energy of 20 eV were used to obtain more specific information on the oxidation states and area ratios.

2.5 Low Energy Electron Diffraction

LEED is a technique which was effectively developed in the early 1970s but has its roots already in the 1927, with Davisson and Germer's experiments[82]. As suggested by the name, it employs a beam of low energy electrons, between 20 and 500 eV, i.e. with wavelengths between 0.5 and 2.0 Å according to the De Broglie equation: $\lambda = \frac{h}{\sqrt{2m_e E}}$

Electrons are generated via thermionic effect by the electron gun, kept at a negative potential with respect to the sample; thus, electrons are accelerated towards the surface, where they can interfere with the outermost 5-10 Å of the material, given their low mean escape depths. When the beam interacts with a crystalline lattice with atomic distances comparable with the electron wavelength, it can scatter coherently: the electrons are then accelerated and impact on a phosphorescent screen, showing diffraction spots corresponding to the reciprocal lattice points.

X-ray diffraction can study the crystal structure of powders, polycrystalline samples and single crystals; it typically has only one or few radiations available and interact with the bulk of the crystal. Whereas LEED can study the surface of single crystals, easily modify the electron energy and therefore their wavelength, a degree of freedom mostly absent from X-ray sources for diffraction. By measuring the distance from the centre of the diffraction spots, it is possible to deduce the real lattice geometry and cell parameters. The simplest way involves Bragg's law, which states that, given a one-dimensional beam of electrons with wavelength λ incoming on a chain of atoms with interlayer spacing d, positive interference occurs when the following relation is satisfied:

$$d\sin(\theta) = n\lambda$$

where *n* represents the diffraction order, the first order of diffraction (*n*=1) requires that, given a normal incident angle the electron wavelength equals the surface lattice parameter. Other maxima of diffraction beam intensity can be found at other angles and are observed as bright spots on a fluorescent screen. In this configuration the zero order of diffraction coincides with the electron gun position, so it cannot be observed in normal emission but requires tilting the sample[83]. The typical LEED setup is reported in figure 2-5[84].

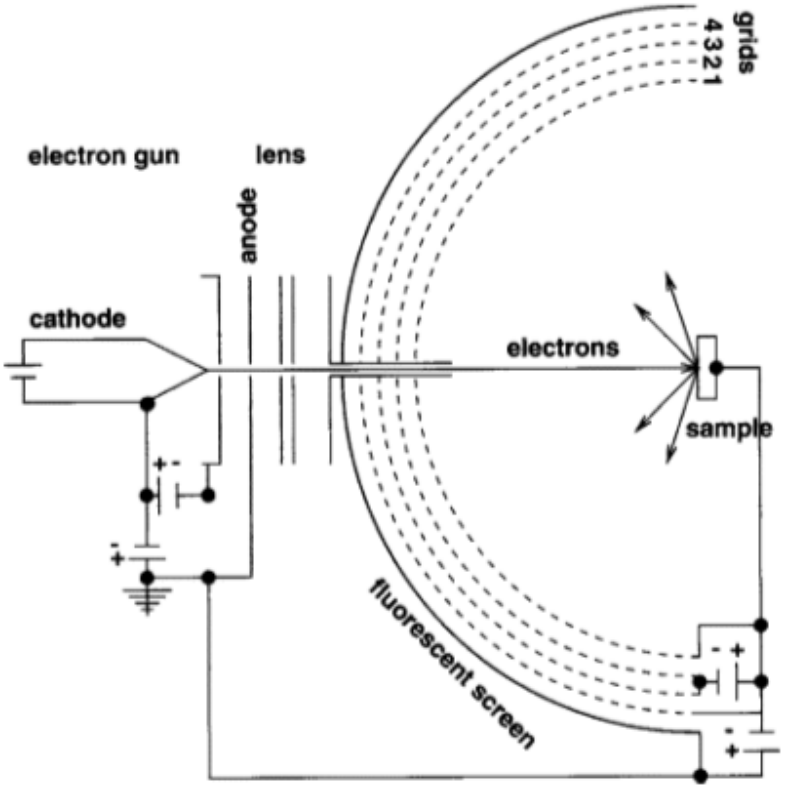

Figure 2-5: scheme of the typical LEED configuration. Reproduced from Ref. 84.

2.6 Electrochemistry

Samples electrochemical activities were studied by means of CVs and LSVs were carried out to obtain the overpotential ($\eta = E - E_{eq}$) needed to reach the arbitrary current density value of 1 mA/cm^2. Other figures of merit can be found as well: the exchange current density j_0, related to the intrinsic kinetics of the electrochemical reaction, and the onset potential, defined as the first potential at which the reaction can occur, represents the bypassing of the thermodynamic barrier and the entrance in the potential region in which the RDS is the electron transfer, but there is no a unique method of calculating it. The Tafel slope, although frequently used, can be an interesting but misleading parameter about the RDS of the reaction. On the other hand, the exchange current density is a strong indicator of the electrode kinetics which can be calculated from the micro-polarization region, and the evaluation of a potential value at an arbitrary current density far enough from the diffusion limited region allows to compare different

samples in a reliable way. As described by the Butler-Volmer theory, the exchange current density is given by:

$$j_0 = nFC_0^* K^0 \exp\left(-\frac{\alpha nF(E_{eq} - E^\circ)}{RT}\right)$$

It is the current density passing through an electrode in both directions when $E = E_{eq}$ or, in other words, when the overpotential and the net current density are null. K^0 is defined as the standard kinetic constant of electron transfer and, just like the exchange current, does not depend on the applied potential, therefore it can be used to compare different electrodic processes at equal temperatures, being solely dependent on the intrinsic activation barrier: $K^0 = Z\exp\left(-\frac{(\Delta G^{\neq})_0}{RT}\right)$, being Z a pre-exponential factor which depends on the mass of the reagents and of the products.

The Butler-Volmer equation is the following:

$$j = j_0\left[\exp\left(\frac{(1-\alpha)nF\eta}{RT}\right) + \exp\left(-\frac{\alpha nF\eta}{RT}\right)\right]$$

At low overpotential, i.e., close to equilibrium region in which $\eta \ll RT/\alpha nF$, the exponentials can be expanded in series, truncating at the second term:

$$j = j_0\left[1 + \frac{(1-\alpha)nF\eta}{RT} - 1 + \frac{\alpha nF\eta}{RT}\right] = j_0\left[\frac{nF\eta}{RT}\right]$$

The first order derivative of the overpotential with respect to the current density represents the resistance associated to the electron transfer, and its calculation allows to determine the exchange current density:

$$j_0 = \frac{RT}{nF}\left(\frac{\partial\eta}{\partial j}\right)^{-1}$$

2.6.1 Water Electrolysis

Water electrolysis is the chemical reaction in which water is converted to H_2 and O_2 through application of electrical energy, given the reaction:

$$2H_2O \rightarrow 2H_2 + O_2$$

At the cathode the HER occurs, while at the anode Oxygen is produced by OER. The half-reactions and mechanisms are different according to the acidity or basicity of the electrolyte. In acid conditions the half-reactions are:

$$\text{Cathode: } 2H^+ + 2e^- \rightarrow H_2$$
$$\text{Anode: } 2H_2O \rightarrow O_2 + 4H^+ + 4e^-$$

In acidic conditions, the HER starts with the proton adsorption to the catalyst's active site, also known as the Volmer step:

$$\text{Volmer step: } H^+ + e^- \rightarrow H_{ad}$$

Followed by the formation of the H_2 molecule on the surface, that can be both electrochemical (Heyrovsky step) or just chemical (Tafel step):

$$\text{Heyrovski step: } H^+ + e^- + H_{ad} \rightarrow H_2$$
$$\text{Tafel step: } 2H_{ad} \rightarrow H_2$$

In acid, the Tafel slope is used to assess the RDS of acid HER on a certain material. According to the Sabatier principle, the most active catalyst, so the one with the highest exchange current j_0, should show a not too weak nor too strong adsorption of the proton, thus, an intermediate HBE.

In alkaline conditions[12–14], Heyrovsky and Volmer steps are described with water rather than protons as reactants:

$$\text{Volmer step: } H_2O + e^- \rightarrow H_{ad} + \text{OH}^-$$
$$\text{Heyrovski step: } H_2O + e^- + H_{ad} \rightarrow H_2 + OH^-$$

Therefore, four factors might influence the performance of a catalyst in alkaline HER: water adsorption on active sites, water dissociation ability, HBE and adsorption strength of aqueous OH^-.

2.6.2 Equipment and methods: electrochemistry in-situ

In this thesis, it was used an electrochemical cell directly connected to the vacuum system, figure 2-6 at the top; to allow the characterization of the electrochemical behaviour and catalytic activity of a sample created under UHV conditions, see paragraphs *2.2* and *2.3*, without exposing it to air, which leads to a strong and mostly uncontrollable oxidation of the surface and a contamination due to adventitious carbon species.

The in-situ electrochemical cell was made of three electrodes: the working electrode (WE), onto which the catalyst to study is grown (in our case the Au(111) crystal); a counter electrode (CE), through which the opposite current of the WE passes, so to close the amperometric circuit, which is usually made of an inert conductive material (a Gold filament, in this thesis); and lastly the reference electrode (RE), an unpolarizable electrode that is used as a reference for the potential applied to the WE and to close the potentiometric circuit. The RE employed for this thesis was an Ag/AgCl micro-electrode (SSC, Silver Silver Chloride) constructed without the use of glass, thus suitable for alkaline conditions.

To carry out measurements, the pressure in the in-situ EC chamber needed to be taken up to atmospheric pressure venting in ultrapure Ar. The electrolyte, KOH 0.1M, was degassed with Ar for at least 40 minutes, then fluxed by means of a syringe pump through a system of tubes. The electrolyte was confined to the surface of the WE with a pressed O-ring. Measurements were taken mainly with still electrolyte, fluxing it was found useful to evaluate the oxidation of Iron soluble species (paragraph *3.5.1.1.1*).

Samples were cycled between -0.25 and +1.55 V vs the Reversible Hydrogen Electrode (RHE) until stabilization of the CV (10 cycles). CVs were then recorded at a scan rate of 20 mV/s broadening the potential range cathodically to include HER and so the reduction peak to metallic Iron (see Chapter *3* for more details). LSVs to study the HER were taken at a scan rate of 50 mV/s between 0.7 and - 0.65 V vs RHE.

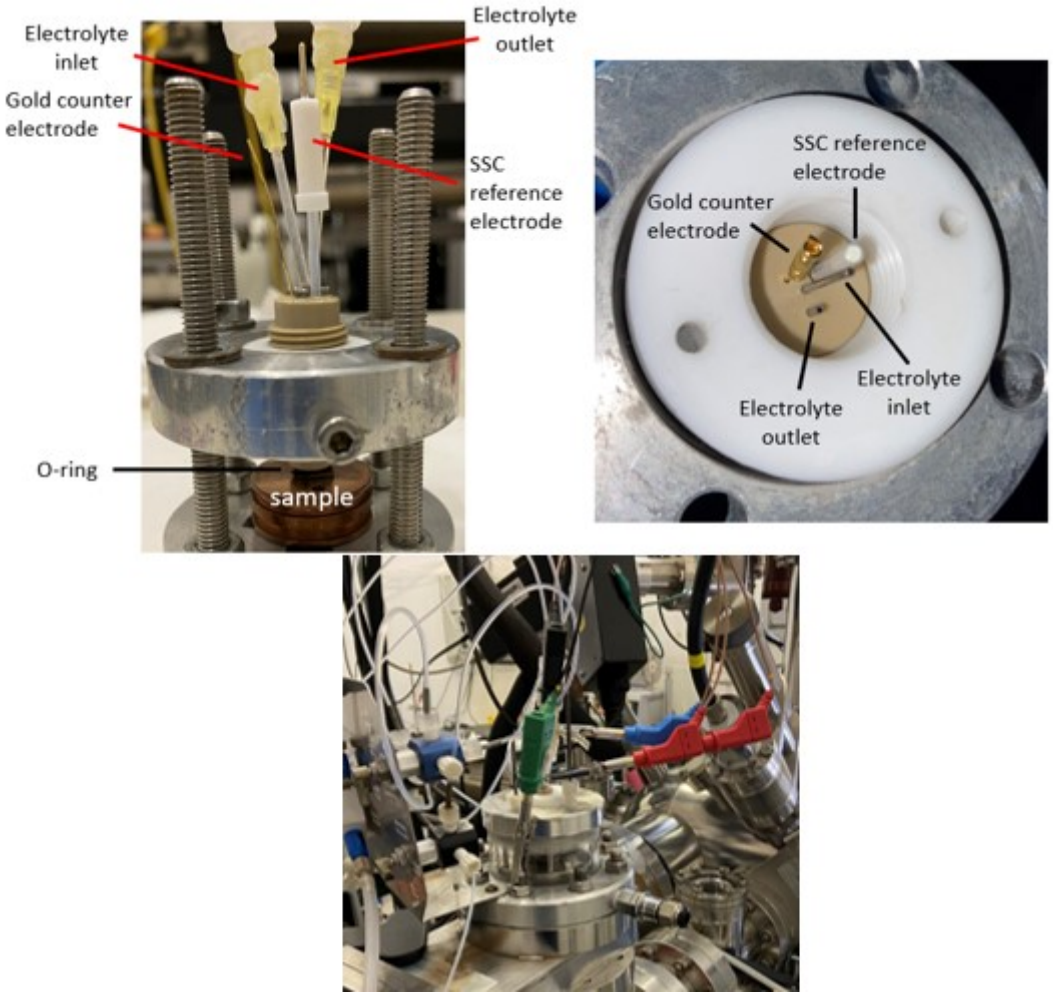

Figure 2-6: top) in-situ EC cell used; bottom) in-situ EC cell connected to the vacuum system, tubes for electrolyte and electrical connections are visible.

2.7 Scanning Tunneling Microscopy

STM exploits the electron tunnelling effect to investigate the local density of states of a sample. Its most important use is probably the direct real-space determination of the materials lattices and superstructures. Given a high enough resolution, it allows to observe the surface lattice distances, to measure the steps' height and terraces and to inspect the density of states of the material below the probe. In a nutshell, STM uses a sharp metal tip (usually made of tungsten or platinum-iridium alloy), ideally with a single apex atom extremity, positioned at just few angstroms above the sample surface, as shown in figure 2-7[85]. The sample is moved by piezo-electric crystals with atomic scale precision, in order to scan a square or rectangular area. At this distance, given the application of a bias voltage between the tip and the surface, electrons can overcome

the vacuum potential barrier and tunnel from one end to the other, depending on the sign of the bias. Two main modes of operations exist: one at constant height, in which the tip is kept at the same vertical position as it is scanned over the surface, so that the measured current depends on the topography of the sample, given that it is chemically homogeneous; or at constant current, which requires the tip-sample distance to be constant. Such mode is possible thanks to a feedback system which, when the detected tunnelling current deviates from the set one due to a change of the topography, quickly adjusts the vertical position. This is the scanning mode that has been used in this work, as it allows to distinguish steps, kinks, defects and even to achieve atomic resolution images.

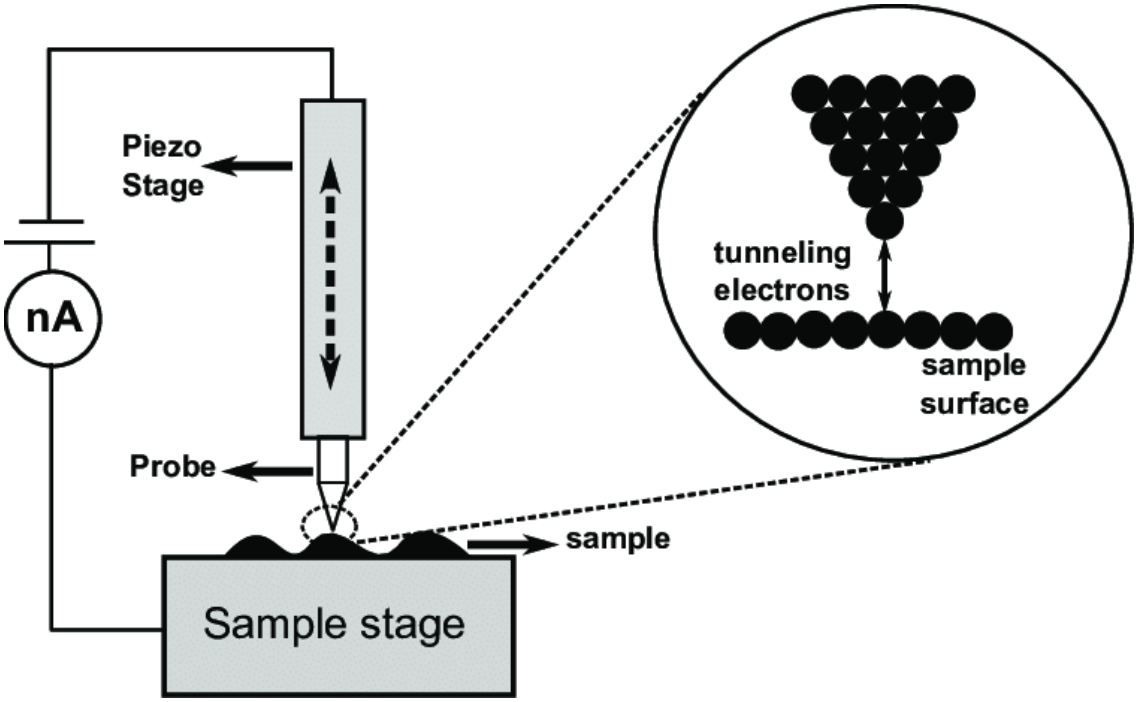

Figure 2-7: basic scheme of a STM setup. Reproduced from Ref. 85.

2.7.1 Tunnel effect

In classical mechanics a particle cannot overcome a potential barrier if it does not possess enough total energy to surpass it but is rather reflected or absorbed (in the case of a physical barrier). On the other hand, according to the quantum theory the particle has a non-zero chance to tunnel through the barrier.

The probability of tunnelling between the sample and the tip (or viceversa) is given by the product of the moduli of the sample electron's wave-function times the one of the tip. Without any bias applied, the probability for the electrons to tunnel from the tip to the sample and viceversa are equal, so the net current is null. The tunnelling current is directly proportional to the probability of finding an electron between the sample and the tip:

$$I \propto |\psi_\nu(0)|^2 \left|\psi_\mu(d)\right|^2 e^{-2\frac{\sqrt{2m\phi}}{\hbar}d}$$

consisting of two main parts, one relative to the probability of having electrons available to tunnel (full states) and available empty states to accommodate tunnelling electrons in the probe (or in the sample, if electrons are going there), and one depending on the work function ϕ and distance *d*. In the Wentzel-Kramers-Brillouin approximation, in fact, by integrating the density of states in a $d\varepsilon$ energy interval, one can find that:

$$I \propto \int_0^{eV} \rho_\nu(E_F - eV + \varepsilon)\rho_\mu(E_F + \varepsilon)\, T(\varepsilon, eV) d\varepsilon$$

$$\text{given: } T = \exp\left(-\frac{2d\sqrt{2m}}{\hbar}\sqrt{\frac{\phi_\nu + \phi_\mu}{2} + \frac{eV}{2} + \varepsilon}\right)$$

This shows a strong dependence of the current on the distance but also that, in the constant current mode, the applied bias is a parameter through which one can choose which states are probed. This allows to inspect not only the topography of an area, as the tip distance from the surface changes to keep the current constant, but also the electronic contrast: for example, in a region at the same height but with lower work function, electrons will find easier to tunnel, then the current will increase and so the tip will get further from the surface, so in the recorded image this region will seem to be higher.

When the sample is polarized positively, its empty states receive electrons and are inspected, whereas the sample bias is negative, the electrons move from the filled states of the sample to the tip, as shown in figure 2-8[86]. In this way it is possible to detect the energy of the surface electrons and where the electron density is higher.

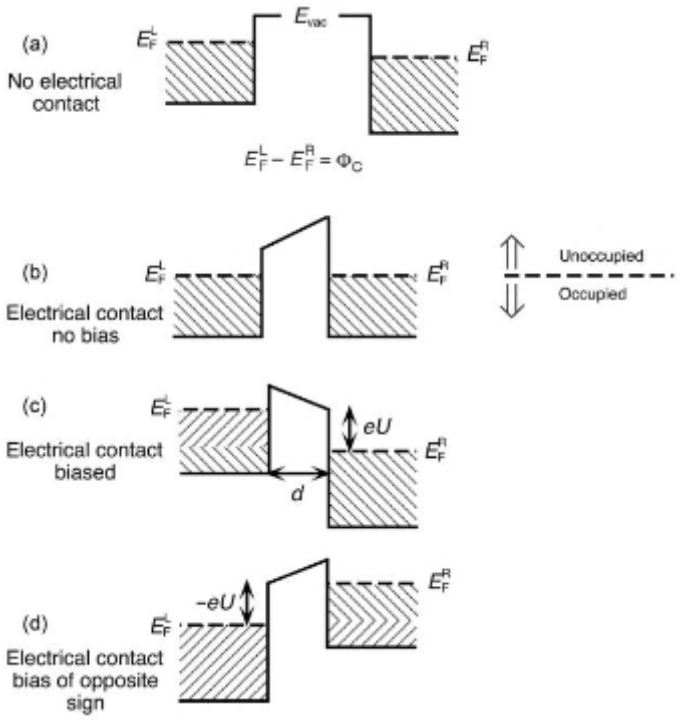

Figure 2-8: effect of changing sample bias on electrons tunnelling. Reproduced from Ref. 86.

2.8 EC-STM

It must be remarked that STM was originally developed to work under UHV conditions, since the first subject of investigation were mainly represented by model surfaces; nowadays, it is still used under UHV conditions in most of the cases. To avoid contamination from adsorbed gases, pressures less than 10^{-10} mbar were and are still needed.

The time limit for surface contamination (i.e. formation of a monolayer of adsorbed species) can be calculated in the simple case of unitary sticking coefficient. The sticking coefficient *S* is a measure of the tendency of a species to adsorb (stick) onto a surface, and it is defined as the ratio of molecules impacting on the surface versus the number of molecules that stick on it. Sticking coefficients therefore range from 0 (no adsorption) to 1 (maximum adsorption). Since the surface concentration of atoms is typically in the order of $10^{15}\ \frac{atoms}{cm^2}$, and upon assuming *S*=1, at a pressure of 760 Torr the corresponding time for surface contamination is 3.44 10^{-9} s. For a pressure of 10^{-9} Torr, the monolayer formation time is 2.61 10^3 *s* (≈45 min).

The sticking coefficient is strongly dependent on many factors, like temperature, surface coverage, exposed crystallographic face and of course it changes according to the adsorbing molecule. Considering Au(111), the problem of contamination seems to represent a minor issue. Indeed, Au(111) is known to have low tendency to contamination[87], however transition metal and their oxides have a tendency of adsorb species on the surfaces.

A great progress of Scanning Probe Microscopy techniques, like STM, is that they have been extended to environments different from UHV, i.e. air or, more interestingly, a liquid phase. This opened the route to extensive solid/liquid interface studies, and to all the phenomena linked to this special interface.

However, when working at the solid/liquid interface, additional considerations must be made. The solid/liquid interface defines in fact a region of finite thickness, in which different properties, with respect to the bulk phase, can arise. For this reason, this region of finite thickness is often named as interphase, being the interface the exact place where the two phases come in contact. The solid phase can in fact perturb the liquid one, for example due to excess charges that metals frequently exhibit at their surfaces[88]. Whereas the liquid phase can modify the solid surface since it could provide ions able to adsorb on the solid surfaces.

The investigation of solid/liquid interface is crucial to visualize the microscopic nature of matter in realistic environment, nowadays STM in liquid is able to resolve atoms and molecules.[88–90].

A special case arises when the liquid is represented by an electrolytic solution. The idea is to perform in operando STM in electrochemical environment (EC-STM), thus under potential control of the sample, which plays at the same time as WE of a “Four-Electrode Setup”, shown in figure 2-9.

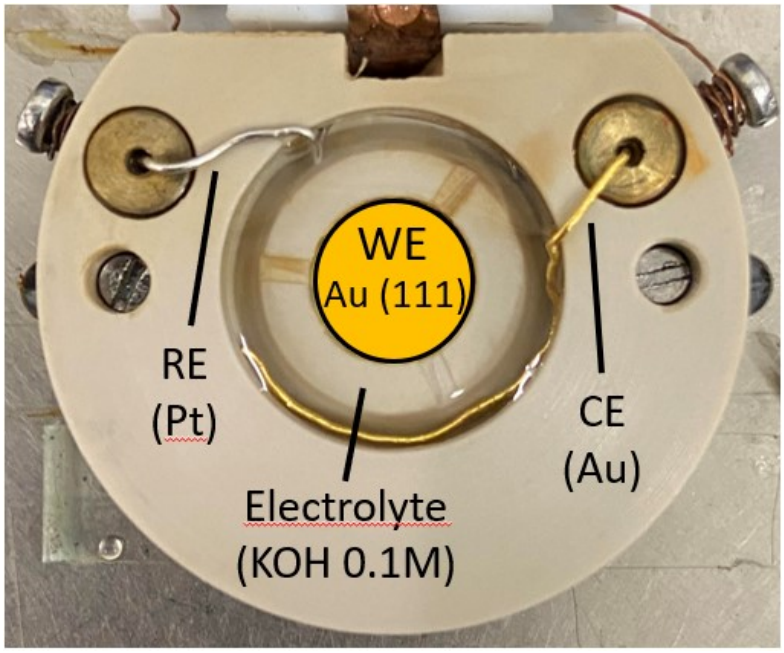

Figure 2-9: EC-STM cell used.

To manage both the electrochemical signals, i.e. the WE current (I_S) and the potential of WE vs the RE (U_S), and the tunnelling parameters, i.e. the tunnelling current (I_T) between the sample and the tip and the tunnelling bias (U_T) of the sample vs the tip, a bi-potentiostat, shown in figure 2-10[91], is necessary. Moreover, being the tip made of metal, it must be covered, ideally letting uncovered the only last few atoms at the extremity, with insulating glue to avoid any faradaic current between the tip and the CE to exist, since it would disturb the tunnelling current signal.

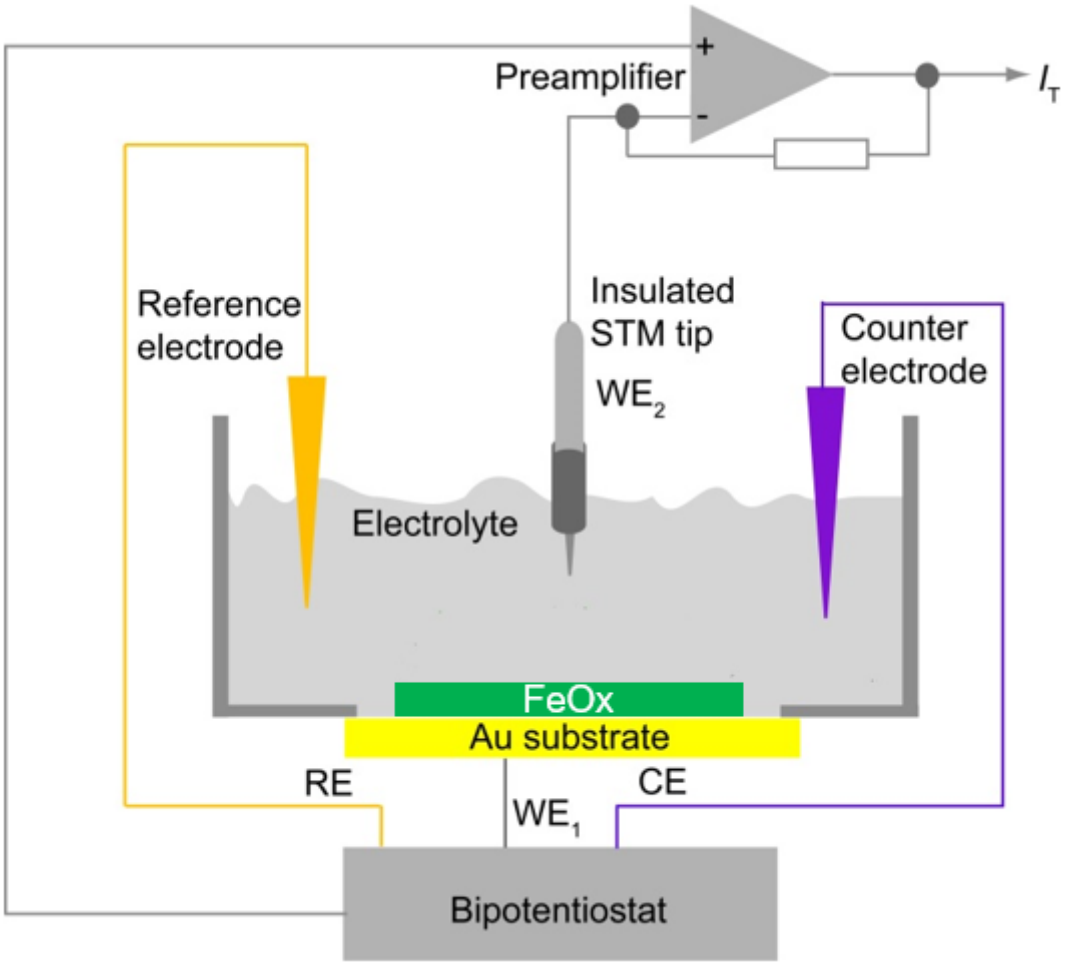

Figure 2-10: schematic illustration of the EC-STM apparatus. Adapted from Ref. 91.

It is important to highlight that potentials used (WE vs RE and WE vs tip) are bound, as shown in figure 2-11; two operational modes are then possible: one with the potential of the tip vs the RE, $U_{t\text{-}R}$, fixed (so changing U_S ends in a change of the same quantity, in modulus, in U_T), the other with U_T fixed (so changing U_S leads to the same change in $U_{t\text{-}R}$).

The fixed $U_{t\text{-}R}$ mode allows to have electrochemical stability of the tip, avoiding/minimizing faradaic current between the tip and the CE; however, it imposes to change the tunnelling bias U_T when changing the sample potential U_S, resulting in a modification of the tunnelling conditions that must be taken into account at the stage of data analysis.

On the other hand, the fixed U_T mode allows to keep unchanged the tunnelling conditions but with the risk of spanning potential regions in which the tip is not stable. Usually this mode is preferred, but, before to start scanning, the CVs of the sample and of the tip (I_S and I_{tip} both vs U_S) are taken and used as benchmark during the whole measurement, to avoid polarizing the sample in potential region in which the tip would be unstable.

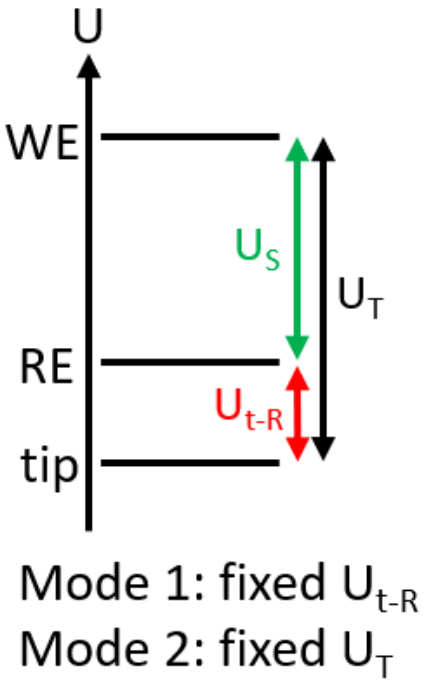

Figure 2-11: scheme of the relative potential levels of WE, RE and tip.

This powerful technique gives the possibility to investigate in-operando a system at a peculiar solid/liquid interface, offering in addition the ability to tune its behaviour upon proper polarisation of the sample as WE. In this way, essential information can be obtained for the electrode/electrolyte interface, and electrochemical processes can be controlled, induced, or inhibited.

2.8.1 Tunneling through an electrolyte

When passing from UHV environment to solid/liquid interface, STM imaging becomes more difficult to describe. Many differences arise and a unique tunnelling theory has not been developed yet. Some quantitative approaches have in any case been explored, providing at least experimental evidence as starting points for theoretical considerations.

One solid point is that water plays a role in the tunnelling phenomenon between tip and substrate. As a result, variations of the tunnelling current with the sample/tip distance are detected[92]. In other words, the effective barrier height for electron tunnelling has changed. When tunnelling at the solid/liquid interface, the tip has to deal certainly with an easier contamination, since the high electric fields applied between tip and sample can attract and accumulate impurities in the tunnelling gap[92,93].

Schmickler and Henderson[92,94] modelized a flat metal electrode surface as jellium, the tip as a jellium sphere, and water as dielectric mean. The result was a reduced effective barrier height (≈2-3 eV), if compared to common barrier heights detected in vacuum (≈3-5 eV).

Another approach concerns tunnelling via intermediate states. This means that electrons tunnel from sample to tip (or vice versa) passing through a certain number of intermediate states, which can be represented by hydrated electrons[92,95] or dipole resonances[92,96].

Intermediate states are interpreted as dipole resonances related to water molecules, which form layers covering uniformly the tip electrode surface, as well as the WE surface. The orientation of the molecules and the thickness of the resulting layers can be influenced by several factors, e.g. chemical nature of the electrolyte, crystallographic orientation of the sample, defects on the tip and/or on the sample, along with the presence of adsorbed species. The tip potential also exerts a major effect, since at the very-end tip a strong and inhomogeneous electric field is originated when the bias potential is applied.

Hugelmann and Schindler[93,97] also investigated the effect on the tunnelling current induced by the presence of water layers within the sample-tip gap, showing that a substantially non-exponential decay of the tunnelling current (with respect to the sample-tip distance *d*) occurs at the solid/liquid interface. Their Distance Tunnelling Spectroscopy studies led to the observation of an oscillatory tunnelling probability, whose cause was attributed to the presence of definite water layers within the tunnelling gap; they experimentally proved that the tunnelling barrier height is minimum when

electron tunnelling is maximised across the electronic states of hydrogen[93], thus, tunnelling barrier minima occur each time a water layer is completed within the tunnelling gap.

Even though the exact tunnelling theory in EC-STM has been not determined yet, the INCAT group used this technique to study quantitatively the HER with atomic resolution, providing information as Tafel slope and onset potential for each single catalytic site. This was done by analysing the noise in the tunnelling current (noise-EC-STM).[98,99] Bandarenka et al.[100] initially proposed a qualitative analysis of the noise based on the spatial derivative of the EC-STM tunnelling current signals ($\frac{\partial I_T}{\partial \text{distance}}$), which ultimately produces a broadening in the $\frac{\partial I_T}{\partial \text{distance}}$ profile proportional to the catalytic site activity, then a more quantitative one, coupling macroscopic current measurements on Pt(111) single crystals with microscopic noise-EC-STM measurements on the corresponding surface, also proposing a connection between the turnover frequency and the full width at half maximum of the EC-STM derivative signals.[91]

3 Results and Discussion

3.1 Clean Gold Single Crystal Au (111)

3.1.1 Electrochemistry

3.1.1.1 Cyclic Voltammetry

As shown in figure 3-1, the CV of the clean Au (111), exhibits peaks at potentials above 0.7 V vs RHE, in agreement with literature[101]. Going anodic, the oxidation of Gold starts with the OH^- adsorption at 0.92 V (reversible oxide formation[102], then proceeds with the irreversible oxide formation in two distinct steps, whose peaks are at 1.18 and 1.38 V; the reduction of the irreversible oxide occurs in one single step at 1.05 V, Gold is then reduced reversibly to metal through OH^- desorption (0.87 V).

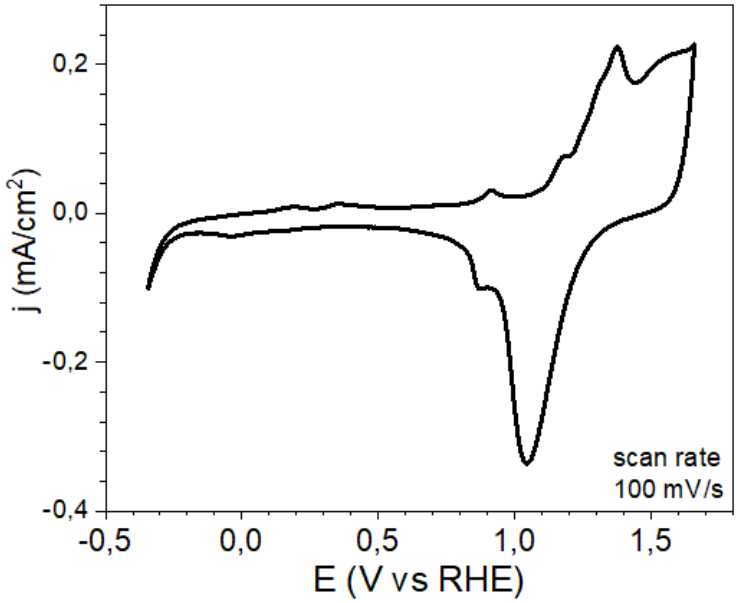

Figure 3-1: CV of Au (111) in KOH 0.1 M

3.1.1.2 Hydrogen Evolution Reaction - Linear Sweep Voltammetry

In the LSV of Au (111), shown in figure 3-2, an onset potential of -0.34 V and an overpotential at 1 mA/cm^2 of -0.62 V are found. Measured currents are low since the Au(111) model system is extremely flat and few atoms are electrochemically involved ($\approx 10^{14}$ in the circle of 4 mm diameter delimited by the O-ring). According to T. Ohmori and M. Enyo[103], the HER kinetics on Gold in basic conditions follows the slow discharge mechanism, with Volmer step as RDS. Moreover, at high concentrations (from $2 \cdot$

10^{-5} to 0.5 M), the under potential deposition (UPD) of the alkali metal takes place concomitantly to HER leading to poisoning of active sites of Gold and thus strongly depresses the electrocatalytic activity[103]. Goyal and Koper[104] calculated a 0.145 V/dec Tafel slope for Au (111) at pH=13, which in quite good agreement with the one calculated in this work.

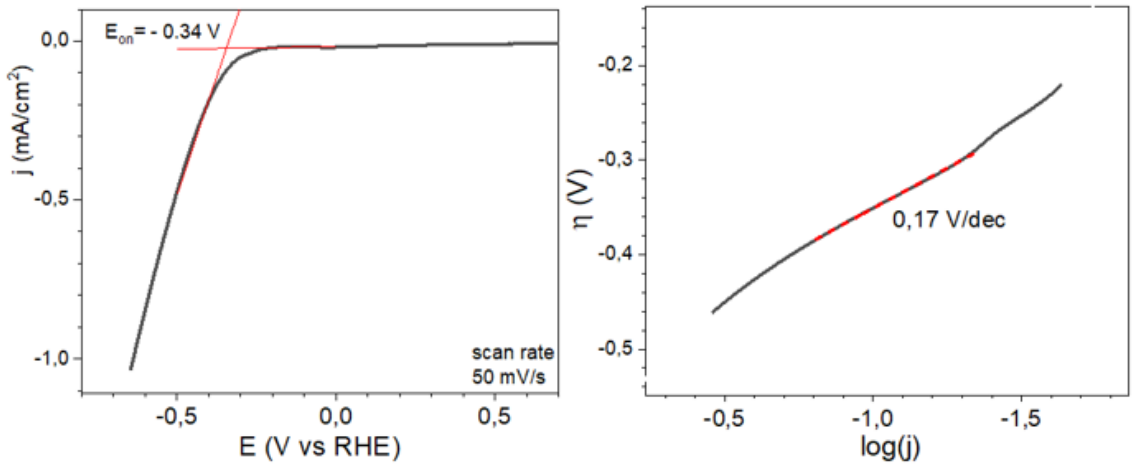

Figure 3-2: Left) LSV of Au (111) in KOH 0.1 M; Right) Tafel plot

3.1.2 XPS

The XPS survey spectrum of Gold agrees with the one reported in literature[74]; as shown in figure 3-3 on the left, it shows several lines detectable with the excitation energy of the Al k_α (1486.7 eV), no Carbon or Oxygen were detected prior the Fe PVD. In figure 3-3 on the right is reported the high-resolution spectra of the $4f_{7/2}$ and $4f_{5/2}$ situated at 84.0 and 87.7 eV, respectively.

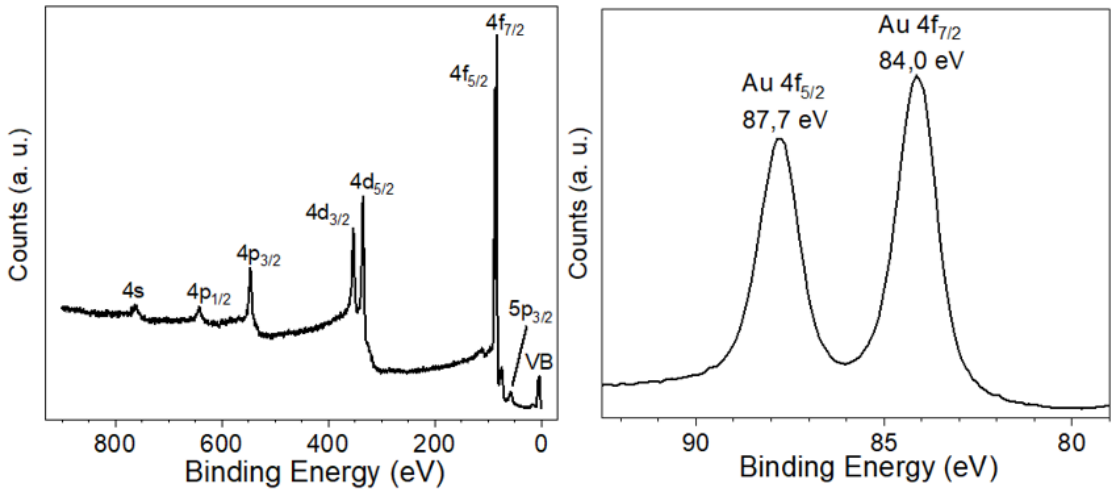

Figure 3-3: Left) XPS survey spectrum of Au; Right) XPS spectrum of Au 4f peaks.

3.1.3 LEED

The LEED pattern of Au (111), in figure 3-4, was acquired using an electron KE of 60 eV, shows the hexagonal reciprocal lattice from which is easily deduced the hexagonal real space lattice. Moreover, focusing on the two reflex at the top-right and at the bottom-right, the common Au(111) herringbone reconstruction with periodicity (22 x √3 of the real lattice) is slightly visible[105]. It must be taken in account that this type of reconstruction is not easily observable by LEED.

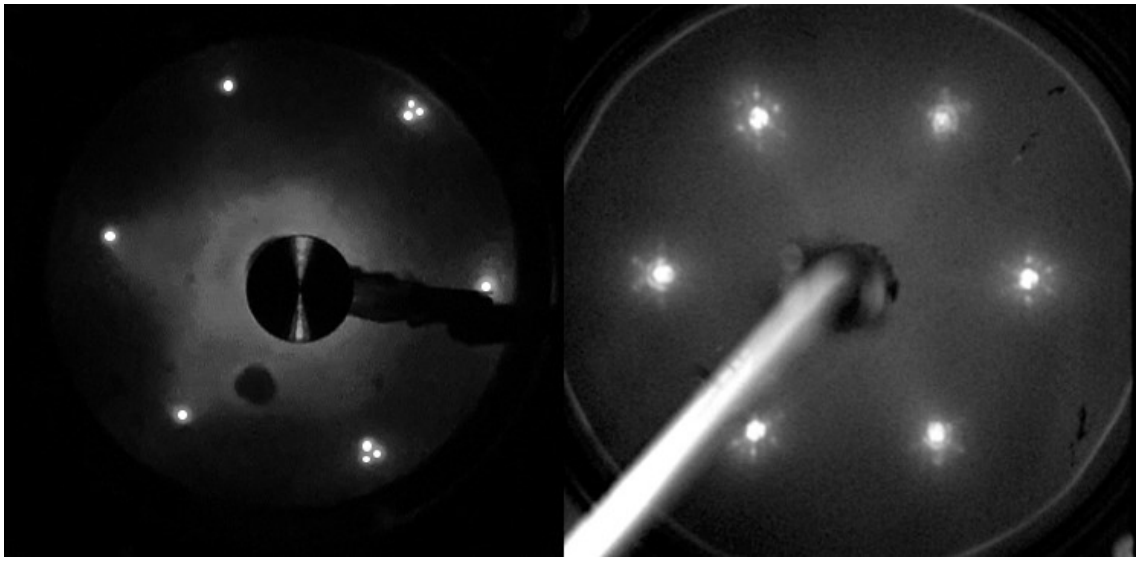

Figure 3-4: Left) measured LEED pattern of clean Au (111), electron energy 60 eV
Right) LEED pattern of clean Au (111), electron energy 60 eV. Reproduced from Ref. 105.

3.1.4 EC-STM

The surface of Au (111) in a KOH 0.1 M solution keeps exhibiting the well-known herringbone reconstruction, as shown on the right in figure 3-5[44]. The image was taken at a 5.89 nA tunnelling current, with the sample positively polarized at 0.32 V with respect to the tip. The sample was polarized at -0.22 V vs RHE (-1.12 V vs Pt) and the current passing through the CE was -5.9 µA.

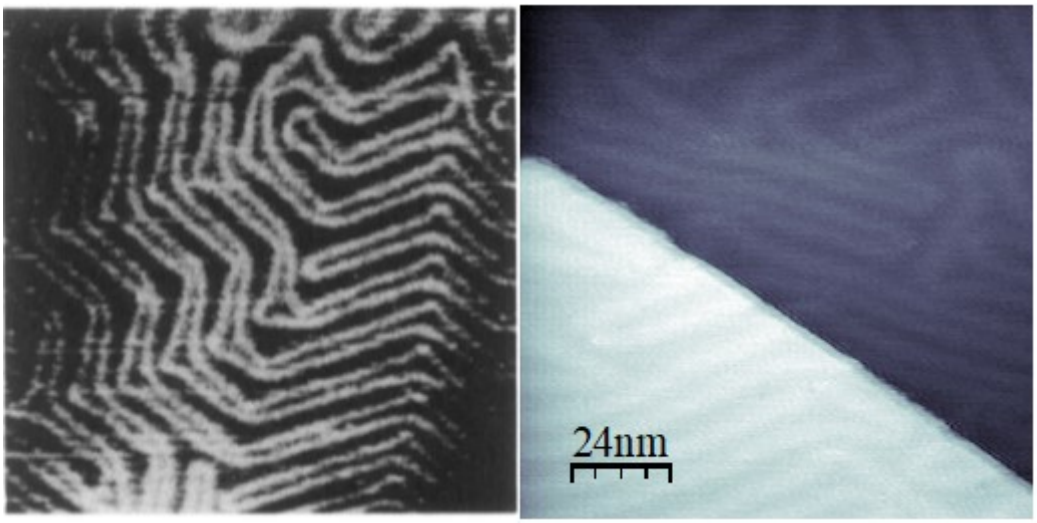

Figure 3-5: Left) 78x78 nm^2 image of the Au(111) surface in UHV. Reproduced from Ref. 44; Right) image of the Au (111) surface in KOH 0.1M. Parameters were I_T = 5.89 nA, U_T = 0.32 V, I_S = -5.9 µA, U_S = -1.12 V

3.2 Comparison between Fe / Au (111) and Fe_3O_4 / Au (111)

Two samples were prepared by depositing in the subMLE regime (20 minutes deposition). One was electrochemically tested without the annealing & oxidation step, the other was annealed for 10 minutes in oxidative atmosphere, dosing molecular Oxygen via a leak valve ($p_{O_2} = 5 \cdot 10^{-7}\ Torr$), at T≈800 K (temperature increasing at 35 K/min, decreasing at 18 K/min).

3.2.1 Electrochemistry

3.2.1.1 Cyclic Voltammetry

The CV seems to not be directly affected by the initial oxidation state of Iron, as shown in figure 3-6; this is probably due to the 0.1 M KOH strong oxidant environment, indeed the Open Circuit Potential (OCP) was always found to be about 0.6-0.7 V vs RHE, indicating a Fe(III) species, as shown in the Pourbaix diagram in figure 3-7[106], regardless

of the initial oxidation state of Iron. From a general perspective, the Pourbaix diagram identifies three regimes of interest for the reactivity of Iron bulk electrodes in aqueous electrolyte, namely the "immunity", the "passivation" and the "corrosion" regime[107]. Within the "immunity" regime (grey), bare Iron is stable against any (electro-)chemical reaction. In the "passivation" regime (green), Iron directly reacts with the electrolyte forming a thin $Fe(OH)_2$ layer on the Iron electrode surface that prevents further reactions of the metal beneath the passive film. Furthermore, the "corrosion" regime (red) is separated in two regions for either acidic (pH < 8.3) or concentrated alkaline solutions (pH > 12). Within these regions, Iron corrodes spontaneously until the corrosion ceases by the eventual formation of a protective layer, which has already been investigated by Michael Faraday and other researchers as early as 1790.[108] It is important to underline the fact that in the nanoscale, Iron may show very different behaviour.

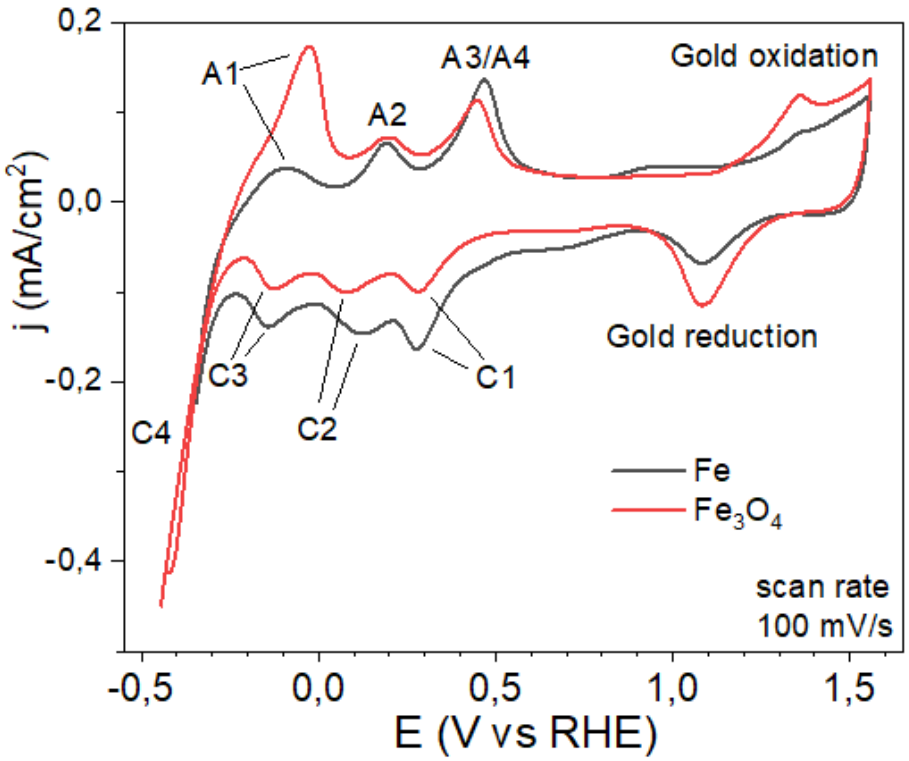

Figure 3-6: comparison between the CV of Fe/Au(111) (black) and Fe_3O_4/Au(111) (red) both in subMLE regime in KOH 0.1 M

Several peaks were recorded: on the right part of the graph are found the oxidation/reduction peaks of Gold, on the left the ones related to Iron: three oxidation

peaks and four reduction ones. The peak A3/A4 was thought to be a convolution of two peaks due to the presence of two the cathodic scan two close reduction peaks, C1 and C2; it was then proved thanks to potential extended CVs, shown in figure 3-8.

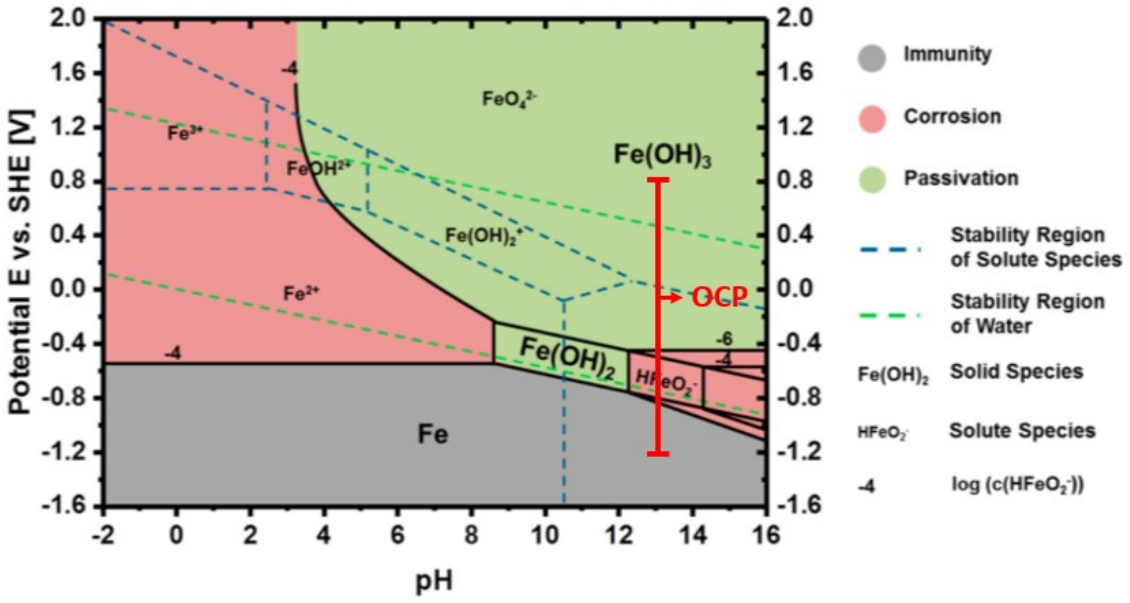

Figure 3-7: Pourbaix diagram of Iron considering $Fe(OH)_2$ and $Fe(OH)_3$ as solid substances only. Adapted from Ref. 106.

Potential extended CVs were taken on the oxidized sample, by keeping constant the Upper Vertex Potential (UVP) at 0.65 V, top-left in figure 3-8, or the Lower Vertex Potential (LVP) at -0.35 V, top-right in figure 3-8; then the LVP was extended to the metallic Iron range, bottom in figure 3-8. Correlation between oxidation and reduction peaks was proved; in particular, in the UVP constant potential extended CV it was noticed that a cathodic overpotential of 0.2 V is required for the C1 peak to appear (light blue line). This may be due to a complex phase change in the reduction from Fe(III) to Fe(II). On the other hand, the oxidation is electrochemically fast and no overpotential are needed, as shown by the good agreement between each restricted CV and the one with the widest range (red line) in figure 3-8 on the right.

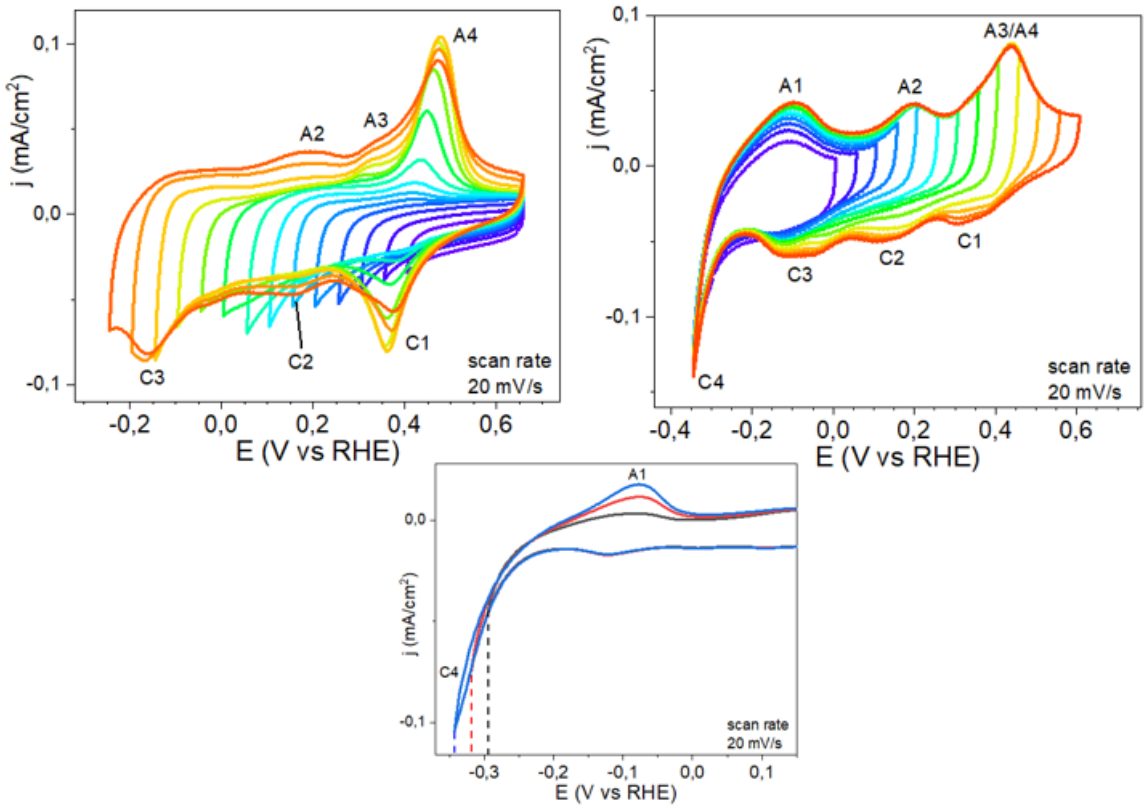

Figure 3-8: potential extended CVs taken at constant UVP (top-left), constant LVP (top-right), extending the LVP in the metallic Iron region (bottom)

According to Micka (6) and Urbaniak (7) the oxidation of metallic Fe may start with the formation of a Fe(I) species (peak A1) and the corresponding reduction peak C4 occurs together with HER. Since according to our investigation A1 is always at negative potential vs RHE, it can be excluded the Hydrogen oxidation reaction (HOR) contribution to the recorded faradaic current. The Fe(I) species may be stabilized to a Fe(I+δ) by the electron withdrawing effect of the Gold substrate on the less electronegative deposited Iron (the Pauling electronegativity of Gold and Iron are 2.54 and 1.83, respectively) It is widely reported in literature[109–113] that, in bulk systems (that may differ from ultra-thin layers), the oxidation to Fe(II) species in alkaline medium occurs *via* the formation of a soluble species, $HFeO_2^-$, that precipitates rapidly as $Fe(OH)_2$. Fe(II) is then further oxidized to Fe (III) in two possible ways, given the presence of the two distinct peaks A3 and A4; one of the two may be related to the oxidation of solid Iron hydroxide $Fe(OH)_2$ to Iron oxo-hydroxide FeOOH and the other may be the oxidation of the solute $HFeO_2^-$ species to FeO_2^-. Possible reactions for each peak are reported in the table 3-1.

Table 3-1: electrodic potential and oxidation reaction for each Iron peak

Peak	Potential (V, metallic Fe)	Potential (V, Fe_3O_4)	Oxidation reaction
A1 (C4)	**-0.10 (-0.35)**	**-0.03 (-0.41)**	**$Fe + OH^- \rightarrow Fe(OH)_{ads} + e^-$**
A2 (C3)	**0.19 (-0.15)**	**0.19 (-0.13)**	**$Fe(OH)_{ads} + 2OH^- \rightarrow HFeO_2^-$ (aq) + $H_2O + e^-$**
			$HFeO_2^-$ (aq) + $H_2O \rightarrow \downarrow Fe(OH)_2$ (s) + OH^-
A3/A4 (C2; C1)	**0.45 (0.12; 0.28)**	**0.44 (0.08; 0.28)**	**$Fe(II) \rightarrow Fe(III) + e^-$**

3.2.2 XPS

As can be observed in the XPS high-resolution spectrum of Fe 2p peak, in figure 3-9 at top-left, the Fe $2p_{3/2}$ peak shifts at higher BE when Iron is oxidized. Besides this, the Fe2p peak area after the oxidation and annealing is reduced of a factor ≈1.67, even though the amount of Iron is the same. This may be due to the fact that at the starting point, the as deposited metallic Iron forms a wetting layer[46] all over the Gold surface, whereas, after the annealing in oxidative atmosphere, Iron oxide NPs grew; thus, the electron photoemitted below the first layers of Oxygen and Iron are attenuated by the top-layer decreasing the overall quantity of Fe 2p signal detected.

The metallic Fe $2p_{3/2}$ peak shape agrees with the one reported by Khan and Matranga[50], with a main peak at 707 eV and satellite shake up at ≈711 eV[114] that results as an asymmetry profile. After oxidation, the obtained Iron oxide phase was the spinel Fe_3O_4, identified by the $2p_{3/2}$ peak position at 710.7 eV, the Fe^{2+} satellite at ≈712eV and the Fe^{3+} satellite ≈720 eV, shifted towards the Fe $2p_{1/2}$ satellite with respect to a Fe_2O_3 samples, according to literature[54,81,115–118].

Moreover, the Au 4f peak is found to be decreased of a factor ≈1.16; hence, even if some Gold surface has been uncovered from Iron, in other regions the thickness of material on Gold increased and so globally the signal decreased, as shown in figure 3-10.

After electrochemistry measurements, so after the exposition of the material to KOH 0.1 M, XPS spectrum of Fe 2p peak did not change significantly, because of the great similarity between the Fe 2p peak of FeOOH (probably the outermost phase) and Fe_3O_4 (under the FeOOH of the surface) phases. On the other hand, O 1s peak broadened since new peaks at higher BE appeared due to the presence of OH and H_2O[119–121], as shown in figure 3-9 at the bottom.

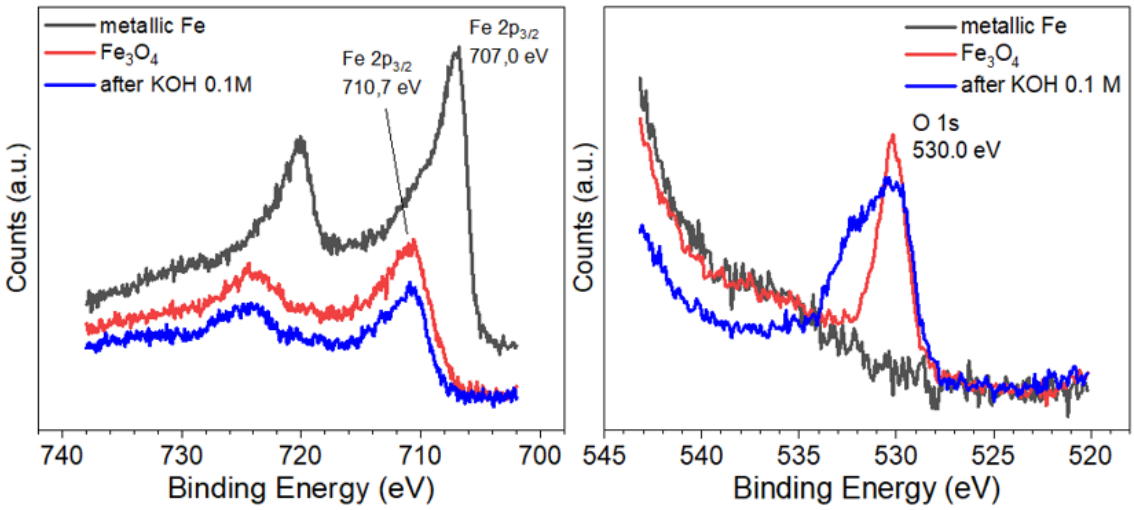

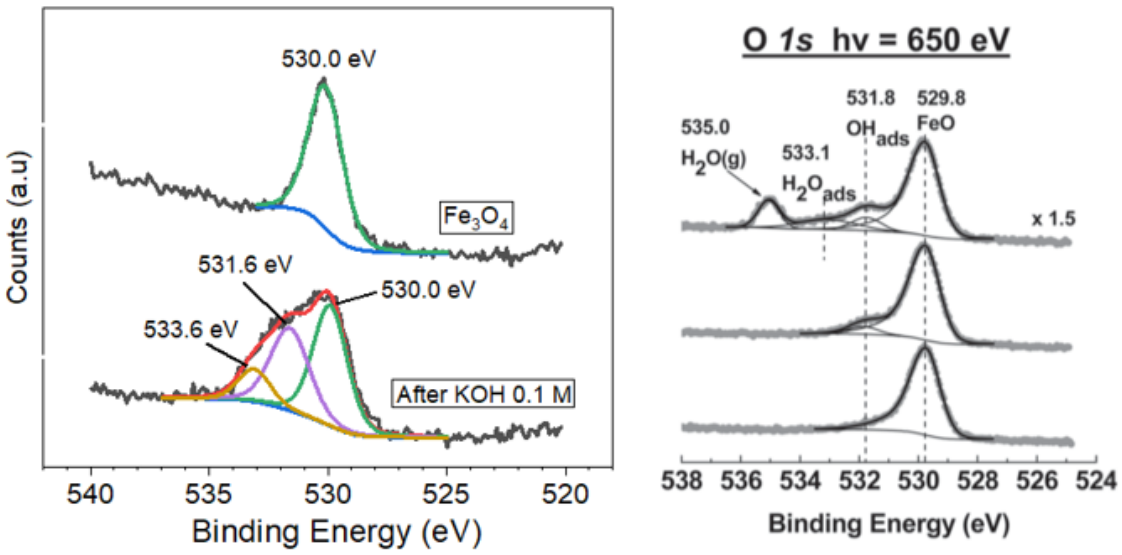

Figure 3-9: comparison between the XPS spectra of Fe 2p peak (top-left) and O 1s peak ((top-right) of metallic Iron (black) and the spinel phase Fe_3O_4 (red) and after electrochemistry measurements (blue). Bottom-left) fit of the O1s peak showing the presence of new peak related to OH and H_2O Oxygen at 531.6 and 533.6 eV, respectively, after electrochemistry. Bottom-right) XPS fit of O 1s peak for hydroxylated FeO. Reproduced from Ref. 119.

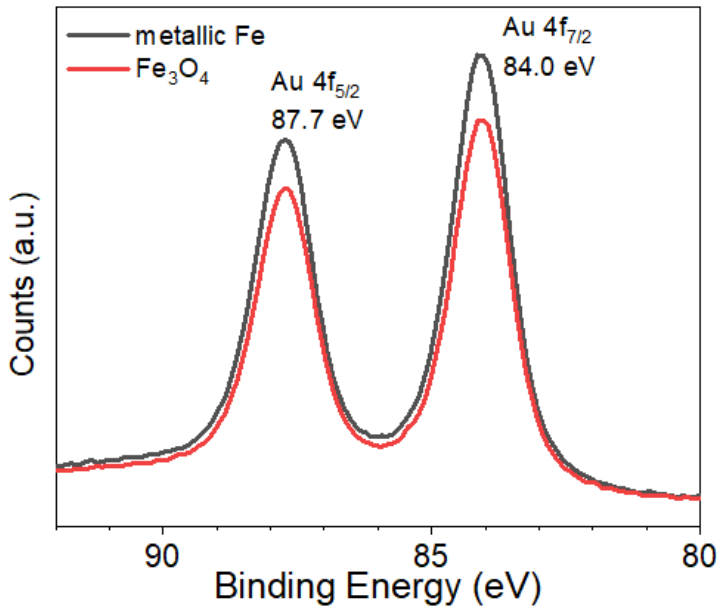

Figure 3-10: comparison between the XPS spectra of Au 4f peak of metallic Iron (black) and of the spinel phase (red)

3.3 Fe_3O_4 / Au (111) submonolayer regime (Θ < 1 MLE)

3.3.1 Electrochemistry

3.3.1.1 Cyclic Voltammetry

During the 10 stabilization cycles (from -0.25 to 1.55 V vs RHE, excluding the metallic Iron range), shown at the top in figure 3-11, no great changes in the CV were observed, only the first cycle (marked with "1") was clearly different. In the complete CV taken at 20 mV/s, shown at the bottom in figure 3-11, A3 and A4 peaks were proved to be distinct peaks. The oxidation from Fe(II) to Fe(III) species may involve two steps or also may follow to different ways. Since the soluble $HFeO_2^-$ species is present in solution, one of the two peaks may involve its oxidation to FeO_2^- and the other the oxidation of solid Iron hydroxide to Iron oxo-hydroxide on the Gold surface.

In the CV taken at 100 mV/s scan rate, reported in figure 3-12, the distinction between the A3-A4 peaks is lost but the C4 peak is more visible.

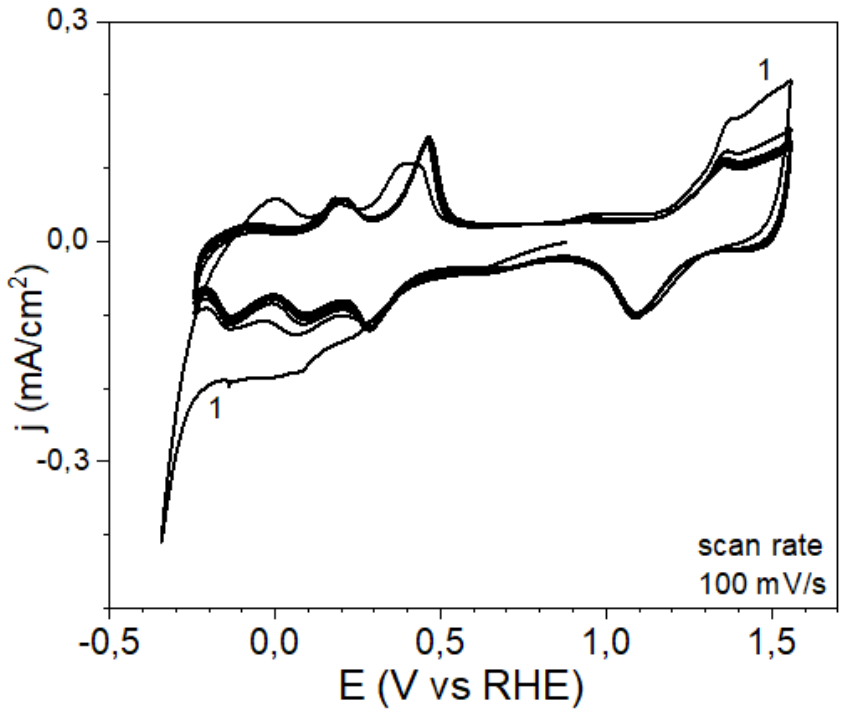

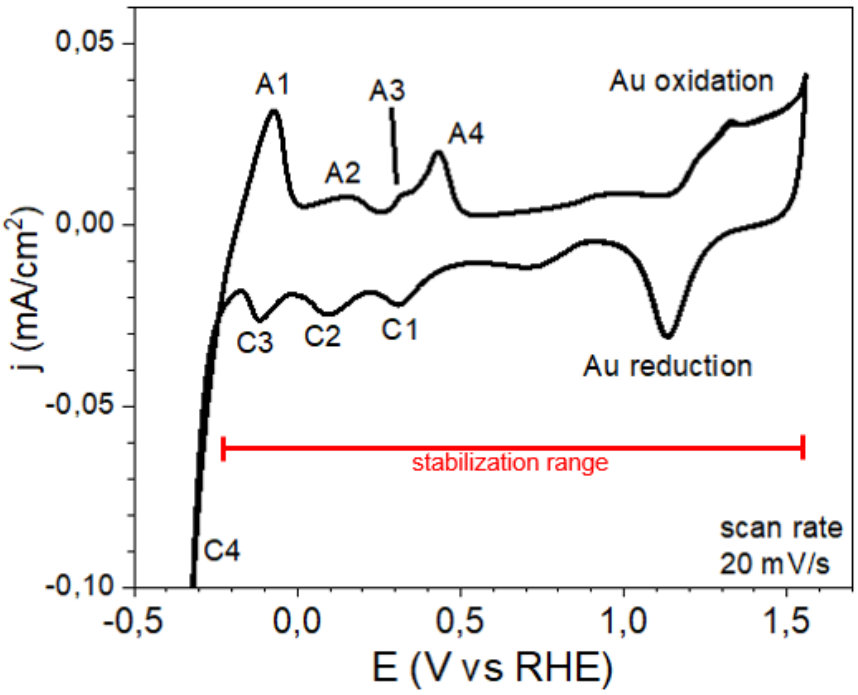

Figure 3-11: Top) 10 cycles stabilization CVs; bottom) CV for Θ < 1MLE at 20 mV/s scan rate.

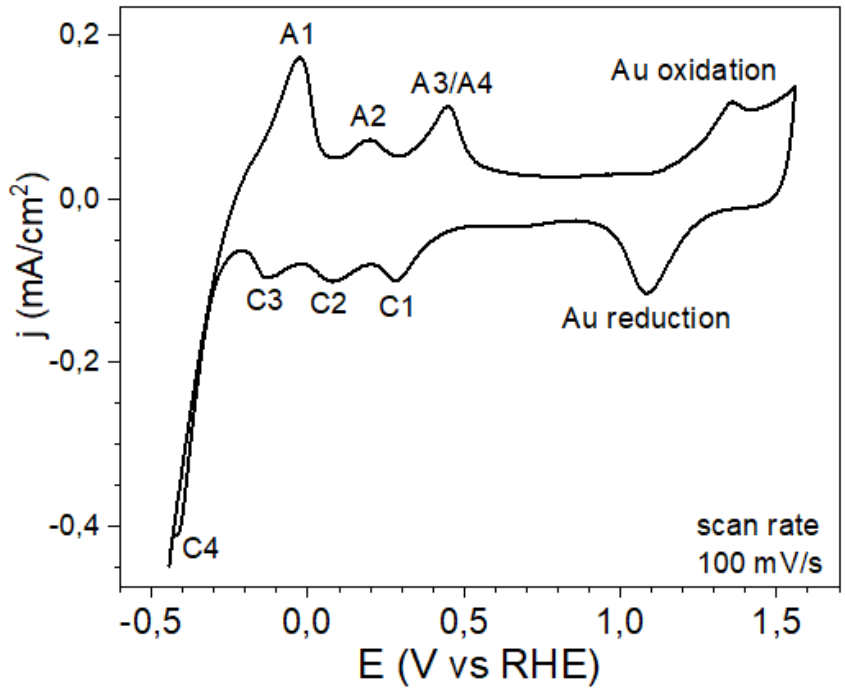

Figure 3-12: CV for Θ < 1 at 100 mV/s scan rate.

Table 3-2: oxidation reaction for each Iron peak

Peak	Potential (V, 20 mV/S)	Potential (V, 100 mV/S)	Oxidation reaction
A1 (C4)	-0.07 (-0.32)	-0.03 (-0.41)	$Fe + OH^- \rightarrow Fe(OH)_{ads} + e^-$
A2 (C3)	0.15 (-0.11)	0.20 (-0.13)	$Fe(OH)_{ads} + 2OH^- \rightarrow HFeO_2^-(aq) + H_2O + e^-$
			$HFeO_2^-(aq) + H_2O \rightarrow \downarrow Fe(OH)_2(s) + OH^-$
A3 (C2)	0.32 (0.09)	(0.08)	$Fe(II) \rightarrow Fe(III) + e^-$ (1st way/step)
A4 (C1)	0.43 (0.31)	0.45 (0.28)	$Fe(II) \rightarrow Fe(III) + e^-$ (2nd way/step)

3.3.1.2 Hydrogen Evolution Reaction - Linear Sweep Voltammetry

In the LSV of the subMLE sample, shown in figure 3-13, an overpotential at 1 mA/cm^2 of -0.54 V is found. The HER onset potential is difficult to be estimated due to overlapping with the reduction peak to metallic Fe situated at -0.37 V. No differences were detected in the subsequent LSVs.

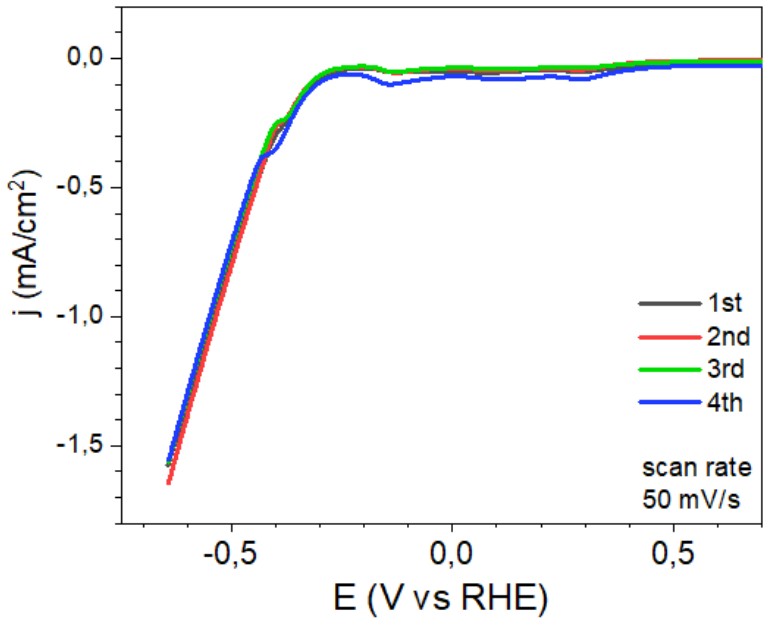

Figure 3-13: consecutive LSVs of the subMLE sample in KOH 0.1 M

3.3.2 XPS

In the XPS survey spectrum of the subMLE sample, shown in figure 3-14 on the left, new peaks related to Iron (Fe 2p and Auger LMM) and Oxygen (O 1s at 530.0 eV) are present. As explained in the paragraph *3.3.2*, the obtained Iron oxide phase is the spinel Fe_3O_4.

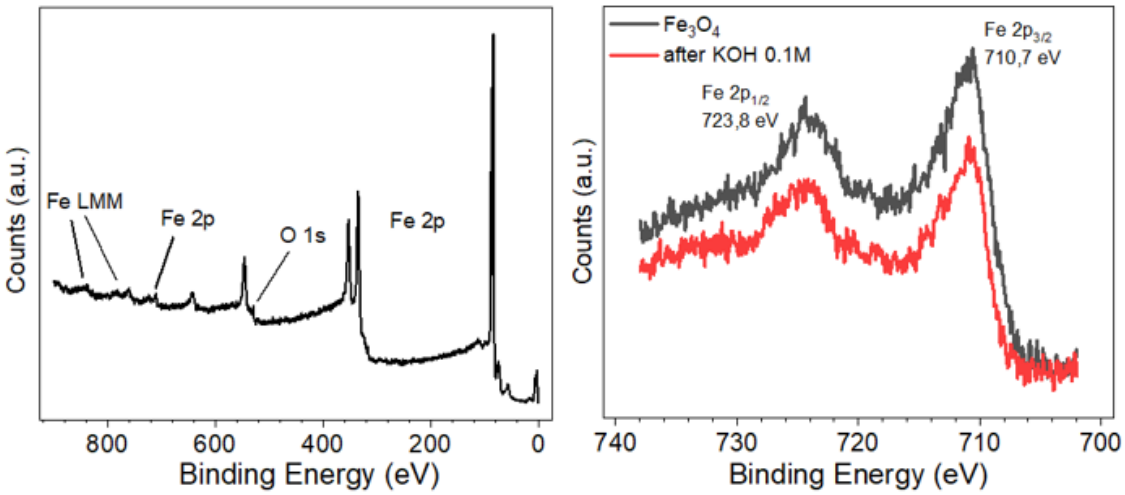

Figure 3-14: Left) XPS survey spectrum of FeOx/Au(111); Right) XPS spectrum of Fe 2p peaks as prepared (black) and after electrochemistry measurements (red)

After electrochemistry measurements, XPS spectrum of Fe 2p peak did not change significantly, whereas a broadening was observed in the O 1s peak; the fit of the O 1s peak is reported in figure 3-9 and described in the paragraph *3.2.2*.

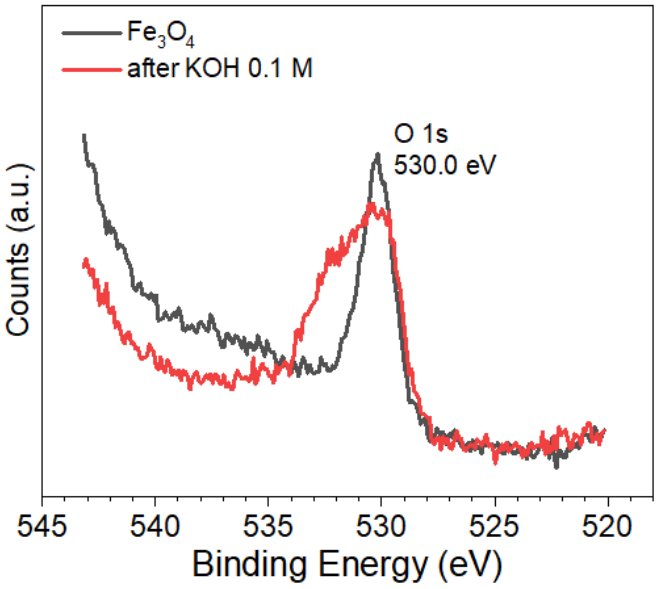

Figure 3-15: XPS spectra of O 1s peak as prepared (black) and after electrochemistry measurements (red)

3.3.3 LEED

The hexagonal LEED pattern, shown in figure 3-16, does not exhibit anymore the Au herringbone pattern, that was already faint also for clean Gold. Moreover, the Fe_3O_4 typical pattern[122] is not detectable probably for the subMLE quantity[58].

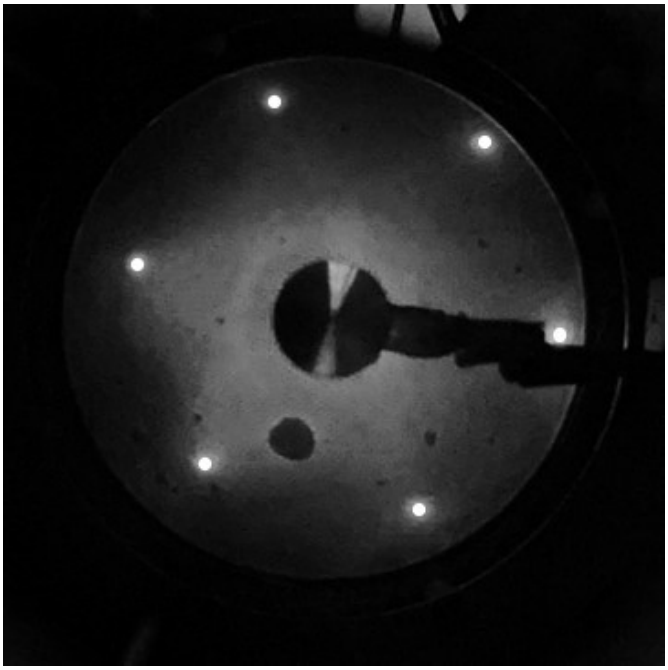

Figure 3-16: LEED pattern of Fe_3O_4 subMLE / Au(111), electron energy 60 eV.

3.3.4 EC-STM

The sample surface was investigated in nitrogen atmosphere (after exposition to air), before and after cycling (10 cycles, from -0.25 V to 1.55 V vs RHE, shown with red bars at the bottom in figure 3-11).

Triangular NPs with a size of tens of nanometres were found, with a height between ≈0.6 nm and ≈12 nm, larger and higher than those reported in literature[50,55]. The thinnest particle has a thickness of about 6 Å, comparable with the one of a 1 MLE of Fe_3O_4[55].

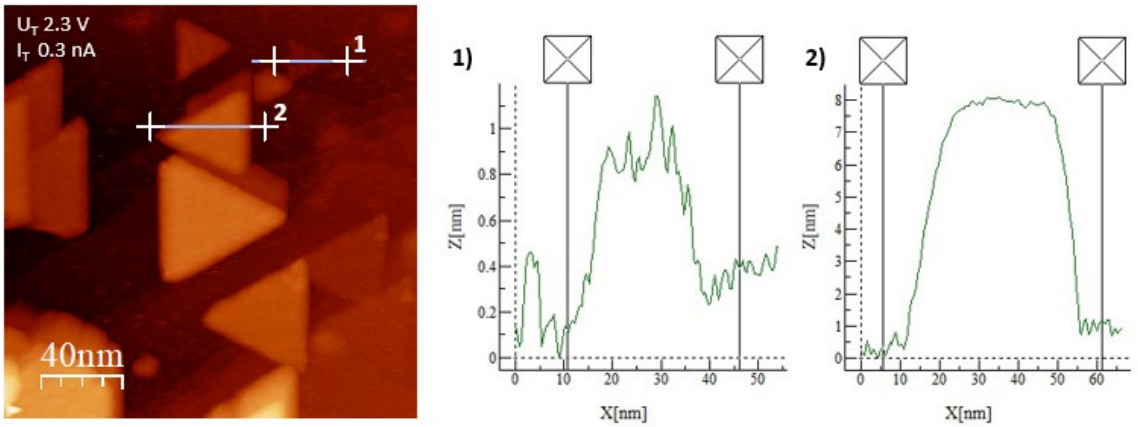

Figure 3-17: STM image of the subMLE sample with height profiles, taken with PtIr tip in air.

In figure 3-18, other images of the NPs are shown, their edge size can range from ≈ 20 - 90 nm.

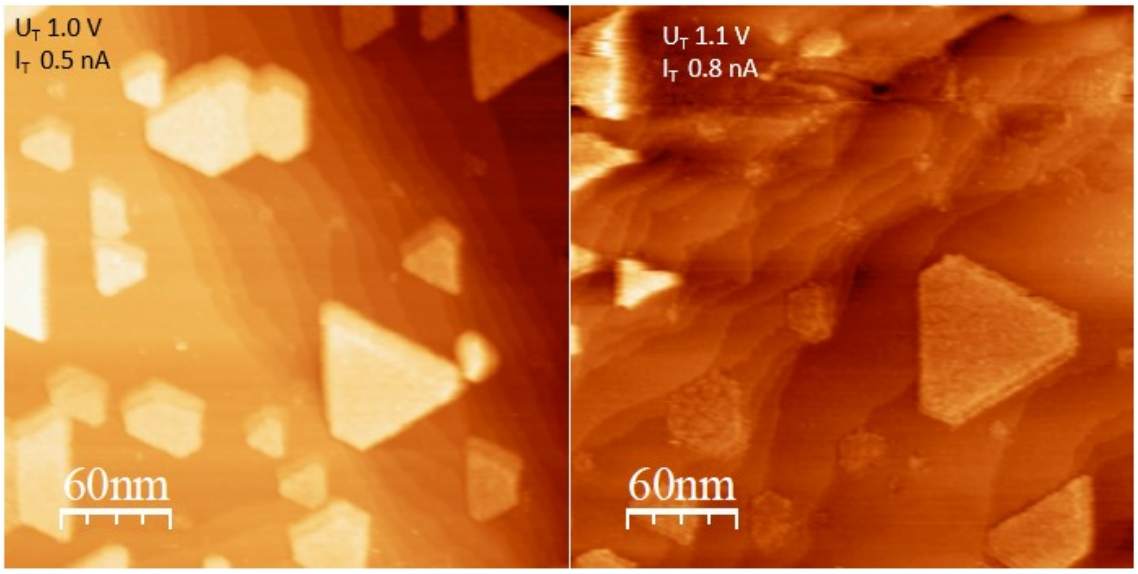

Figure 3-18: triangular NPs found in the subMLE regime. Images were taken with a W tip.

Atomic resolution was found on the top of a NP, as shown in figure 3-19. The lattice constant was calculated to be about 3 Å, coherent with the O-O distance in a Fe_3O_4 (111) surface (being the Fe-Fe distance 5.92 Å). This further confirmed the previous determination of the Fe_3O_4 spinel phase, that is found to not undergoing any phase change after short air exposure.

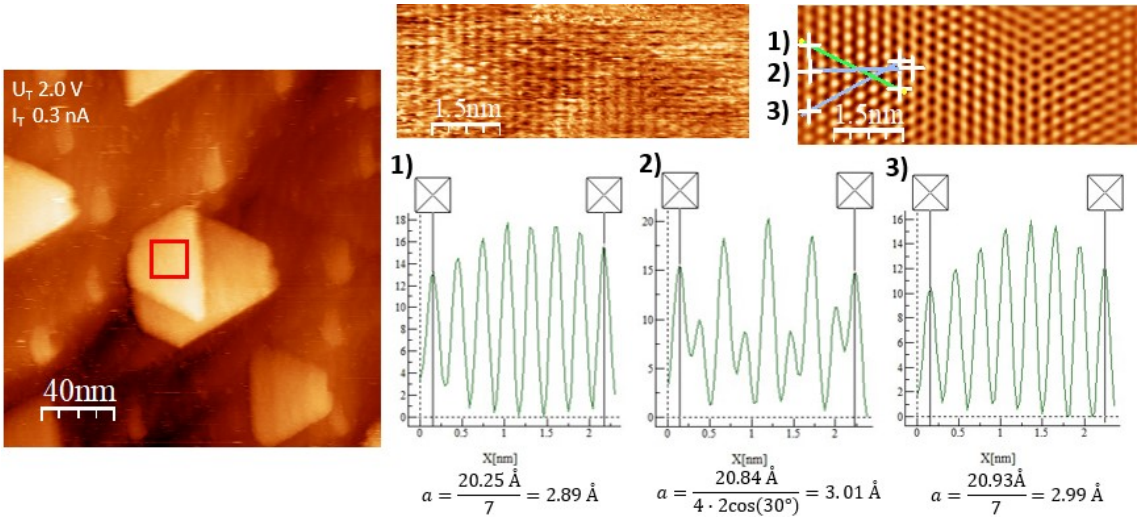

Figure 3-19: atomic resolution found on a Fe_3O_4 NP.

After 10 reorganization cycles between -0.25 and 1.55 V vs RHE (excluding the metallic Iron potential range) the triangular NPs were completely lost and, in some regions, triangular "footprints" were found scanning in KOH 0.1M, while polarizing at -0.1 V vs RHE, with dimensions comparable with the one of the previous NPs, as shown in figure 3-20 on the left. This may be explained by the fact that the deposition step of the dissolution-deposition process occurs faster on the Gold surface rather than on the Iron oxide NPs leading to the triangular footprints. In other regions a very rough surface was found (roughness ≈0.7 nm, maximum height 6.0 nm) as shown in figure 3-20 on the right; also the Gold surface was found to be rough, since its oxidation and subsequent reduction (so inclusion of Oxygen in the structure followed by its expulsion) worsened the outermost atomic layers, and this made difficult to distinguish between Gold and Iron in EC-STM measurements. The particles have diameters that range from 12 to 17 nm with an average of 14.5 nm, the apparent heights range from 1.9 to 3.5 nm with an average of 2.36 nm.

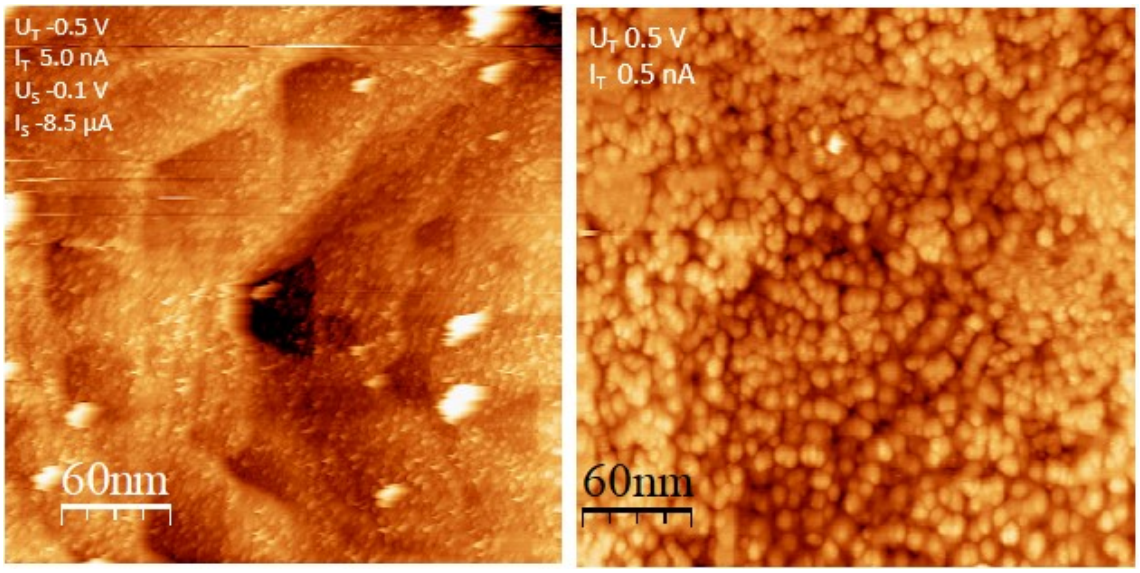

Figure 3-20: surface after cycling 10 times between -0.25 V and 1.55 V vs RHE. Left) in KOH 0.1 M; Right) in air.

EC-STM measurements provided a unique opportunity to visualize the high mobility of Iron on the Gold surface, a phenomenon not apparent with traditional macroscopic EC techniques. While the stabilization CV in Figure 3-11 at the top did not exhibit significant changes, EC-STM images revealed dramatic alterations in the surface structure.

3.4 Fe_3O_4 / Au (111) high coverage regime (Θ > 5 MLE)

To investigate the catalytic activity depending on the amount of Iron deposited, a sample with ≈10 times Iron quantity was prepared (200 minutes deposition followed by annealing for 30 minutes in oxidative atmosphere, dosing molecular Oxygen *via* a leak valve ($p_{O_2} = 5 \cdot 10^{-7}\ Torr$), at T≈800 K (temperature ramp at 35 K/min for both increasing and decreasing T).

3.4.1 Electrochemistry

3.4.1.1 Cyclic Voltammetry before HER

In the case of Fe multilayer, during the 10 reorganization cycles (between -0.25 and 1.55 V vs RHE, excluding the metallic Iron potential range, shown at the top in figure 3-21), great changes were found. Gold peaks were detectable at the beginning and faded during cycling, on the other hand Iron peaks were increasing. This means that at the

starting point the Gold surface was exposed between the relative high (given the large amount of Iron deposited) spinel particles, then the Gold surface was covered cycle by cycle due to the electrochemical dissolution of $Fe(OH)_{ads}$ to $HFeO_2^-$ and subsequent precipitation as $Fe(OH)_2$, as sketched at the bottom in figure 3-21. Besides the EC-STM evidence shown even in the subMLE regime in figure 3-20, this constitutes another strong proof of the great mobility of Iron oxide layers, even though excluding the metallic Iron potential range, in which significant structural changes surely occur due to complete expulsion of Oxygen from the crystalline lattice explained in the paragraph *3.5.1.1*.

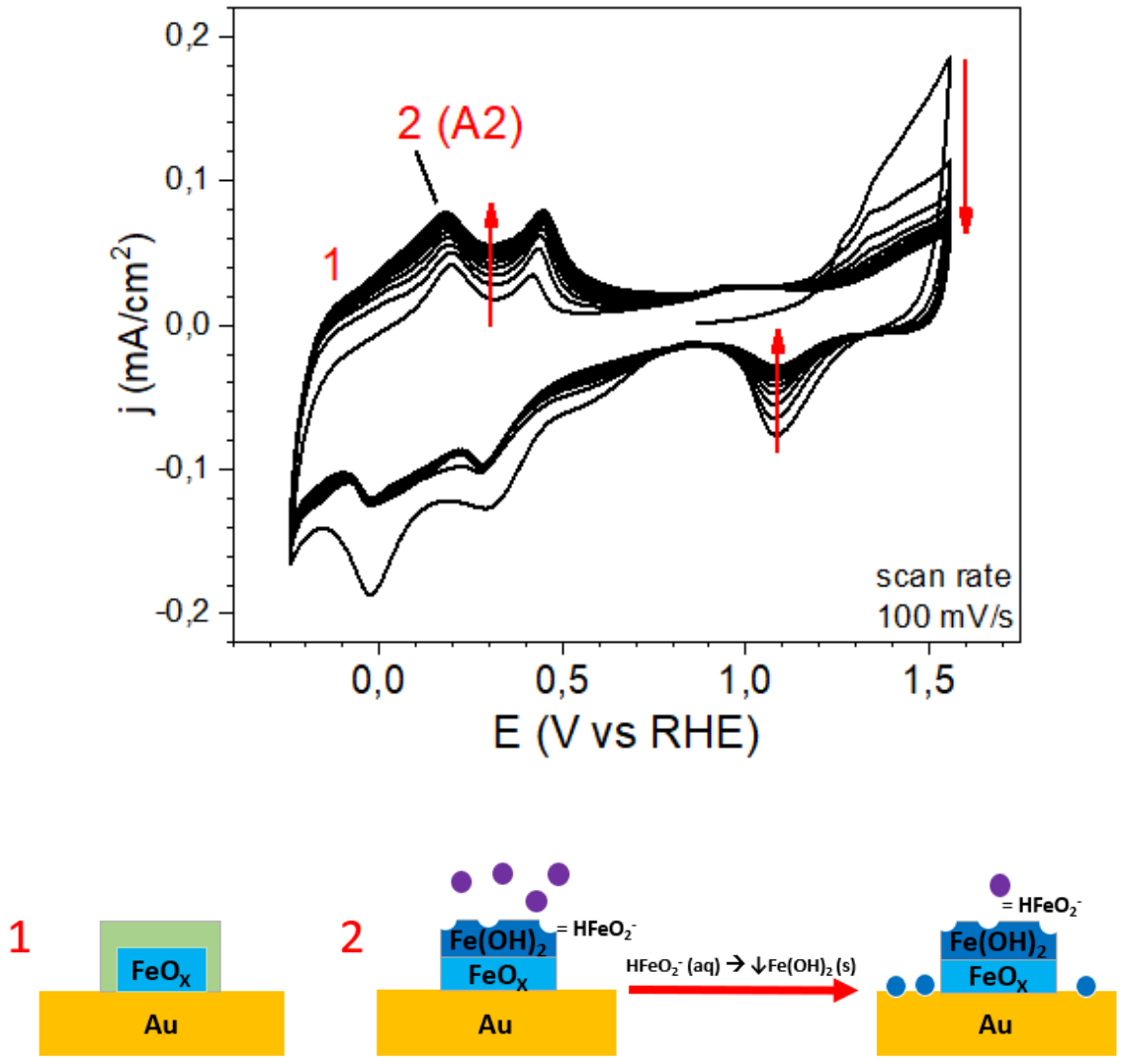

Figure 3-21: top) stabilization CVs, 10 cycles at a scan rate of 100 mV/s; bottom) scheme representing the dissolution-deposition process.

The CV taken at 20 mV/s after having stabilized the sample showed very strong similarities with the subMLE one, as illustrated in figure 3-22, exhibiting the same peaks with small difference in intensity ratio and applied voltage: peaks A2, C2 and C3 moved cathodically of 0.04, 0.06 and 0.03 V, respectively. This may be explained by little local variations of the pH between the two samples, or it may be due to an easier reduction of the Iron in the subMLE regime, where the electronic effects of Gold are much more intense on the Iron oxide layers than in the high coverage regime. The bulk Gold substrate may help the reduction of Iron thanks to the stabilization at partially higher oxidation numbers more stable species (Fe(I) → Fe(I+δ) and Fe(II) → Fe(II+δ)), given its higher electronegativity with respect to Iron (2.54 and 1.83, respectively). On the other hand, the oxidation from Fe(I) to Fe(II) seems to be a bit more difficult in the subMLE regime (since it shifted anodically); this may be due to the higher compactness of the film than in the high coverage regime and so a greater effort for the two hydroxyde ions to reach and react with the Iron, according to the reaction of A2 peak in table 3-2.

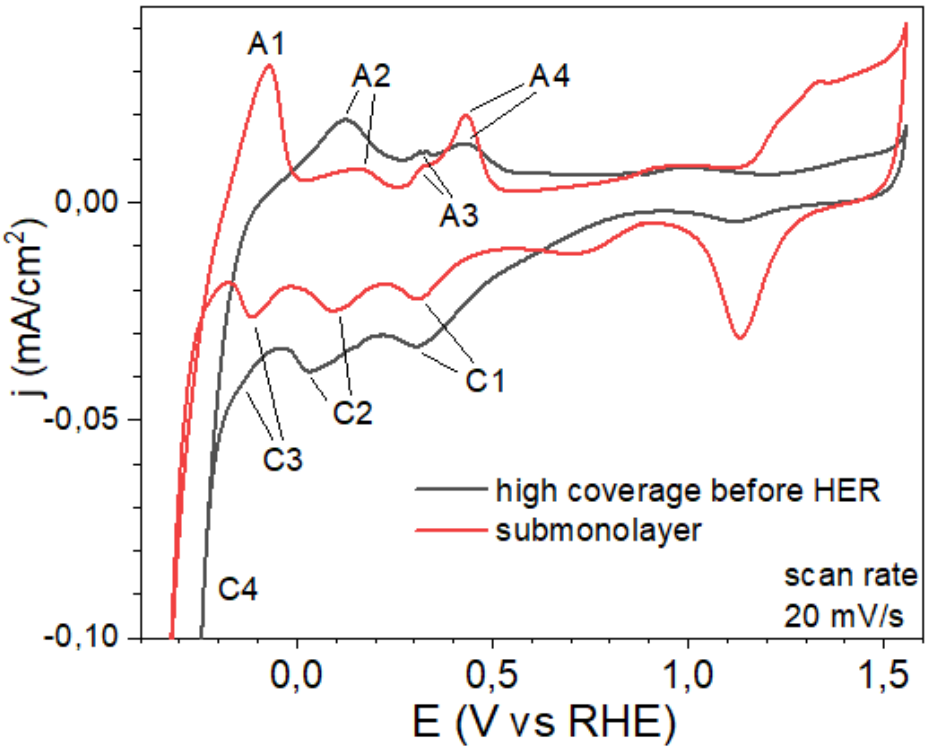

Figure 3-22: CV of high coverage sample compared with the subMLE one, both taken at 20 mV/s.

3.4.1.2 Hydrogen Evolution Reaction - Linear Sweep Voltammetry

The first LSV taken showed an overpotential at 1 mA/cm^2 of -0.49 V. The CV after LSV changed a lot (see figure 3-24), so a second LSV was taken; it was found out a very different activity between the two LSV in contrast to the subMLE regime reported in figure 3-13 which shows consistent LSVs.

In the second LSV In figure 3-23, it is possible to clearly identify two reduction peaks (the metallic Fe one at -0.4 V and the one at -0.12 V probably related to the reduction from Fe(III) to Fe(II)), the overpotential at 1 mA/cm^2 was found to be worsen at -0.57 V; thus, the sample was much more active toward HER at the first LSV, then the performance of the material worsened. The reason of this may be found in the growth of an outer porous layer (described in the paragraph *3.5.1.1*), which traps the produced gaseous hydrogen "poisoning" the catalyst and ending in reducing of around 24% the density current (proportional to the moles of hydrogen produced per unit time per unit area) at an overpotential of 0.6 V vs RHE.

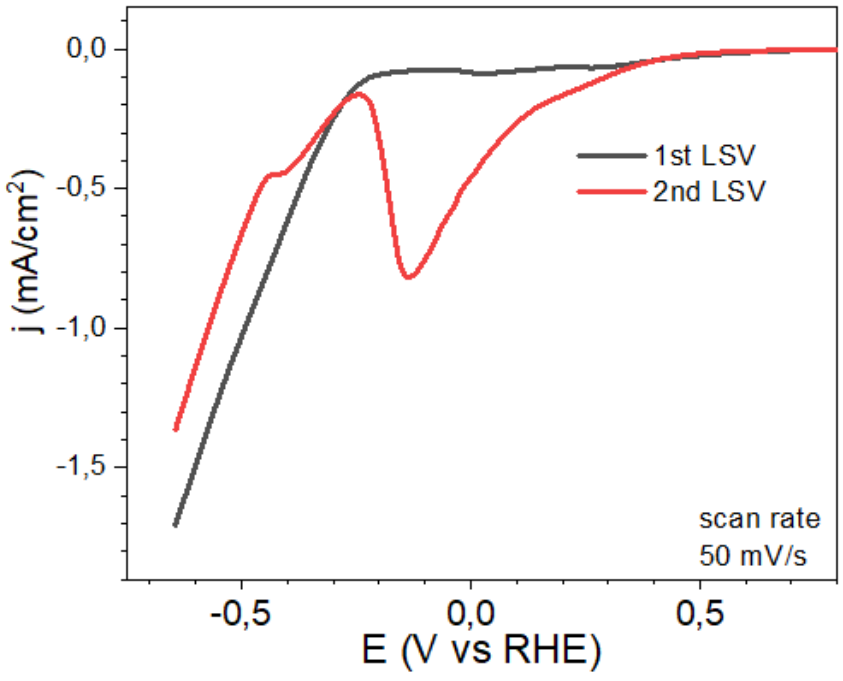

Figure 3-23: comparison between the first (black) and second (red) LSV taken on the high coverage sample.

3.4.1.3 *Cyclic Voltammetry after HER*

The CV of the sample changed dramatically after the LSV toward HER, as can be seen in figure 3-24. The peak related to oxidation from Fe (II) to Fe (III) (A3/A4) and the one related to the corresponding reduction (C2/C3) grew a lot; the A2 and C1 peaks remained slightly recognizable. Hence, the Fe(II)-Fe(III) peak depends on the amount of Iron deposited and after HER the structure pass from a compact structure, in which only the outermost layer is electrochemically involved, to a porous high electrochemical surface area one, giving a CV analogous to the one of bulk Iron[123–127], shown in figure 3-31.

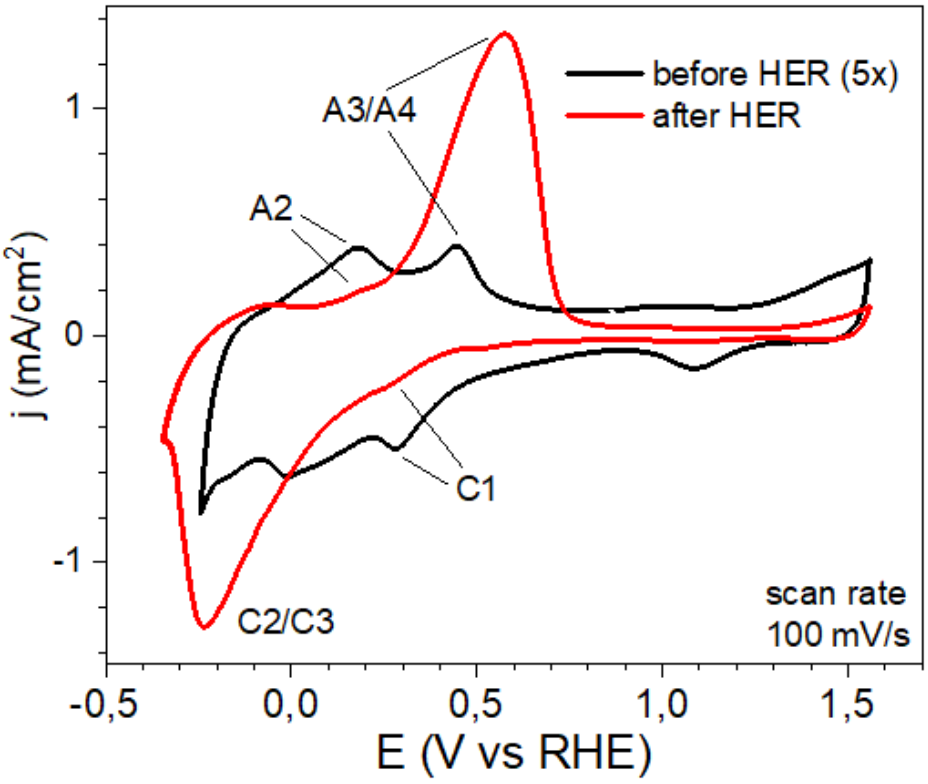

Figure 3-24: CV taken at 100 mV/s scan rate of the high coverage sample before (black) and after (red) the LSV in HER region.

3.4.2 XPS

In the XPS survey spectrum, showed in figure 3-25 on the left, peaks of Oxygen (O 1s at 530.0 eV) and Iron (Fe2p and Auger LMM) are easily identifiable, given the high amount of Iron oxide deposited. The high-resolution spectrum of Fe 2p peak, in figure 3-25 on the right, agrees with a spinel phase, Fe_3O_4, as explained in the paragraph *3.3.2*.

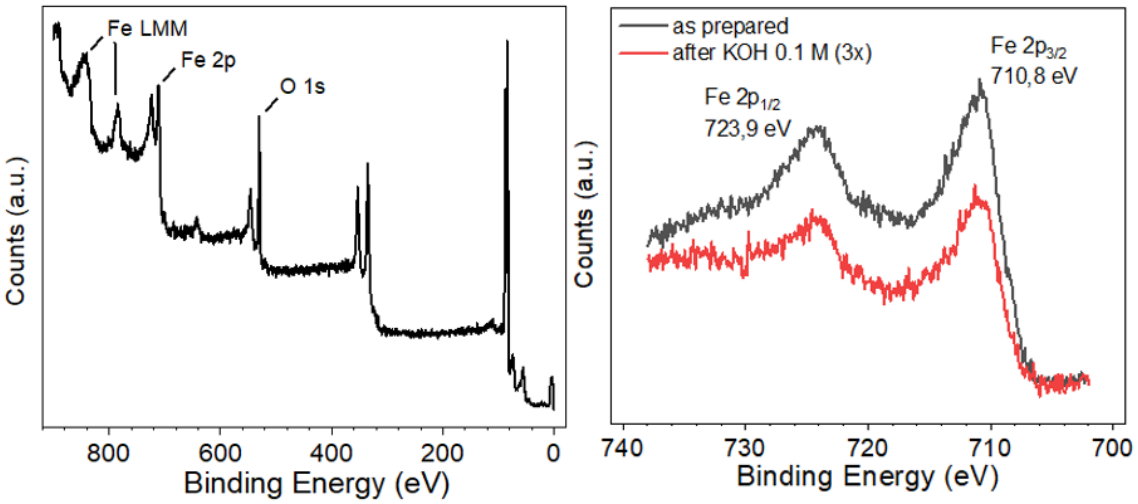

Figure 3-25: Left) XPS survey spectrum of Fe_3O_4/Au(111); Right) XPS spectrum of Fe 2p peaks as prepared (black) and after electrochemistry measurements (red)

As described in the paragraph *3.3.2*, after electrochemistry measurements, so after the exposition of the material to KOH 0.1 M, XPS spectra of Fe 2p peak did not change significantly for the similarity of Fe 2p of spinel and FeOOH, whereas O 1s peak broadened and shifted. In this case. as shown in figure 3-26 at the bottom, the main component is the one of the OH group. This is due to the thick outer hydrous layer formed after the LSV in HER containing many OH groups.

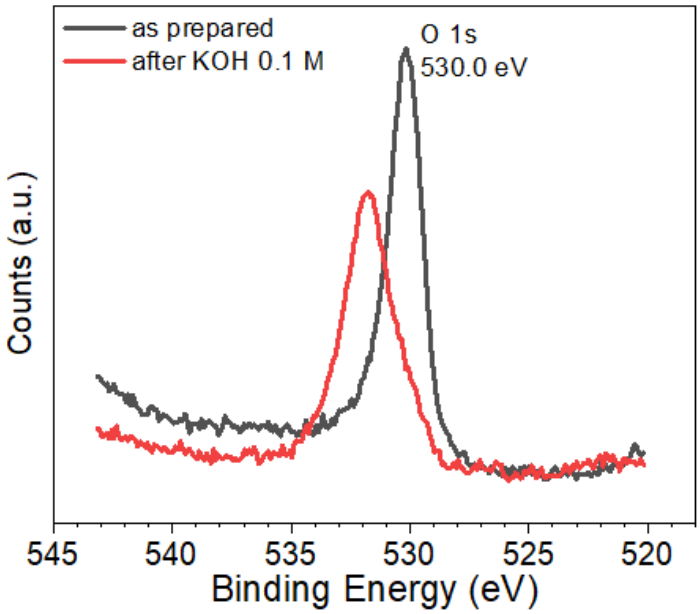

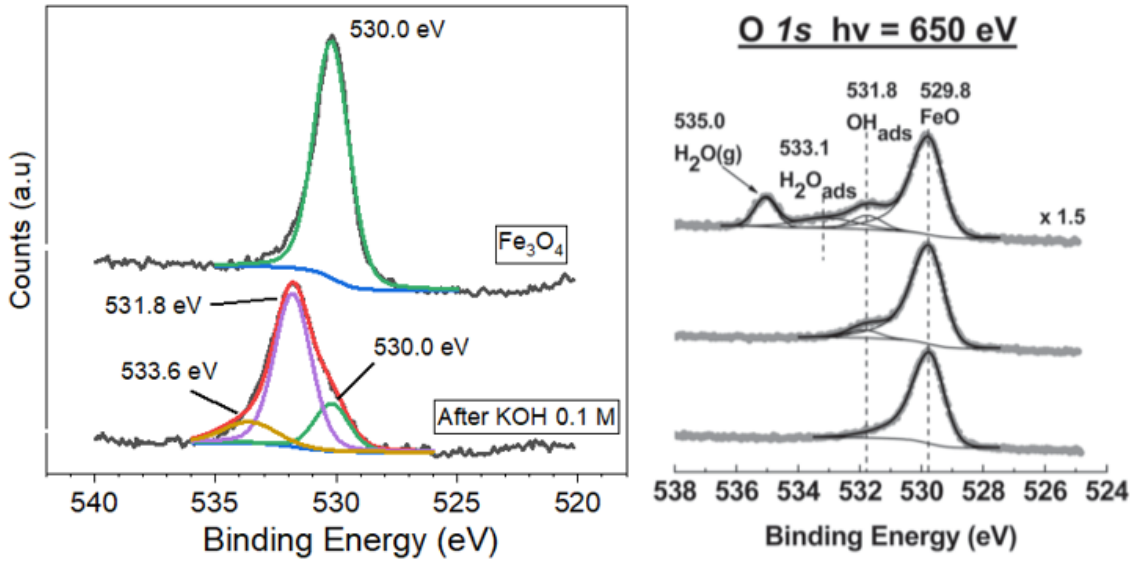

Figure 3-26: Top) XPS spectra of O 1s peak as prepared (black) and after electrochemistry measurements (red) Bottom-left) fit of the O1s peak showing the presence of new peak related to OH and H_2O Oxygen at 531.8 and 533.6 eV, respectively, after electrochemistry. Bottom-right) XPS fit of O 1s peak for hydroxylated FeO. Reproduced from Ref. 119.

3.4.3 LEED

As shown in figure 3-27[122], the LEED pattern exhibited a clear (2 x 2) superstructure on Au (111), confirming the spinel phase and revealing the epitaxial pseudomorphic growth on Au(111), since the spots of the second order of diffraction of Fe_3O_4 coincide with the first order ones of Au (111). Being the lattice constant of Au(111) 2.89 Å and the one of the Fe_3O_4 (111) Fe_{tet1} terminated surface 5.92 Å, the mismatch was calculated to be ≈2.4%.[61]

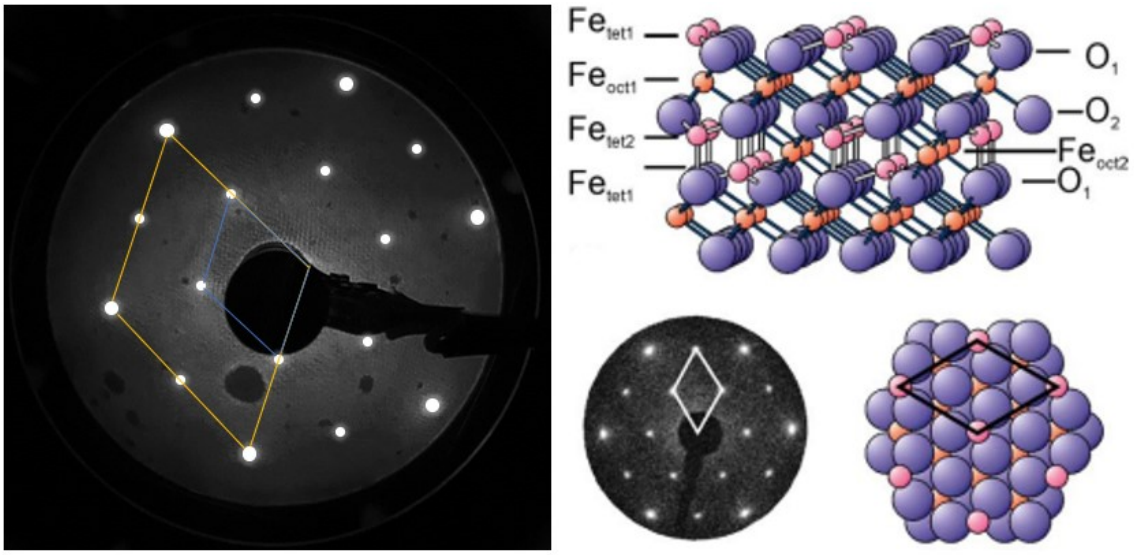

Figure 3-27: Left) measured LEED pattern; Right) at the top, structure of Fe_3O_4, at the bottom LEED pattern and structure of the Fe_3O_4 (111) Fe_{tet1} terminated surface. Reproduced from Ref. 122.

3.4.4 Raman

The sample as prepared was investigated by means of Raman spectroscopy (laser wavelength 523 nm, 1 mW, long working distance 50x objective) the spectrum is shown in figure 3-28. The main bands recognizable at 537 and 667 cm^{-1} reveal a magnetite phase[128].

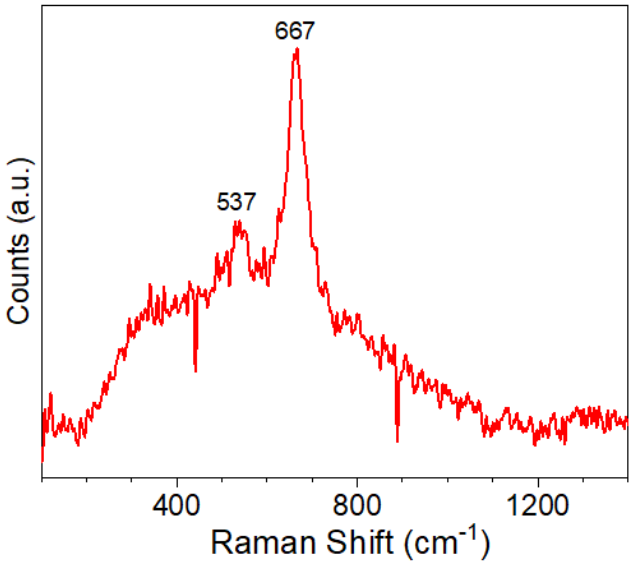

Figure 3-28: Raman spectrum of the high coverage sample.

3.4.5 EC-STM

Given the (relatively) significant thickness of the semiconductive Iron oxide film, that hinders the electrons to tunnel from the sample to the tip (and viceversa), EC-STM images were particularly difficult to be measured. However, some dissolution phenomena were recorded at OCP. A bridge-like region was observed while dissolving. The four images reported in figure 3-29 were taken in a time of 7 minutes; the "bridge" became thinner (large 73, 40 and 14 nm from left to right), until disappearing (last image on the right). The stable phase at 0.8 V vs RHE (-0.1 V vs Pt) is FeOOH (+ H_2O → $Fe(OH)_3$), the dissolution driving force may be the reduction of the surface energy by reducing the density of edges. The line profiles shown at the bottom in figure 3-29 prove that the "bridge" kept a constant height of 5-6 Å in the process.

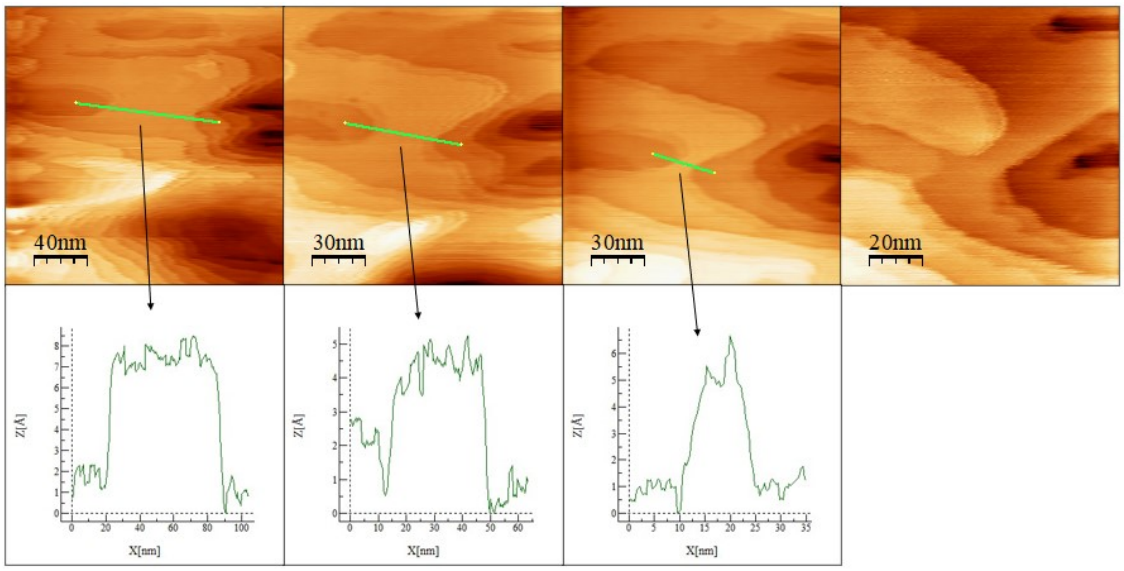

Figure 3-29: EC-STM images taken with a W coated tip in KOH 0.1 M at OCP ($I_S \approx 0$ µA, $U_S = 0.8$ V vs RHE), $U_T = 0.415$ V, $I_T = 0.777$ nA.

The high mobility of the species makes almost impossible to focus the measurements changing the EC potential.

3.5 Fe_3O_4 / Au (111) multilayer regime (Θ ≈ 1.5 MLE)

After having observed the behaviour of the high coverage sample, with the growth of an important peak after having reduced the Iron to zero oxidation state, a lower coverage sample was prepared to investigate the critical thickness above which it was possible to observe the new peak and to eventually try to control its growth.

3.5.1 Electrochemistry

3.5.1.1 Cyclic Voltammetry

During the 10 reorganization cycles, shown in figure 3-30, great changes were found as for the high coverage sample. Gold peaks were present at the beginning and faded during cycling, Iron peaks were increasing in the meanwhile. The Gold surface cycle by cycle is covered by Iron oxide due to the electrochemical dissolution of $Fe(OH)_{ads}$ to $HFeO_2^-$ and subsequent precipitation as $Fe(OH)_2$, as illustrated in figure 3-21.

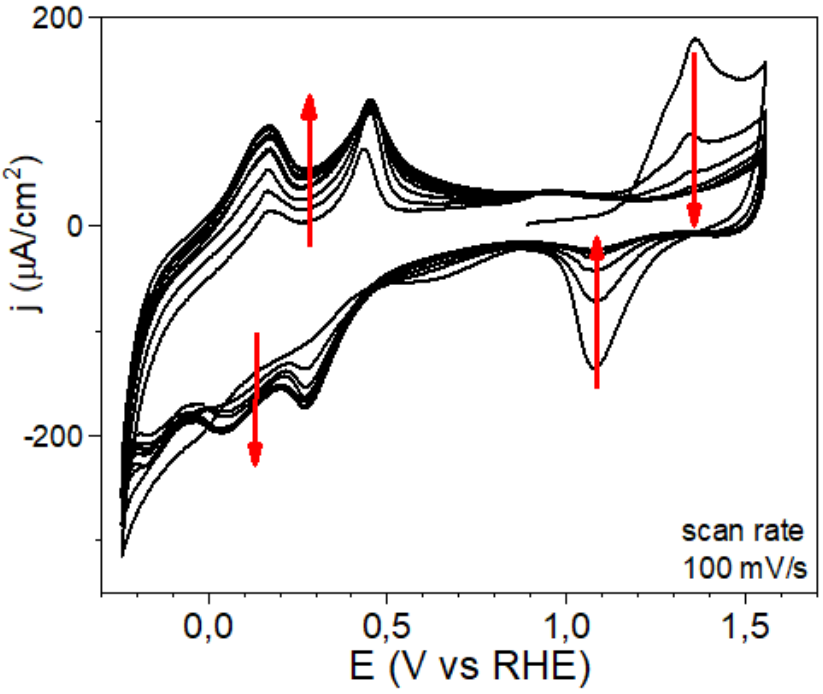

Figure 3-30: stabilization CVs, 10 cycles at a scan rate of 100 mV/s

While in the high coverage regime the growth of the A3 peak was observed all at once after the LSV toward HER, in this coverage regime, just by extending the potential range to the region of metallic Fe (not reached during the 10 cycles stabilization), it was possible to control the growth of the A3 and C2 peaks, whereas other peaks kept

constant, as shown in figure 3-31 on the left. Thus, the complete expulsion of O from the lattice, lets an outer porous structure, namely outer layer (figure 3-32), which thickness increases at each cycle, probably favoured by the dissolution-deposition process described above. This phenomenon was observed by Lyons and Brandon, shown in figure 3-31 on the right, in their study on a polycrystalline Iron electrode[129] and also by Duschek et al.[123] on a 10 nm thick Iron film on Pt. Albani et al.[124], by correlation between electrochemical and ellipsometry studies, proved the existence of an inner "compact" layer difficult to electroreduce, which the authors hypothesized made of Fe_3O_4, and an outer gelatinous Iron hydroxide layer.

Because of the absence of the outer layer fingerprint in the CV for subMLE, we related the EC-STM results, in paragraph *3.3.4*, to the redeposition of compact Iron NPs, i.e. NPs that have an ordered structure but with smaller nanometric size.

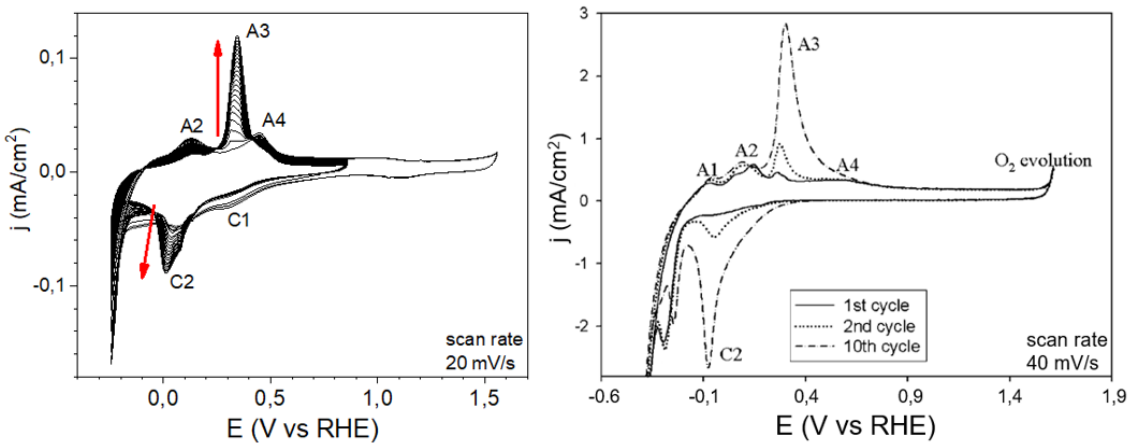

Figure 3-31: Left) CV showing the growth of the A3 peak; Right) CV taken at 40 mV/s of a polycrystalline Iron electrode in KOH 0.1M. Adapted from Ref. 129

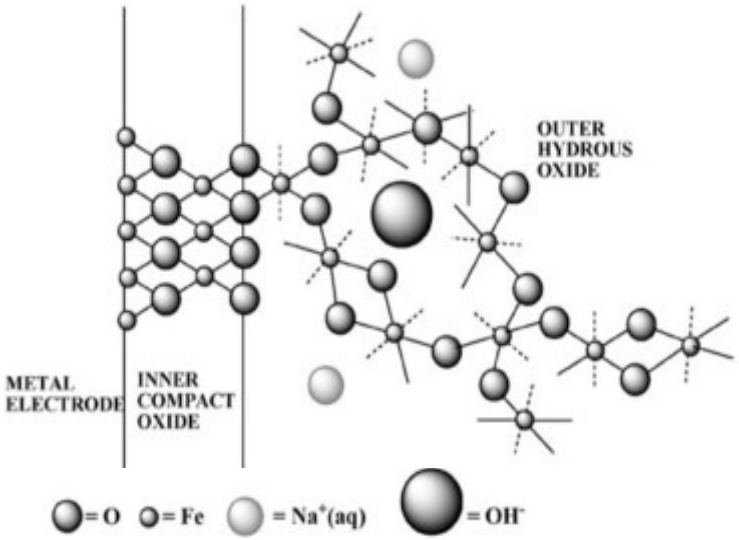

Figure 3-32: Schematic representation of the Fe/FeO_x/$FeO_a(OH)_b(OH_2)_c$/electrolyte interface region. Reproduced from Ref. 129.

The CV including the C4 and A1 peak is shown in figure 3-33. The A4 peak remains unknown, but can be excluded its relationship to a second step in the oxidation Fe(II) → Fe(III), indeed, it can be connected to the oxidation of the inner compact layer or of the $HFeO_2^-$ soluble species, to get more information about A4 see next paragraph. The resolution among C1, C2 and C3 peaks is lost, as the one among A3 and A4 peaks.

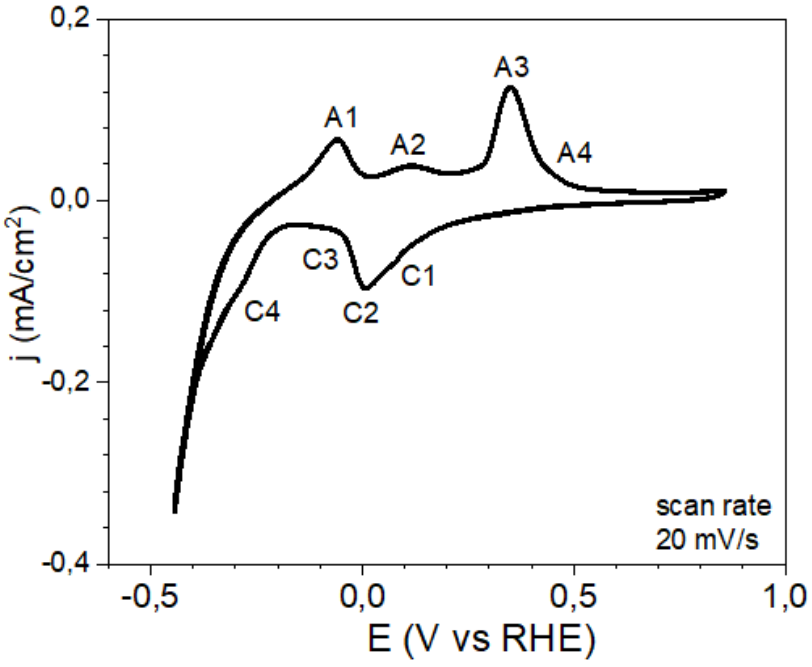

Figure 3-33: CV taken at 20 mV/s of the multilayer sample in KOH 0.1 M

Potential extended CVs were taken by keeping constant the UVP at 0.75 V, top-left in figure 3-34, or the LVP at -0.25 V, top-right in figure 3-34. Correlation between oxidation and reduction peaks was proved; in particular, in the UVP constant potential extended CV it was noticed that a cathodic overpotential of 0.3 V was required for the C1 peak to appear, as highlighted in the zoom at the bottom in figure 3-34 (lime coloured line). This may be due to a complex phase change in the reduction from Fe(III) to Fe(II).

On the other hand, the oxidation is electrochemically fast and no overpotential are needed, as shown by the good in figure 3-34 at top-right agreement between each restricted CV and the largest one (red line).

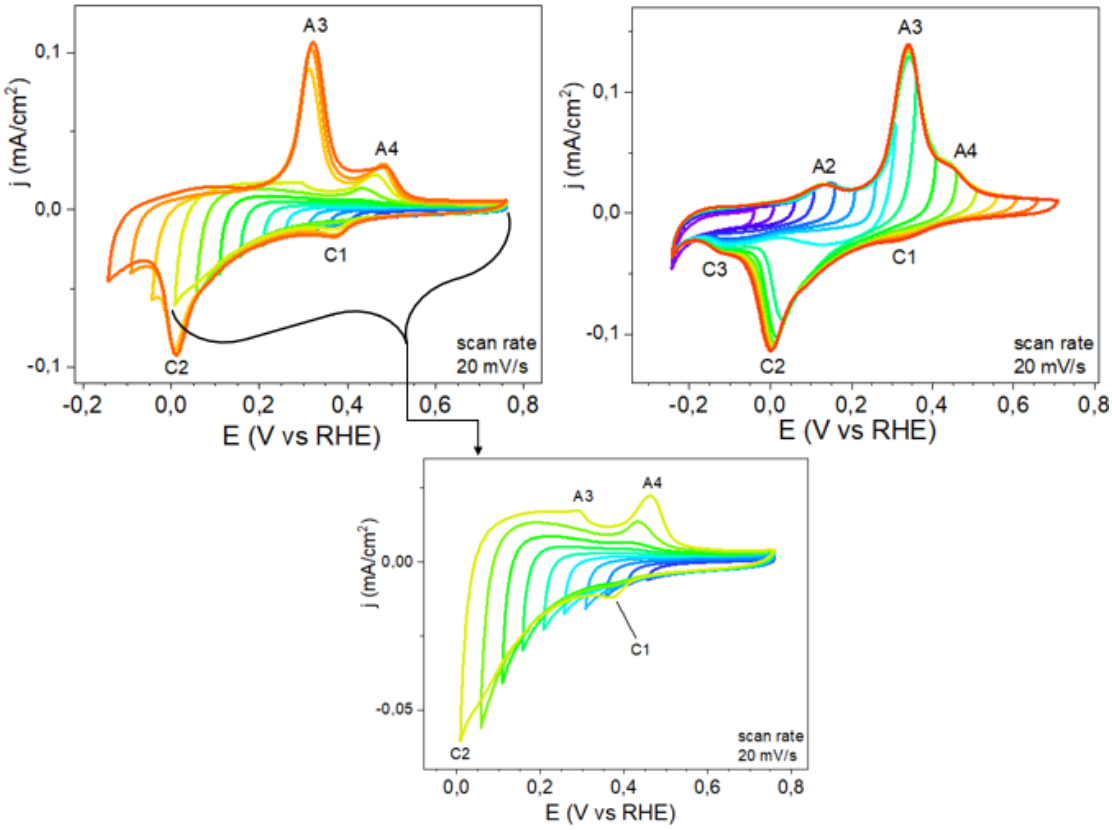

Figure 3-34: potential extended CVs taken at constant UVP (top-left) with zoom limited to the C2 peak onset (bottom), constant LVP (top-right)

3.5.1.1.1 Cyclic voltammetry fluxing fresh electrolyte.

Since the solute species $HFeO_2^-$ is present in solution during the measurements, to exclude the possibility that A4 oxidation peak (that is independent on the coverage, as the $HFeO_2^-$ concentration) was related to its oxidation, fresh electrolyte was fluxed while measuring the CV to take down to almost zero the concentration of the $HFeO_2^-$ species. A shown in figure 3-35, the A4 peak did not disappear (the shift of the CV is given by the flux of electrolyte), so the A4 peak is not related to the oxidation of the solute species $HFeO_2^-$, we associated it to the oxidation of the Iron oxide inner compact layer in contact with the Gold surface. The complete assignation of redox peaks is reported in table 3-3.

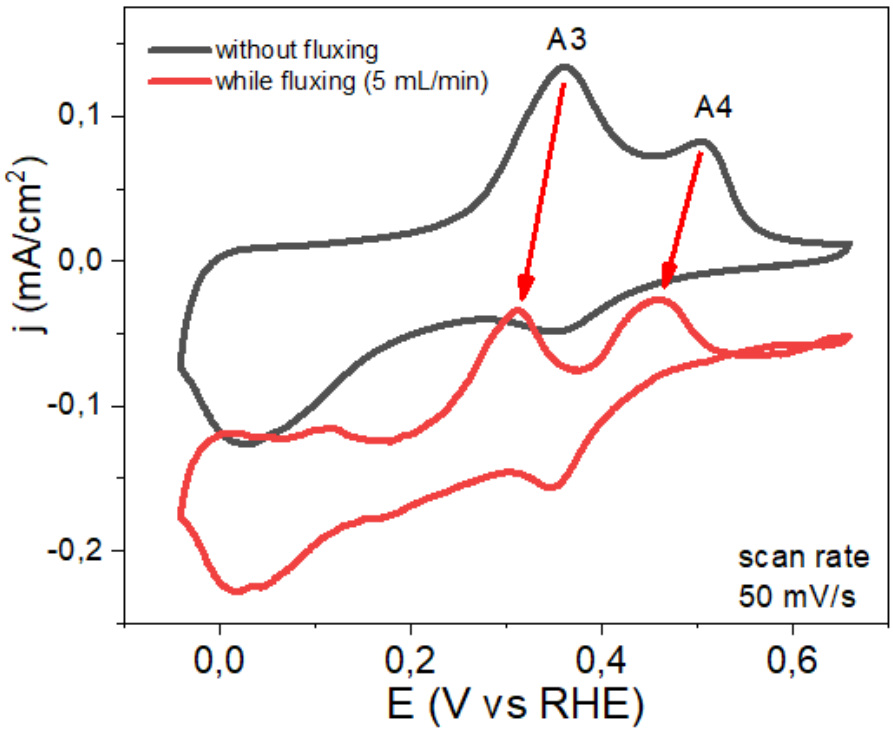

Figure 3-35: comparison between the CV measured with static electrolyte (black) and while fluxing fresh electrolyte (red)

Table 3-3: oxidation reaction for each Iron peak

Peak	Oxidation reaction
A1 (C4)	**$Fe + OH^- \rightarrow Fe(OH)_{ads} + e^-$**
A2 (C3)	**$Fe(OH)_{ads} + 2OH^- \rightarrow HFeO_2^-(aq) + H_2O + e^-$**
	$HfeO_2^-(aq) + H_2O \rightarrow \downarrow Fe(OH)_2(s) + OH^-$
A3 (C2)	**Outer hydrous oxide** **$Fe(OH)_2 + OH^- \rightarrow FeOOH + H_2O + e^-$**
A4 (C1)	**Inner compact oxide** **$FeO + xOH^- \rightarrow Fe_3O_4/Fe_2O_3 + xe^- + yH_2O$**

3.5.1.2 Hydrogen Evolution Reaction - Linear Sweep Voltammetry

The LSV of the multilayer sample, taken after the outer layer growth, is shown in figure 3-36. An overpotential at 1 mA/cm^2 of -0.60 V was found. The HER onset potential is difficult to determine by the reduction peak to metallic Fe situated at -0.39 V.

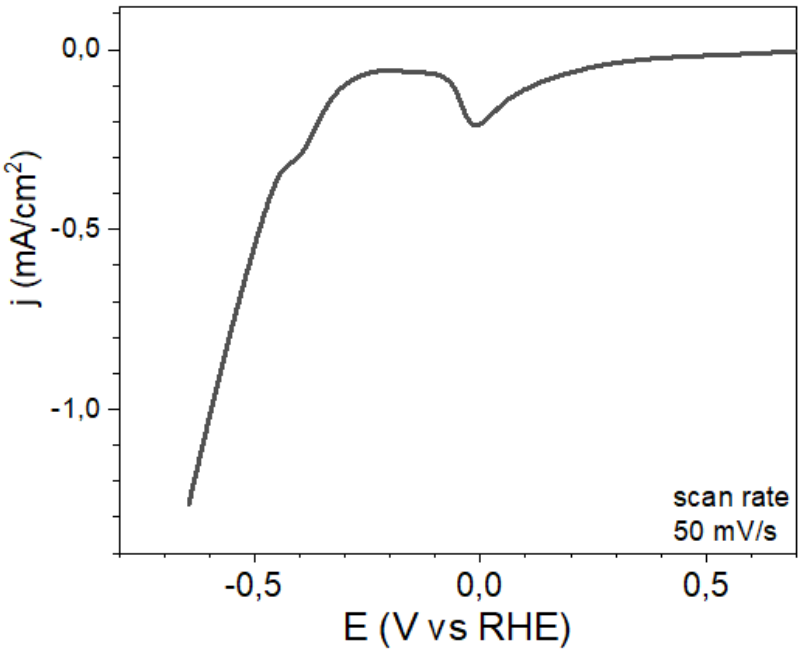

Figure 3-36: LSV of the multilayer sample in KOH 0.1 M

3.5.2 XPS

In the XPS survey spectrum, showed in figure 3-37 on the left, peaks of Oxygen (O 1s at 530.0 eV) and Iron (Fe2p and Auger LMM) are easily identifiable, given the high amount of Iron oxide deposited. The high-resolution spectrum of Fe 2p peak, in figure 3-37 on the right, agrees with a spinel phase, Fe_3O_4, as explained in the paragraph *3.3.2*.

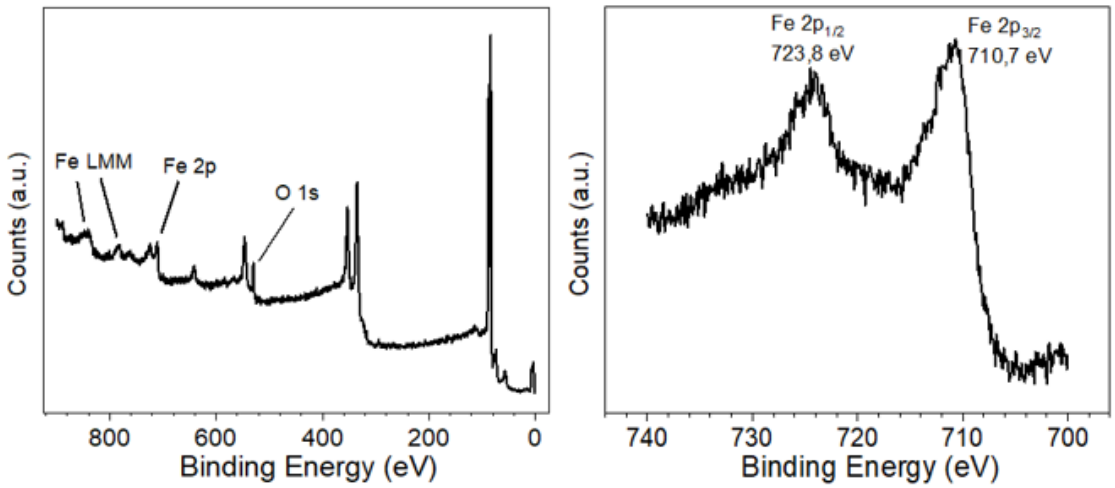

Figure 3-37: Left) XPS survey spectrum of Fe_3O_4/Au(111); Right) XPS spectrum of Fe 2p peaks.

After electrochemistry measurements, so after the exposition of the material to KOH 0.1 M, XPS spectra of Fe 2p peak did not change greatly, because of the great similarity between the Fe 2p peak of FeOOH (probably the outermost phase) and Fe_3O_4 (under the FeOOH of the surface) phases. O 1s peak broadened since the peaks related to OH and H_2O appeared, as shown in figure 3-38 at the bottom. The ratio between OH peak and lattice Oxygen one is greater than in subMLE but smaller than in the thick layer, confirming that the outer layer is mainly composed by hydroxylated Fe.

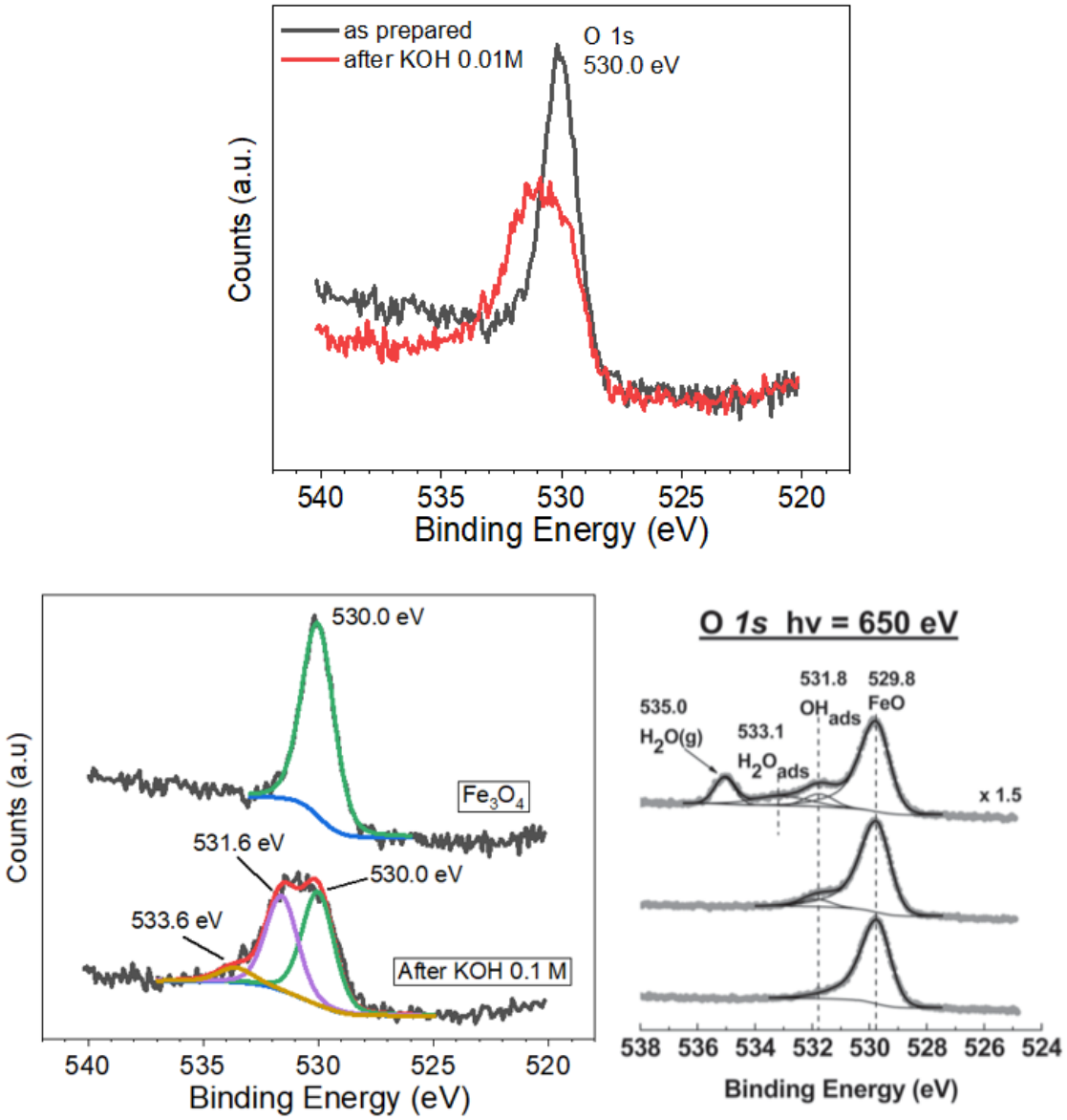

Figure 3-38: Top) XPS spectra of O 1s peak as prepared (black) and after electrochemistry measurements (red) Bottom-left) fit of the O1s peak showing the presence of new peak related to OH and H_2O Oxygen at 531.6 and 533.6 eV, respectively, after electrochemistry. Bottom-right) XPS fit of O 1s peak for hydroxylated FeO. Reproduced from Ref. 119.

3.5.3 LEED

As shown in figure 3-39, the LEED pattern exhibited a weak 2 x 2 superstructure (only the first order of diffraction was detectable) on Au(111), confirming a spinel phase, but less thick than the high coverage sample in which diffraction spots were more clearly visible (figure 3-27).

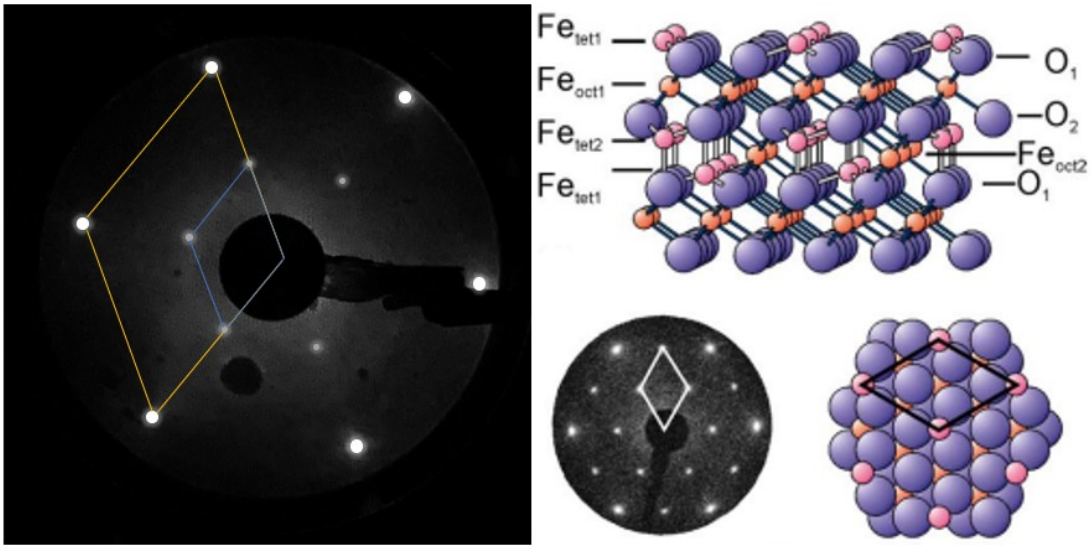

Figure 3-39: Left) measured LEED pattern at 55 eV; Right) at the top, structure of Fe_3O_4, at the bottom LEED pattern at 60 eV and structure of the Fe_3O_4 (111) Fe_{tet1} terminated surface. Reproduced from Ref. 122.

3.5.4 EC-STM

As shown in figure 3-40, the 70x70 nm^2 of surface was investigate in the potentials ranging from 0.100 V to - 0.350 V vs RHE (-0.800 to -1.250 vs Pt) and then anodically until to 0.450 V vs RHE (-0.550 V vs Pt). From 0.100 V to -0.100 V vs RHE (-0.800 to -1.000 V vs Pt), shown in the images 1 to 3 in figure 3-40, no great changes are detectable on the surface, during HER (image 4) the noise increases a lot, since hydrogen is being produced and affecting EC-STM measurements, as described in literature[98]. The white protrusions in the fifth image may correspond to the hydroxylation of the surface. After HER, going anodically from -0.050 to 0.350 V vs RHE (-1.050 to -0.550 V vs Pt), from image 5 to 8 in figure 3-40, a significant smoothing of the surface is observed. This phenomenon has been observed as formation of passivation of Iron[126], the detailed analysis of these pictures is still under investigation.

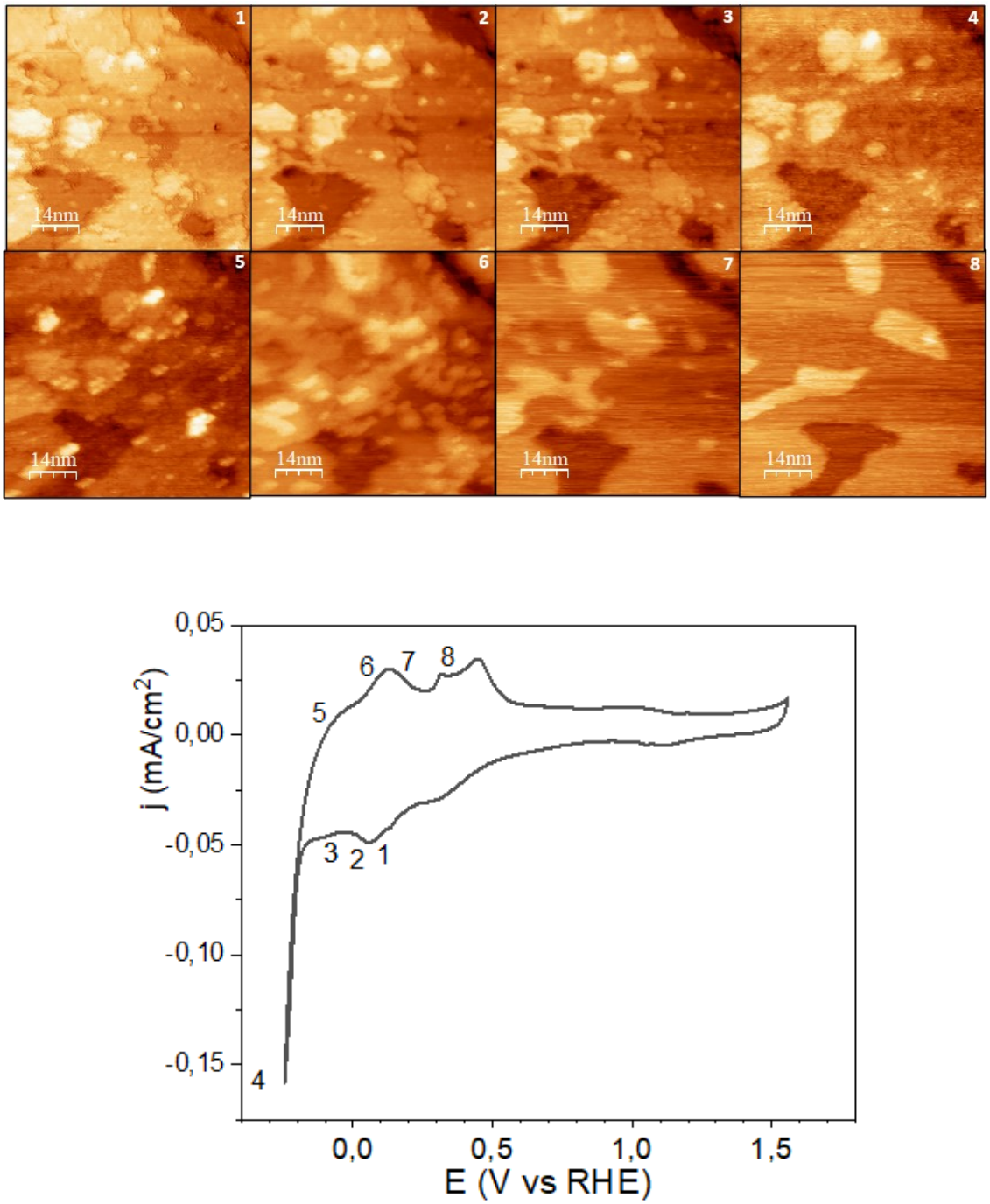

Figure 3-40: Top) EC-STM 70x70 nm² images of the surface nearby the HER potential range Bottom) Reference CV, the numbers indicate the point of the CV at which the images were taken.

Table 3-4: tunnelling current, bias potential, electrochemical current and electrodic potential for each EC-STM image.

	I_T (nA)	U_T (V)	I_S (µA)	U_S (V vs RHE)	U_S (V vs Pt)
1	5.89	0.111	-0.53	0.100	-0.800
2	5.89	0.324	-0.50	0.000	-0.900
3	5.89	0.324	-0.57	- 0.100	-1.000
4	5.89	0.455	-10	- 0.350	-1250 (HER)
5	5.89	0.455	-0.7	- 0.150	-1.050
6	5.89	0.300	-0.47	0.050	-0.850
7	5.89	0.241	-0.43	0.150	-0.750
8	5.89	0.329	-0.37	0.350	-0.550

The complexity of EC-STM imaging may be also related to the combination of speed of scanning of the STM and changing EC potential. When the images are acquired rapidly, in few seconds, the layers might not have time to reorganize in the most stable configurations. This add a further complexity of this imaging technique and further analysis will be undertaken.

3.6 Comparison between Θ < 1, Θ ≈ 1.5 and Θ > 5 MLE

3.6.1 Electrochemistry

3.6.1.1 Cyclic Voltammetry

The CVs of the three different covered samples show strong similarity before the growth of the outer layer, as shown in figure 3-41 at the top. The A3 peak is detectable even before the OL growth in all the three cases, revealing the presence of defects on the surface. Gold peaks are not visible for the multilayer and high coverage samples.

The comparison between the CVs of the three different coverages, in figure 3-41 at the bottom, shows the entity of the A3 and C2 peaks increase with the amount of Iron. The Gold peaks (on the right in the CV) decrease until disappearing with the increase of Iron deposited since the surface is covered and Gold is passivated by the Iron oxide film.

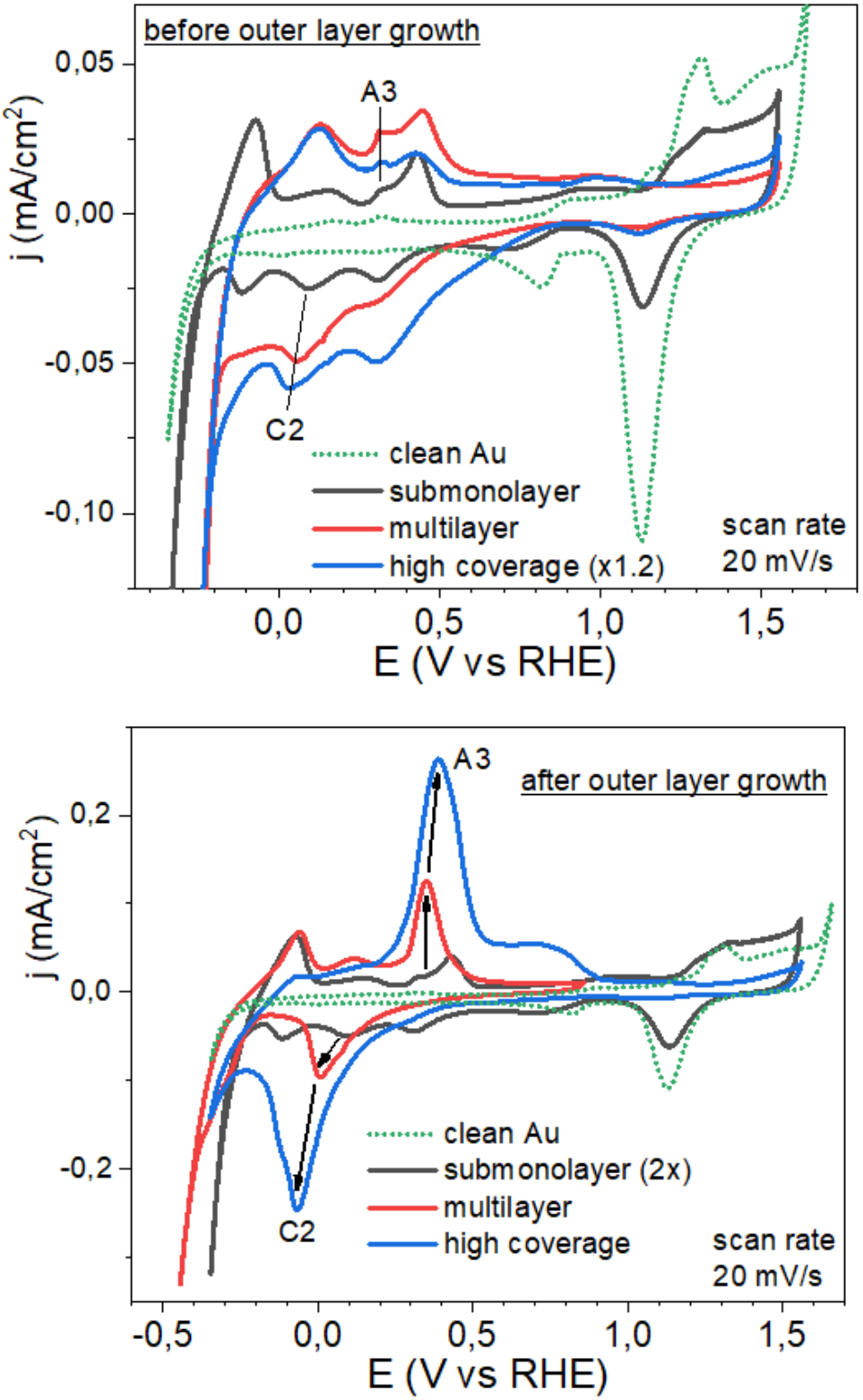

Figure 3-41: Top) comparison between the CVs of subMLE, multilayer and high coverage samples before outer layer growth; Bottom) comparison between the CVs of subMLE, multilayer and high coverage samples after outer layer growth.

3.6.1.2 Hydrogen Evolution Reaction - Linear Sweep Voltammetry

It is possible to reconstruct the behaviour of the system also looking at figure 3-42. Pristine Au(111) shows the worst activity toward HER, so as expected Iron oxide improves the HER performance. The samples with the outer layer grown show worse activities, the reason of this may be found in the growth of the outer porous layer, which traps the produced gaseous hydrogen "poisoning" the catalyst. The most active sample is the high coverage one, where Gold is completely covered and the Iron full MLE (so the amount of Iron that participate to the reaction is higher with respect to the subMLE sample) still compact. It was also proved by EC-STM that this so called "compact" layer is formed by the dissolution and redeposition in many small particles of Iron particles that, if the quantity of Iron is enough, can cover the Gold surface.

Iron may exhibit a lower energy barrier for water dissociation (Volmer step), known to be the RDS on Gold[103,104], either Iron may suffer less than Gold the poisoning due to the UPD of the alkali metal (potassium in this case). The subMLE sample is the second most active catalyst and it is stable after repeated LSV, the interplay between Iron and uncovered Gold may also play a role to be further investigated.

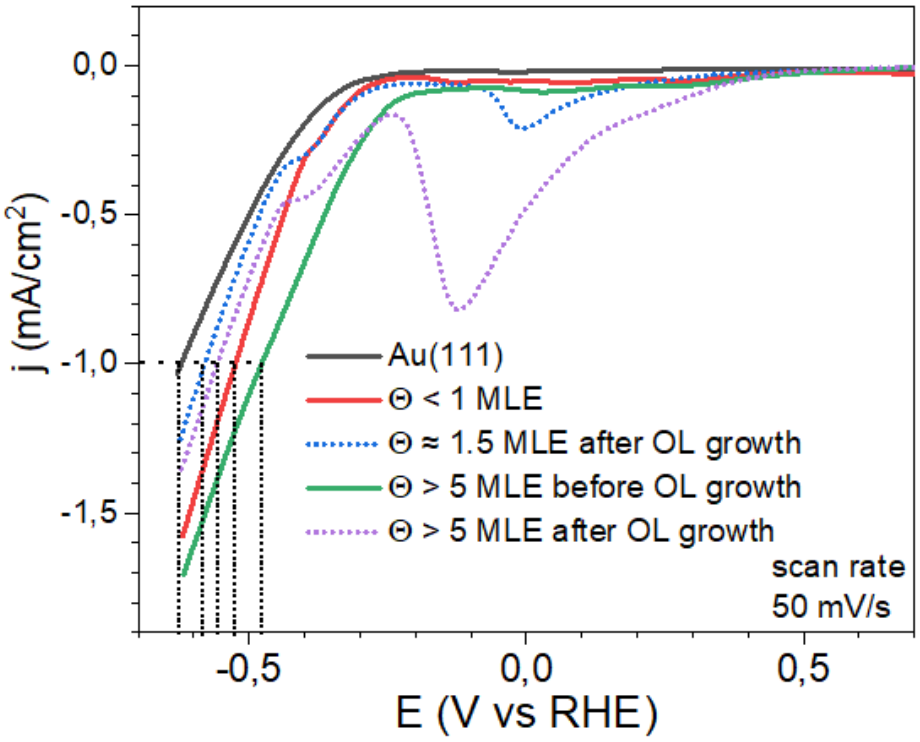

Figure 3-42: comparison between LSVs of different coverage.

Table 3-5: comparison of overpotential at 1 mA/cm² for different coverages.

η @ 1 mA/cm² (V vs RHE)	Au(111)	Θ<1ML	Θ≈1.5ML after OL	Θ>5ML before OL	Θ>5ML after OL
	-0.63	-0.52	-0.58	-0.48	-0.56

3.6.2 XPS

In the comparison of the XPS high-resolution spectra of Fe 2p, shown in figure 3-43 on the left, it is clearly visible the increasing in intensity with the amount of Iron; the Fe $2p_{3/2}$ peak position stays the same with similar shapes, hence the Iron oxide phase is in all the three samples the spinel Fe_3O_4. In figure 3-43 on the right, it can be appreciated the decreasing of Au 4f peak with increasing the Iron oxide present on its surface.

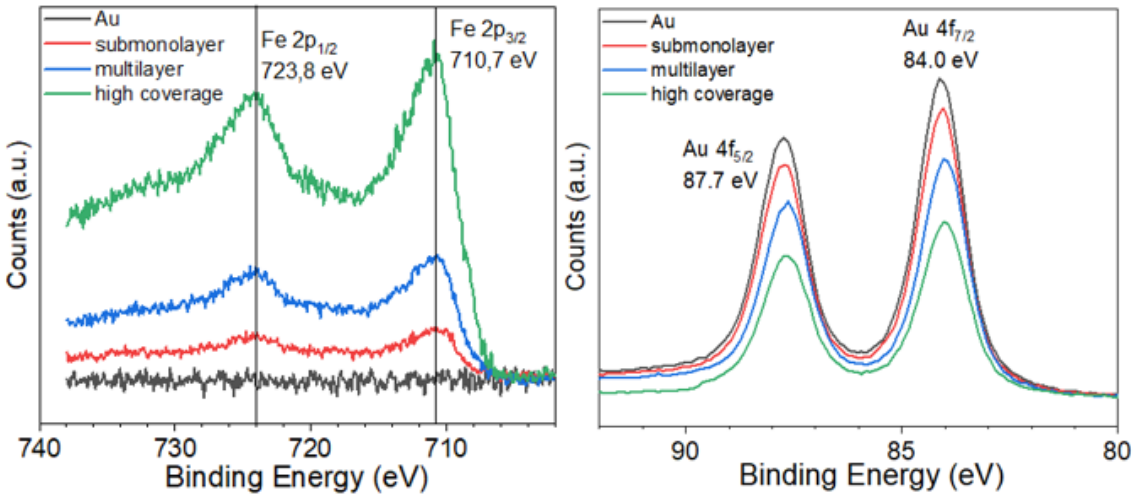

Figure 3-43: Left) comparison of the Fe 2p and (right) Au 4f XPS spectra for different coverages.

3.7 Mn Dual Atom / 1MLE Fe_3O_4 / Au (111)

On a Fe_3O_4/Au(111) MLE substrate, a Mn was deposited via MOCVD adapted to UHV conditions. The precursor, $Mn_2(CO)_{10}$, was heated up to 90-100 °C (its decomposition occurs at temperatures higher than 110 °C[70,71]) to increase its vapour pressure (which is ≈ 6.82 Torr at room temperature[70]) and dosed *via* a leak valve at a pressure of $4 \cdot 10^{-6}$ Torr, with the substrate kept at room temperature.

3.7.1 Electrochemistry

3.7.1.1 Cyclic Voltammetry

As shown in figure 3-44, the sample was stabilized in a safe range of potential, excluding metallic Iron region to avoid the eventual growth of an outer layer and oxidative potentials over 0.8 V were also excluded to avoid the formation of the very soluble permanganate ion MnO_4^-, with consequent loss of the Mn.

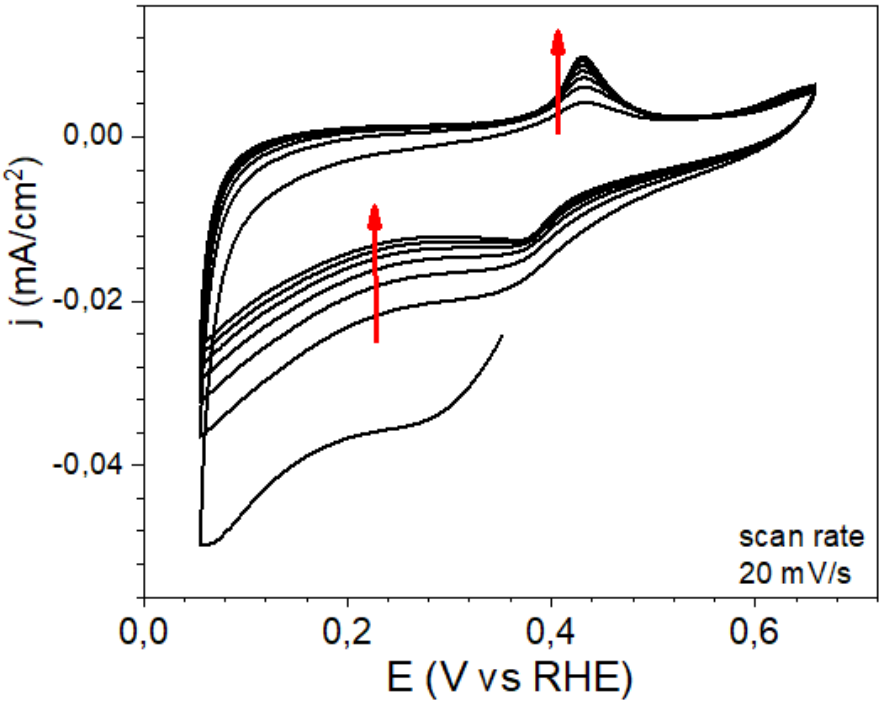

Figure 3-44: stabilization CVs, 10 cycles at a scan rate of 20 mV/s.

The sample was tested in three different conditions:

- as prepared (after stabilization shown in figure 3-44) to probe the activity in presence of Mn DAs;

- after having dissolved Mn by extending the potential range anodically to 1.8 V to oxidize it and solubilize it as MnO_4^-, in order to compare the activity of the very same sample but in absence of Mn DAs;
- finally, after having chemically lowered the Iron oxide coverage by means of 30 cycles between -0.2 and 2.2 V vs RHE at 100 mV/s scan rate and fluxing 10 mL of fresh electrolyte, to have a comparison with the subMLE activity.

In figure 3-45 the CV of the sample as prepared and at the end, on the left and on the right, respectively; after having cycled and fluxed fresh electrolyte, Gold peaks are much more visible since Iron has been removed and Gold uncovered.

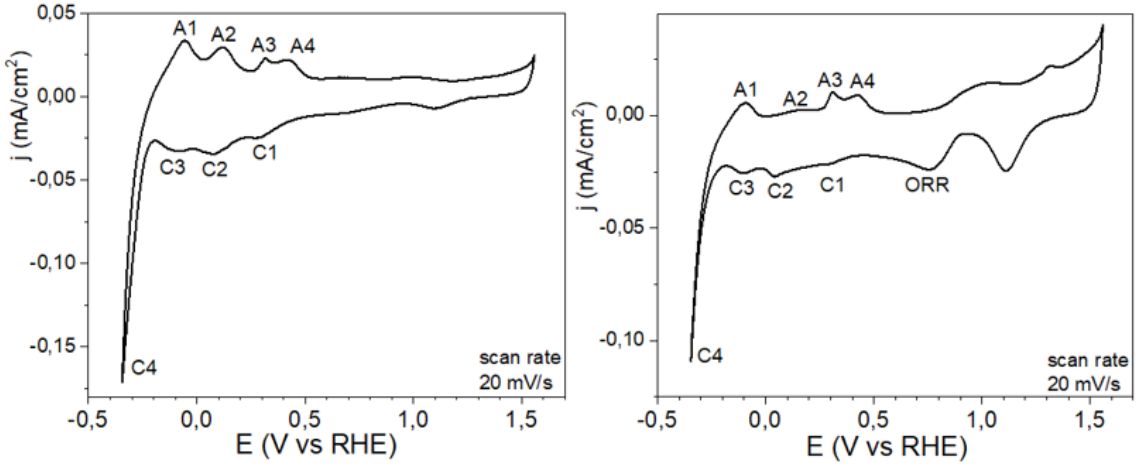

Figure 3-45: Left) CV of the sample as prepared; Right) CV of the sample after 30 cycles and having fluxed 10mL fresh electrolyte.

3.7.1.2 Hydrogen Evolution Reaction - Linear Sweep Voltammetry

The most active catalyst, as shown in figure 3-46, is the sample as prepared, with Mn Dual Atom Catalyst (DAC), that shows a significantly lower overpotential at 1 mA/cm^2 of -0.53 V with respect to the other two samples, but still worse than the high coverage sample before the outer layer growth, which exhibits a -0.48 V overpotential at 1 mA/cm^2. Mn as DA provides, in fact, two very close sites as well as many oxidation states that may stabilize the reaction intermediates, resulting in a facilitated water dissociation.

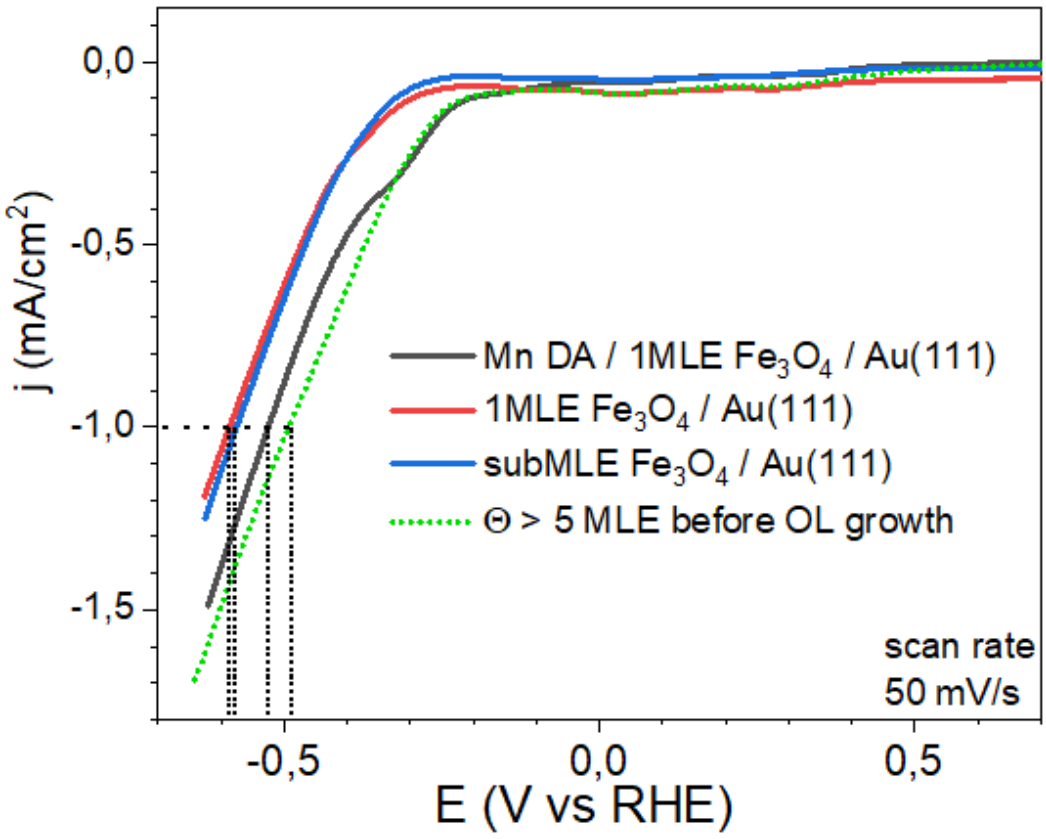

Figure 3-46: comparison of LSVs of the sample as prepared (black), after removing Mn (red) and after having partially removed Iron (blue)

Table 3-6: comparison of overpotential at 1 mA/cm² for the sample as prepared, after removing Mn and after having partially removed Iron.

η @ 1 mA/cm² (V vs RHE)	**Mn DA / 1MLE Fe_3O_4 / Au(111)**	**1MLE Fe_3O_4 / Au(111)**	**subMLE Fe_3O_4 / Au(111)**
	-0.53	-0.58	-0.59

3.7.2 XPS

The XPS survey spectrum, shown in figure 3-47, shows the set of Gold, Oxygen and Iron peaks. Iron oxide is present in the spinel phase, as deduced by the high resolution spectrum of Fe 2p peaks as reported before, in figure 3-48 on the left (12-31/35). Manganese, being present in very little amount, is visible only in the high-resolution spectrum of Au $4p_{1/2}$ – Mn 2p peaks, reported in figure 3-51 on the right, comparing the signals of Fe_3O_4/Au(111) with the one after Mn deposition.

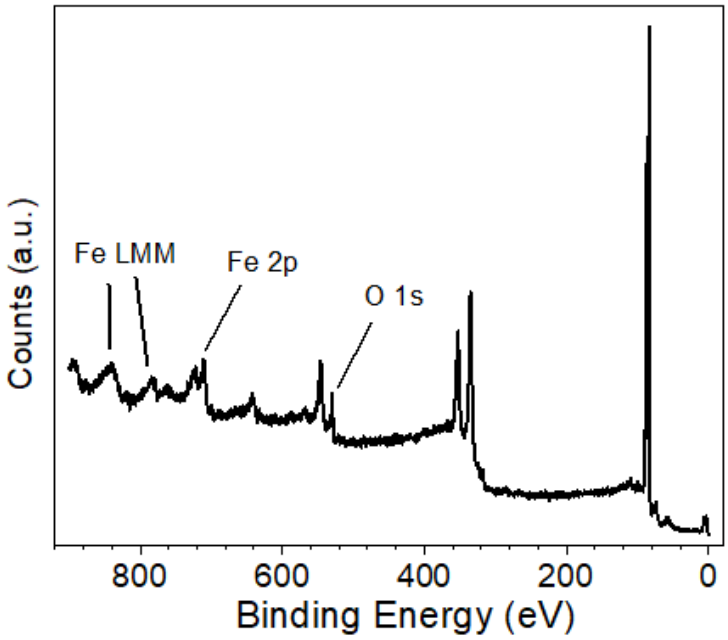

Figure 3-47: XPS survey spectrum of the sample as prepared

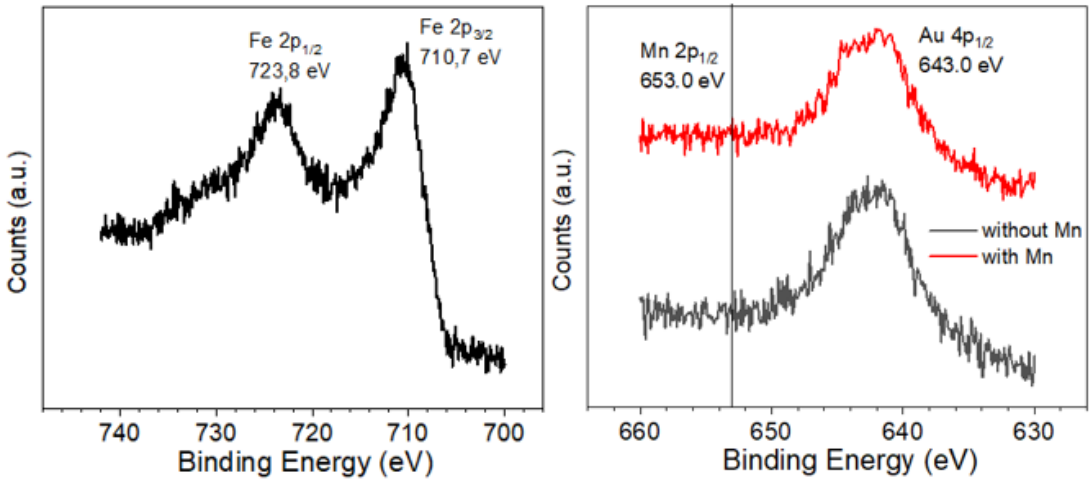

Figure 3-48: XPS spectra of Fe 2p peak (left) and Au $4p_{1/2}$ / Mn 2p peaks (right), both taken on the sample as prepared.

Conclusions

The catalytic performance toward HER and the EC behaviour in alkaline medium of epitaxial Fe_3O_4/Au(111) were investigated at different coverages. The EC studied were performed by and in-situ EC cell with precise control over the environment and material growth conditions.

Before testing the HER performance the oxide layers were stabilized by CVs recorded between -0.25 and 1.55 V vs RHE. In the subMLE coverage, a complex CV was recorded and no significant EC changes were observed during the stabilization. In contrast, for samples with coverage above the MLE, Gold redox peaks were initially visible, due to the Fe_3O_4 island growth mode that leaves some Gold uncovered; however, they disappeared within few CV cycles. We attribute this behaviour to the formation of a soluble species, $HFeO_2^-$ that precipitates rapidly as $Fe(OH)_2$. This is a known behaviour for bulk Iron in alkaline medium.

Very interestingly in the subMLE these macroscopic EC finding hinted to an idle situation with a probable stabilization of the Fe_3O_4 in subMLE form. However, investigation by in-operando EC-STM revealed drastic changes of the surface, even for subMLE coverages, as shown in figure 4-1. Gold redox peak in EC experiments did not disappear for the low quantity of Fe_3O_4 deposited but a clear reorganization was evident, transitioning from large triangular NPs to a rough surface.

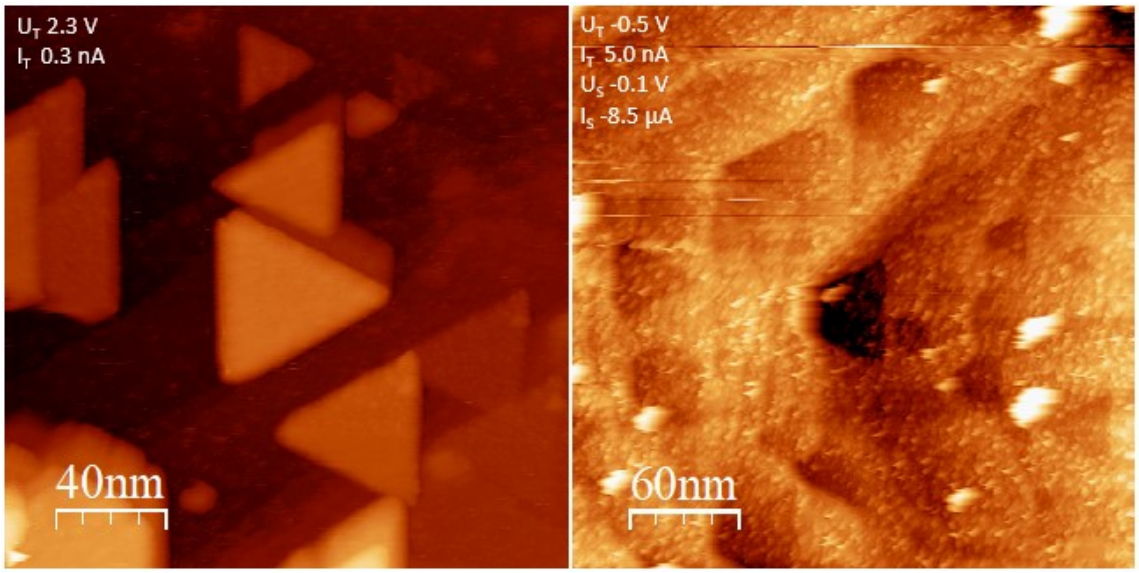

Figure 0-1: STM image of the subMLE sample as prepared scanned in air (left) and after 10 cycles stabilization scanned in electrolyte at -0.1 V vs RHE (right)

After activation CVs of the catalysts described above, the most active sample for HER, as shown if Figure 4-2, was the one with the highest coverage, Θ≈5MLE. This enhanced activity is attributed to the higher amount of Iron available, combined with a fully covered Gold surface. It's worth noting that the Gold surface can be susceptible to poisoning due to the UPD of potassium.

However, a new effect has been observed: the high coverage sample's activity deteriorated after the first LSV to HER. Indeed, to reach the potential for hydrogen evolution, the sample passed the threshold of -0.4 V vs RHE and became metallic. Subsequent oxidation of this metallic phase led to the so-called "outer layer growth". This outer layer has a porous structure, which we believe hinders the diffusion of generated H_2 and consequently decrease HER performances. The CV and EC behaviours of thick layer of magnetite after the outer layer growth became similar to what is observed for bulk Fe samples.

To better understand the conditions of outer hydrous layer growth, we exploited the possibility of choosing a well-defined thickness of magnetite, in contrast to conventional studies on bulk Fe. A sample with intermediate coverage of about 1.5 MLE was studied and CV scanning was performed extending the potential range just about to activate the

reduction of Iron to the elemental state (-0.4 V vs RHE). The transformation of complex subMLE CV to a conventional bulk-like CV was observed and by the gradual “outer layer growth”, as shown in figure 4-2.

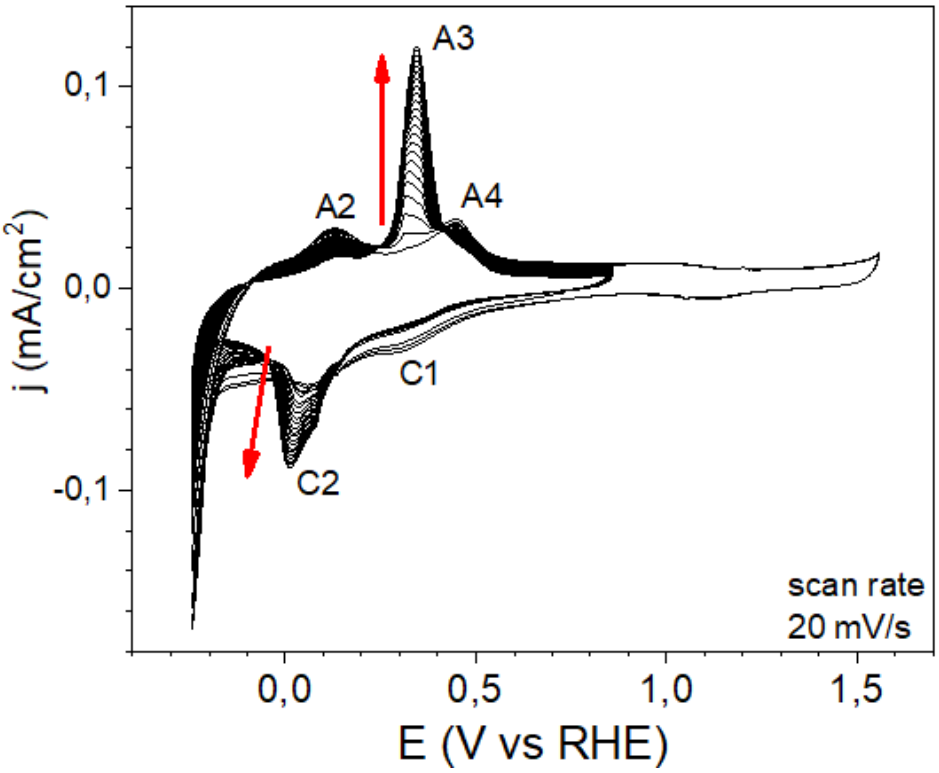

Figure 0-2: CV showing the gradual the growth of the A3 peak in the sample with coverage Θ≈1.5.

Finally, to improve the performance of the samples in HER, Mn DAs was deposited at ultralow coverage on a 1 MLE of magnetite. This resulted to be the second most active sample, suggesting that Mn DAC may enhance the reaction by reducing the activation energies through the provision of two closely spaced sites for the adsorption of reaction intermediates. Notably, in the case of LSVs taken on the subMLE or 1 MLE of magnetite both with and without Mn there were no observable changes after consecutive LSV measurements. This lack of change indicates the absence of “outer layer growth”, which in case of multilayers has a detrimental effect on performance. Therefore, even though they may exhibit slightly lower performance, these samples are considered much more stable than thicker layers.

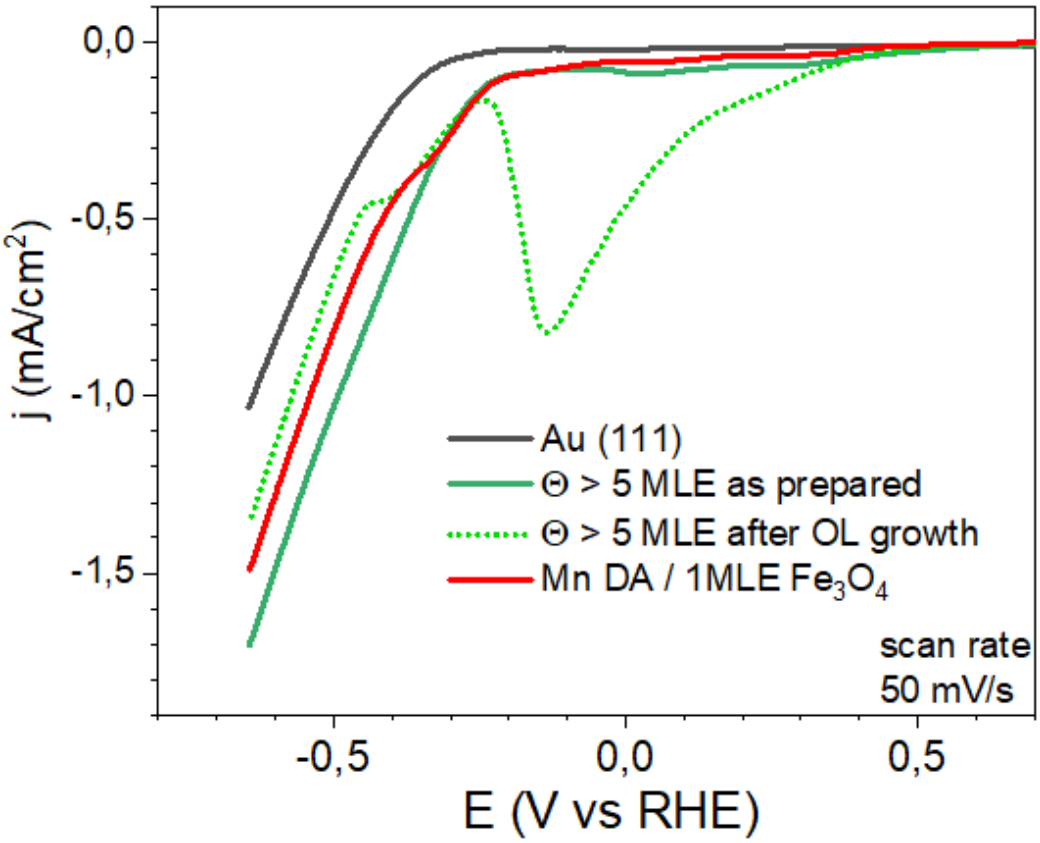

Figure 0-3: comparison of LSV of the clean Au(111) (black), high coverage sample before (green solid line) and after (light-green dotted line) the outer layer growth and of the MLE sample decorated with Mn DAs (red line).

To summarize, in this thesis Fe_3O_4 was synthesized as a model system to gain insights into the electrocatalytic performance of ultra-thin Fe and NPs in alkaline media. State-of-the-art characterizations, such as EC-STM and in-situ EC, provided an unprecedented understanding of the relationship between electrochemical behaviour and morphological changes in the electrocatalyst. We successfully distinguished the activation and reorganization of oxide phases from the outer layer growth, the latter has been found for multilayers. The addition of Mn DAC demonstrated the versatility of this model system in exploring even more complex electrocatalysts, forming the basis for future studies.

References

1. Lenssen, N. J. L. *et al.* Improvements in the GISTEMP Uncertainty Model. *JGR Atmospheres* **124**, 6307–6326 (2019).
2. Calvin, K. *et al.: Climate Change 2023: Synthesis Report. Contribution of Working Groups I, II and III to the Sixth Assessment Report of the Intergovernmental Panel on Climate Change, IPCC,* (2023) .
3. US Department of Commerce, N. Global Monitoring Laboratory - Carbon Cycle Greenhouse Gases. https://gml.noaa.gov/ccgg/trends/global.html.
4. Friedlingstein, P. *et al.* Global Carbon Budget 2022. *Earth Syst. Sci. Data* **14**, 4811–4900 (2022).
5. Climate Change Impacts Data Explorer. *Our World in Data* https://ourworldindata.org/explorers/climate-change.
6. Gerretsen, I. The state of the climate in 2023. https://www.bbc.com/future/article/20230317-the-state-of-the-climate-in-2023.
7. Ritchie, H. *et al.* CO_2 and Greenhouse Gas Emissions. *Our World in Data* (2020).
8. https://www.drjez.com/uco/ChemTools/Standard%20Thermodynamic%20Values.pdf.
9. Morgan, T. & Programme, U. N. E. *The Hydrogen Economy: A Non-technical Review. UNEP* (2006).
10. Bhandari, R. *et al.* Life cycle assessment of hydrogen production via electrolysis – a review. *Journal of Cleaner Production* **85**, 151–163 (2014).
11. Morales-Guio, C. *et al.* Nanostructured hydrotreating catalysts for electrochemical hydrogen evolution. *Chem. Soc. Rev.* **43**, 6555 (2014).
12. Sheng, W. *et al.* Hydrogen Oxidation and Evolution Reaction Kinetics on Platinum: Acid vs Alkaline Electrolytes. *J. Electrochem. Soc.* **157**, B1529 (2010).
13. Hu, C. *et al.* Recent progress made in the mechanism comprehension and design of electrocatalysts for alkaline water splitting. *Energy Environ. Sci.* **12**, 2620–2645 (2019).
14. Markovića, N. *et al.* Hydrogen electrochemistry on platinum low-index single-crystal surfaces in alkaline solution. *J. Chem. Soc., Faraday Trans.* **92**, 3719–3725 (1996).
15. Durst, J. *et al.* New insights into the electrochemical hydrogen oxidation and evolution reaction mechanism. *Energy Environ. Sci.* **7**, 2255–2260 (2014).
16. Zheng, Y. *et al.* The Hydrogen Evolution Reaction in Alkaline Solution: From Theory, Single Crystal Models, to Practical Electrocatalysts. *Angew. Chem. Int. Ed.* **57**, 7568–7579 (2018).
17. Sheng, W. *et al.* Correlating the hydrogen evolution reaction activity in alkaline electrolytes with the hydrogen binding energy on monometallic surfaces. *Energy Environ. Sci.* **6**, 1509 (2013).
18. Ursua, A. *et al.* Hydrogen Production From Water Electrolysis: Current Status and Future Trends. *Proc. IEEE* **100**, 410–426 (2012).
19. Gilliam, R. *et al.* A review of specific conductivities of potassium hydroxide solutions for various concentrations and temperatures. *International Journal of Hydrogen Energy* **32**, 359–364 (2007).
20. Ivy, J. Summary of Electrolytic Hydrogen Production: Milestone Completion Report, *OSTI* (2004).

21. Roy, A. Dynamic and transient modelling of electrolysers by renewable energy sources and cost analysis of electrolytic hydrogen. (2006).
22. Ulleberg, O. Modeling of advanced alkaline electrolyzers: a system simulation approach. *International Journal of Hydrogen Energy* **28**, 21–33 (2003).
23. Accelera | Powering the World with Clean Energy. https://www.accelerazero.com/.
24. Du, N. *et al.* Anion-Exchange Membrane Water Electrolyzers. *Chem. Rev.* **122**, 11830–11895 (2022).
25. Kraglund, M. R. *et al.* Ion-solvating membranes as a new approach towards high rate alkaline electrolyzers. *Energy Environ. Sci.* **12**, 3313–3318 (2019).
26. Anantharaj, S. *et al.* "The Fe Effect": A review unveiling the critical roles of Fe in enhancing OER activity of Ni and Co based catalysts. *Nano Energy* **80**, 105514 (2021).
27. Parkinson, G. S. Iron oxide surfaces. *Surface Science Reports* **71**, 272–365 (2016).
28. Ketteler, G. *et al.* Bulk and surface phases of iron oxides in an oxygen and water atmosphere at low pressure. *Phys. Chem. Chem. Phys.* **3**, 1114–1122 (2001).
29. Vodyanitskii, Yu. N. Iron hydroxides in soils: A review of publications. *Eurasian Soil Sc.* **43**, 1244–1254 (2010).
30. Zepeda-Alarcon, E. *et al.* Magnetic and nuclear structure of goethite (α-FeOOH): a neutron diffraction study. *J Appl Cryst* **47**, 1983–1991 (2014).
31. Freund, H.-J. *et al.* Chapter model systems in heterogeneous catalysis at the atomic level: a personal view. *Sci. China Chem.* **63**, 426–447 (2020).
32. Grosse, P. *et al.* Dynamic transformation of cubic copper catalysts during CO_2 electroreduction and its impact on catalytic selectivity. *Nat. Commun.* **12**, 6736 (2021).
33. Mom, R. V. *et al.* Assessment of the Degradation Mechanisms of Cu Electrodes during the CO_2 Reduction Reaction. *ACS Appl. Mater. Interfaces* **15**, 30052–30059 (2023).
34. Velasco-Vélez, J. *et al.* Cationic Copper Species Stabilized by Zinc during the Electrocatalytic Reduction of CO_2 Revealed by In Situ X-Ray Spectroscopy. *Advanced Sustainable Systems* **7**, 2200453 (2023).
35. Martini, A. *et al.* Tracking the Evolution of Single-Atom Catalysts for the CO_2 Electrocatalytic Reduction Using Operando X-ray Absorption Spectroscopy and Machine Learning. *J. Am. Chem. Soc.* **145**, 17351–17366 (2023).
36. Roldan Cuenya, B. *et al.* Potential-Dependent Morphology of Copper Catalysts During CO_2 Electroreduction Revealed by In Situ Atomic Force Microscopy. *Angew. Chem. Int. Ed.* **60**, 2561–2568 (2021).
37. Wartner, G. *et al.* Insights into the electronic structure of Fe–Ni thin-film catalysts during the oxygen evolution reaction using *operando* resonant photoelectron spectroscopy. *J. Mater. Chem. A* **11**, 8066–8080 (2023).
38. Haase, F. T. *et al.* Size effects and active state formation of cobalt oxide nanoparticles during the oxygen evolution reaction. *Nat. Energy* **7**, 765–773 (2022).

39. Deciphering the Structural and Chemical Transformations of Oxide Catalysts during Oxygen Evolution Reaction Using Quick X-ray Absorption Spectroscopy and Machine Learning. *J. Am. Chem. Soc.* **145**, 4065−4080 (2023)
40. Wang, J. *et al.* Non-precious-metal catalysts for alkaline water electrolysis: *operando* characterizations, theoretical calculations, and recent advances. *Chem. Soc. Rev.* **49**, 9154–9196 (2020).
41. Zhao, T. *et al.* Design and operando/in situ characterization of precious-metal-free electrocatalysts for alkaline water splitting. *Carbon Energy* **2**, 582–613 (2020).
42. Tsai, F.-T. *et al.* The HER/OER mechanistic study of an FeCoNi-based electrocatalyst for alkaline water splitting. *J. Mater. Chem. A* **8**, 9939–9950 (2020).
43. Morgenstern, K. *et al.* Cobalt growth on two related close-packed noble metal surfaces. *Surface Science* **601**, 1967–1972 (2007).
44. Barth, J. V. *et al.* Scanning tunneling microscopy observations on the reconstructed Au(111) surface: Atomic structure, long-range superstructure, rotational domains, and surface defects. *Phys. Rev. B* **42**, 9307–9318 (1990).
45. Wu, C. *et al.* Ultrathin Oxide Films on Au(111) Substrates. in *Oxide Materials at the Two-Dimensional Limit* (eds. Netzer, F. P. & Fortunelli, A.) **234** 149–168 (Springer International Publishing, 2016).
46. Allmers, T. *et al.* Growth and morphology of thin Fe films on flat and vicinal Au(111): a comparative study. *New J. Phys.* **11**, 103049 (2009).
47. Voigtländer, B. *et al.* Epitaxial growth of Fe on Au(111): a scanning tunneling microscopy investigation. *Surface Science Letters* **255**, L529–L535 (1991).
48. Stroscio, J. A. *et al.* Microscopic aspects of the initial growth of metastable fcc iron on Au(111). *Journal of Vacuum Science & Technology A: Vacuum, Surfaces, and Films* **10**, 1981–1985 (1992).
49. Dekadjevi, D. T. *et al.* Structural phase transition of Fe grown on Au(111). *Phys. Rev. B* **71**, 054108 (2005).
50. Khan, N. A. *et al.* Nucleation and growth of Fe and FeO nanoparticles and films on Au(111). *Surface Science* **602**, 932–942 (2008).
51. Yang, S. *et al.* Precise determination of moiré pattern in monolayer FeO(111) films on Au(111) by scanning tunneling microscopy. *Phys. Rev. Materials* **4**, 074004 (2020).
52. Jiang, Y. *et al.* Two-Dimensional Iron Oxide on Au(111): Growth Mechanism and Interfacial Properties. *J. Phys. Chem. C* **125**, 24755–24763 (2021).
53. Deng, X. & Matranga, C. Selective Growth of Fe_2O_3 Nanoparticles and Islands on Au(111). *J. Phys. Chem. C* **113**, 11104–11109 (2009).
54. Deng, X. *et al.* Preparation and characterization of Fe_3O_4(111) nanoparticles and thin films on Au(111). *Surface Science* **604**, 627–632 (2010).
55. Yu, L. *et al.* CO Oxidation on Gold-Supported Iron Oxides: New Insights into Strong Oxide–Metal Interactions. *J. Phys. Chem. C* **119**, 16614–16622 (2015).

56. Schulz, H. Short history and present trends of Fischer–Tropsch synthesis. *Applied Catalysis A: General* **186**, 3–12 (1999).
57. Freund, H. J. *et al.* Oxide ultra-thin films on metals: new materials for the design of supported metal catalysts. *Chem. Soc. Rev.* **37**, 2224 (2008).
58. Weiss, W. *et al.* Surface chemistry and catalysis on well-defined epitaxial iron-oxide layers. *Progress in Surface Science **70**, 1-3* (2002).
59. Liu, H. L. *et al.* Synthesis of monosized magnetic-optical AuFe alloy nanoparticles. *Journal of Applied Physics* **103**, 07D529 (2008).
60. Ramesh, R. *et al.* Whither Oxide Electronics? *MRS Bull.* **33**, 1006–1014 (2008).
61. Nikiforov, M. P. *et al.* Epitaxial Electrodeposition of Fe_3O_4 on Single-Crystal Au(111). *Advanced Materials* **12**, 1351–1353 (2000).
62. Neri, G. *et al.* CO and NO_2 sensing properties of doped-Fe_2O_3 thin films prepared by LPD. *Sensors and Actuators B: Chemical* **82**, 40–47 (2002).
63. Lin, J. *et al.* Gold-Coated Iron (Fe@Au) Nanoparticles: Synthesis, Characterization, and Magnetic Field-Induced Self-Assembly. *Journal of Solid State Chemistry* **159**, 26–31 (2001).
64. Carpenter, E. E. *et al.* Effects of shell thickness on blocking temperature of nanocomposites of metal particles with gold shells. *IEEE Trans. Magn.* **35**, 3496–3498 (1999).
65. Zhou, W. L. *et al.* Transmission Electron Microscopy Study of Gold-Coated Iron Core-Shell and Au/Fe/Au Onion-Like Nanoparticles Synthesized using Reverse Micelles. *MRS Proc.* **581**, 107 (1999).
66. Carpenter, E. E. *et al.* Synthesis and magnetic properties of gold–iron–gold nanocomposites. *Materials Science and Engineering: A* **286**, 81–86 (2000).
67. EFM 3. *FOCUS GmbH* https://www.focus-gmbh.com/efm-evaporators/efm-3/.
68. EFM 3 - Scienta Omicron.
https://scientaomicron.com/en/Instruments/e-beam-evaporators/EFM-3.
69. Dimanganese decacarbonyl - Wikipedia. https://en.wikipedia.org/wiki/Dimanganese_decacarbonyl.
70. Christiansz, G. I. *et al.* Evaluation of some manganese feedstocks for MOCVD. *Journal of Crystal Growth* **93**, 589–593 (1988).
71. Brimm, E. O. *et al.* Preparation and Properties of Manganese Carbonyl. *J. Am. Chem. Soc.* **76**, 3831–3835 (1954).
72. Einstein, A. Über einen die Erzeugung und Verwandlung des Lichtes betreffenden heuristischen Gesichtspunkt. *Ann. Phys.* **322**, 132–148 (1905).
73. https://epm.univie.ac.at/research/low-dimensional-quantum-solids/methods/.
74. *Handbook of X-ray photoelectron spectroscopy: a reference book of standard spectra for identification and interpretation of XPS data*. (Perkin-Elmer Corporation, 1992).
75. Hofmann, S. *Auger- and X-Ray Photoelectron Spectroscopy in Materials Science: A User-Oriented Guide*. (Springer Science & Business Media, 2012).

76. Brisk, M. A. et al. Shake-up satellites in X-ray photoelectron spectroscopy. *Journal of Electron Spectroscopy and Related Phenomena* **7**, 197–213 (1975).
77. Yin, L. *et al.* Paramagnetism and Shake-Up Satellites in X-Ray Photoelectron Spectra. *Chemical Physics Letters* **24**, 1 (1974)
78. Gupta, R. P. *et al.* Calculation of multiplet structure of core p-vacancy levels. *Phys. Rev. B* **10**, 71–77 (1974).
79. Gupta, R. P. *et al.* Calculation of multiplet structure of core p-vacancy levels. II. *Phys. Rev. B* **12**, 15–19 (1975).
80. Biesinger, M. C. *et al.* Resolving surface chemical states in XPS analysis of first row transition metals, oxides and hydroxides: Cr, Mn, Fe, Co and Ni. *Applied Surface Science* **257**, 2717–2730 (2011).
81. Grosvenor, A. P. *et al.* Investigation of multiplet splitting of Fe 2p XPS spectra and bonding in iron compounds. *Surf. Interface Anal.* **36**, 1564–1574 (2004).
82. Davisson, C. *et al.*The Scattering of Electrons by a Single Crystal of Nickel. *Nature* **119**, 558–560 (1927).
83. Jonat, F. *et al.* Low-energy electron diffraction for surface structure analysis.
84. Speller, S. *et al.* Surface characterization: Composition, structure and topography. in *Experimental Methods in the Physical Sciences* (ed. Naiwa, H. S.) **38** 1–109 (Academic Press, 2001).
85. Marturi, N. Vision and visual servoing for nanomanipulation and nanocharacterization in scanning electron microscope. *Micro and nanotechnologies/Microelectronics*. Université de Franche-Comté (2013)
86. Kolasinski, K. W. *Surface Science: Foundations of Catalysis and Nanoscience*. (John Wiley & Sons, 2012).
87. Lazaga, M. A. *et al. Catalytic Selective Oxidation*. vol. 523 (American Chemical Society, 1993).
88. Bard, A. J. *et al.* Introductory lecture. Studies of the liquid/solid interface by scanning tunnelling microscopy and scanning electrochemical microscopy. *Faraday Disc.* **94**, 1 (1992).
89. Sonnenfeld, R. *et al.* Atomic-Resolution Microscopy in Water. *Science* **232**, 211–213 (1986).
90. Gewirth, A. A. *et al. Nanoscale Probes of the Solid/Liquid Interface*. (Springer Science & Business Media, 2013).
91. Aliofkhazraei, M. *Modern Electrochemical Methods in Nano, Surface and Corrosion Science*. (BoD – Books on Demand, 2014).
92. Schmickler, W. Electronic Effects in the Electric Double Layer. *Chem. Rev.* **96**, 3177–3200 (1996).
93. Hugelmann, M. *et al.* Tunnel barrier height oscillations at the solid/liquid interface. *Surface Science* **541**, L643–L648 (2003).
94. Schmickler, W. *et al.* A model for the scanning tunneling microscope operating in an electrolyte solution. *Journal of Electroanalytical Chemistry and Interfacial Electrochemistry* **290**, 283–291 (1990).
95. Sass, J. K. *et al.* Solvent dynamical effects in scanning tunneling microscopy with a polar liquid in the gap. *Journal of Electroanalytical Chemistry and Interfacial Electrochemistry* **308**, 333–337 (1991).

96. Halbritter, J. *et al.* Tunneling mechanisms in electrochemical STM —distance and voltage tunneling spectroscopy. *Electrochimica Acta* **40**, 1385–1394 (1995).

97. Hugelmann, M. *et al.* In Situ Distance Tunneling Spectroscopy at Au(111)/0.02 M $HClO_4$. *J. Electrochem. Soc.* ***151*** *E97(2004)*

98. Lunardon, M. *et al.* Atom-by-atom identification of catalytic active sites in operando conditions by quantitative noise detection. *Joule* **6**, 617–635 (2022).

99. Kosmala, T. *et al.* Operando visualization of the hydrogen evolution reaction with atomic-scale precision at different metal–graphene interfaces. *Nat Catal* **4**, 850–859 (2021).

100. Bandarenka, A. S. *et al.* Direct instrumental identification of catalytically active surface sites. *Nature* **549**, 74–77 (2017).

101. Hamelin, A. *et al.* Cyclic voltammetric characterization of oriented monocrystalline gold surfaces in aqueous alkaline solution. *Journal of Electroanalytical Chemistry and Interfacial Electrochemistry* **295**, 291–300 (1990).

102. Gallagher, M. E. *et al.* Structure sensitivity of CO oxidation on gold single crystal surfaces in alkaline solution: Surface X-ray scattering and rotating disk measurements. *Surface Science* **582**, 215–226 (2005).

103. Ohmori, T. *et al.* Hydrogen evolution reaction on gold electrode in alkaline solutions. *Electrochimica Acta* **37**, 2021–2028 (1992).

104. Goyal, A. *et al.* The Interrelated Effect of Cations and Electrolyte pH on the Hydrogen Evolution Reaction on Gold Electrodes in Alkaline Media. *Angew. Chem. Int. Ed.* **60**, 13452–13462 (2021).

105. McGuirk, G. M. Au(111) Surface Restructuring from Sulfur Adsorbates. *PennState University* (2011).

106. Weinrich, H. *et al.* Silicon and Iron as Resource-Efficient Anode Materials for Ambient-Temperature Metal-Air Batteries: A Review. *Materials* **12**, 2134 (2019).

107. Pourbaix, M. Atlas of Electrochemical Equilibria in Aqueous Solutions. *NACE* (1966).

108. Macdonald, D. D. Passivity - the key to our metals-based civilization. *Pure Appl. Chem.* (1999).

109. Urbaniak, J. *et al.* Preparation of Fe_2O_3-exfoliated graphite composite and its electrochemical properties investigated in alkaline solution. *J. Solid State Electrochem.* **14**, 1629–1635 (2010).

110. Dražić, D. M. *et al.* The anodic dissolution process on active iron in alkaline solutions. *Electrochimica Acta* **27**, 1409–1415 (1982).

111. Song, I. *et al.* Electrochemical behaviour of iron and iron oxide thin films in alkaline (1 m KOH) aqueous solution: a voltammetry study for cathodic instability of coating/metal interface. *J. Appl. Electrochem.* **26**, (1996).

112. Andersson, B. *et al.* Slow Potentiodynamic Studies of Porous Alkaline Iron Electrodes. *J. Electrochem. Soc.* **123**, 824–828 (1976).

113. Weinrich, H. *et al.* Understanding the nanoscale redox-behavior of iron-anodes for rechargeable iron-air batteries. *Nano Energy* **41**, 706–716 (2017).

114. Corneille, J. S. *et al.* Preparation and characterization of ultra-thin iron oxide films on a Mo(100) surface. *Surface Science* **338**, 211–224 (1995).

115. Somorjai, G. A. Modern Surface Science and Surface Technologies: An Introduction. *Chem. Rev.* **96**, 1223–1236 (1996).

116. Ooi, F. *et al.* A Facile Solvothermal Synthesis of Octahedral Fe_3O_4 Nanoparticles. *Small* **11**, 2649–2653 (2015).

117. Majumder, S. *et al.* Magnetization Enhancement of Fe $_3$ O $_4$ by Attaching onto Graphene Oxide: An Interfacial Effect. *J. Phys. Chem. C* **122**, 21356–21365 (2018).

118. Wilson, D. *et al.* XPS analysis of oleylamine/oleic acid capped Fe3O4 nanoparticles as a function of temperature. *Applied Surface Science* **303**, 6–13 (2014).

119. Deng, X. *et al.* In Situ Observation of Water Dissociation with Lattice Incorporation at FeO Particle Edges Using Scanning Tunneling Microscopy and X-ray Photoelectron Spectroscopy. *Langmuir* **27**, 2146–2149 (2011).

120. Baltrusaitis, J. *et al.* Adsorption of sulfur dioxide on hematite and goethite particle surfaces. *Phys. Chem. Chem. Phys.* **9**, 5542 (2007).

121. Zhang, H. *et al.* Adsorption mechanism of water molecules on hematite (104) surface and the hydration microstructure. *Applied Surface Science* **550**, 149328 (2021).

122. Lemire, C. *et al.* The surface structure of Fe_3O_4(111) films as studied by CO adsorption. *Surface Science* **572**, 103–114 (2004).

123. Duschek, K. *et al.* Electrochemical and in situ magnetic study of iron/iron oxide films oxidized and reduced in KOH solution for magneto-ionic switching. *Electrochemistry Communications* **72**, 153–156 (2016).

124. Albani, A. *et al.* A comparative electrochemical and ellipsometric study of the iron electrodes in different alkaline electrolytes. *Electrochimica Acta,* 31, **11**, 1403-1411 (1986)

125. Joiret, S. Iron passivation studied by in situ Raman spectroscopy on Fe/Au(111) epitaxial films.

126. Khaselev, O. *et al.* In-situ electrochemical scanning tunneling microscopy studies on the oxidation of iron in alkaline solution. *Electrochimica Acta* **42**, 2333–2337 (1997).

127. Schrebler Guzmán, R. S. *et al.* The potentiodynamic behaviour of iron in alkaline solutions. *Electrochimica Acta* **24**, 395–403 (1979).

128. De Faria, D. L. A. *et al.* Raman microspectroscopy of some iron oxides and oxyhydroxides. *J. Raman Spectrosc.* **28**, 873–878 (1997).

129. Lyons, M. E. G. *et al.* Redox switching and oxygen evolution electrocatalysis in polymeric iron oxyhydroxide films. *Phys. Chem. Chem. Phys.* **11**, 2203 (2009).

Acknowledgements

In primo luogo, desidero ringraziare il Relatore di questa tesi, Dr. Mattia Cattelan, il Prof. Stefano Agnoli e i Dottorandi del gruppo INCAT, in particolare Jijin e Marco, per l'immensa pazienza, disponibilità e competenza dimostrate in questi mesi nell'illuminarmi la via nel mondo della Scienza delle Superfici e dell'ultra-alto vuoto.

Un sentito ringraziamento va ai miei Genitori per avermi sempre spronato ad arrangiarmi, senza mai mancare quando avevo davvero bisogno, e per avermi permesso di continuare a studiare, supportandomi sia moralmente che economicamente.

Ringrazio le care Nonne, Laura e Silvana, per la scarsa parsimonia di complimenti quando le aggiornavo sui voti arrivati.

Non posso infine non ringraziare il Nek e la Erry sempre stati, nonostante la (relativa) lontananza, vicinissimi e pronti ad ascoltare lunghe note vocali.

Ringrazio di cuore la Mini Comunità e tutti gli Amici di Padova per il tempo di qualità trascorso insieme in Beato, in Piovego, a ballare, cantare, al parco, in appartamento o sul balcone condiviso del palazzo.

Per ultimi, ma non per importanza, gli Amici di Cerese, con cui ho condiviso innumerevoli splendidi momenti fino a questo traguardo, "per me, nulla ripaga di più di una notte passata con voi".

Grazie Padova,

sei meravigliosa.